THE LITHIUM AND HYDROGEN INTERCALATION INTO ELECTROCHROMIC MATERIALS: TUNGSTEN TRIOXIDES AND CESIUM TUNGSTEN OXIDES

by

Qiming Zhong

B.Sc., Shanghai University of Science and Technology, 1977

M.S., Fudan University, Shanghai, 1982

THESIS SUBMITTED IN PARTIAL FULFILLMENT OF

THE REQUIREMENTS FOR THE DEGREE OF

DOCTOR OF PHILOSOPHY

in the Department

of

Physics

Simon Fraser University

December 1991

ISBN 0-315-83734-9

Approval

Name: Qiming Zhong

Degree: Doctor of Philosophy

Title of thesis: Lithium and Hydrogen Intercalation into Electrochromic Materials: Tungsten Trioxides and Cesium Tungsten Oxides

Examing committee:

Chairman: Professor E.D. Crozier

Professor K. Colbow
Senior Supervisor

Professor S.R. Morrison
Dept. of Physics, SFU

Professor J.F. Cochran
Dept. of Physics, SFU

Associate Professor J.R. Dahn
Dept. of Physics, SFU

Dr. W.R. McKinnon
External Examiner
Institute for Microstructural Science
National Research Council of Canada

Date Approved: February 11, 1992

PARTIAL COPYRIGHT LICENSE

I hereby grant to Simon Fraser University the right to lend my thesis, project or extended essay (the title of which is shown below) to users of the Simon Fraser University Library, and to make partial or single copies only for such users or in response to a request from the library of any other university, or other educational institution, on its own behalf or for one of its users. I further agree that permission for multiple copying of this work for scholarly purposes may be granted by me or the Dean of Graduate Studies. It is understood that copying or publication of this work for financial gain shall not be allowed without my written permission.

Title of Thesis/Project/Extended Essay

The lithium and hydrogen intercalation into electrochromic materials : tungsten trioxides and cesium tungsten oxides

Author: _____
(signature)

Zhong, Qiming
(name)

April 2, 1992
(date)

Abstract

Using electrochemical techniques and x-ray diffraction methods, lithium and hydrogen intercalations into tungsten trioxide and cesium tungsten oxides were studied. Tungsten trioxide (WO_3) has been used as electrochromic (EC) material for about 20 years, but two new cesium tungsten oxides were first studied as the EC material in this work.

Three kinds of WO_3 materials were studied: 1. WO_3 films prepared by thermal vacuum evaporation and recrystallization treatment; 2. Commercially purchased WO_3 powder; 3. WO_3 powders prepared by heating tungstate H_2WO_4 at various temperatures. Basic electrochromic properties of WO_3 films were investigated, including optical absorption changes after hydrogen and lithium intercalations; relations between the hydrogen and lithium content and the optical densities in WO_3 films; and the hydrogen and lithium diffusion coefficients inside the WO_3 film. Specific attention was given to the crystal structures of formed hydrogen tungsten bronze H_xWO_3 and lithium tungsten bronze Li_xWO_3 films. A computer program (Rietveld profile refinement program) was used to analyze the x-ray diffraction patterns obtained from lithium or hydrogen intercalated WO_3 films. The structures of electrochemically formed H_xWO_3 and Li_xWO_3 films were determined for the first time. The initial monoclinic WO_3 host changes to a tetragonal structure at $x = 0.4$ in the H_xWO_3 film and $x = 0.08$ in the Li_xWO_3 film. The structures of tetragonal H_xWO_3 and Li_xWO_3 are quite similar and belong to the same space group P4/nmm. The structure of

Li_xWO_3 changes further to a cubic phase at about x = 0.28 in Li_xWO_3 film. It was found that the lithium can not intercalate into commercially purchased WO_3 powder as readily as in WO_3 films. A technique was developed to prepare WO_3 powders in which the same phase transition takes place as in WO_3 films. Using *in situ* x-ray experiments, structure changes caused by lithium intercalation in the prepared WO_3 powder host were studied. As lithium slowly intercalated into the WO_3 powder, a sequence of x-ray diffraction patterns were collected. With the analyzed data, a phase diagram for electrochemically formed Li_xWO_3 was created.

Hydrogen and lithium intercalations in two cesium tungsten oxide films were also investigated. Hexagonal cesium tungsten bronze $Cs_{0.30}WO_3$ powder was prepared by thermal solid state reaction and pyrochlore cesium tungsten oxide $(Cs_2O)_{0.43}W_2O_6$ powder was prepared by wet chemical reaction. The films were prepared by evaporating the corresponding powder in a vacuum system. The hydrogen and lithium intercalations in prepared cesium tungsten oxide films were studied. The hydrogen and lithium diffusion coefficients were found to be dependent on the host crystal structures.

Acknowledgements

I would like to express my sincere appreciation to Professor Konrad Colbow for his valuable suggestions, encouragements and guidance throughout this research work, and also for his patient reading of this manuscript.

I would like to expess my most sincere thanks to Dr. Jeff Dahn for his kind help and important directions and suggestions in the most part of experiments for this thesis. I wish to thank Professor S. Roy Morrison and Professor John F. Cochran for their time and advice in the Supervisory Committee. I also wish to thank Professor Albert E. Curzon and Dr. Bretislav Heinrich for their help with the experiments. I wish to extend my thanks to the staff of the Physics Department of Simon Fraser University for their various assistance. I am especially thankful to Moli Energy Ltd. for the TGA and surface area analysis.

This work was partially supported by the Frank Allison Linville Institute for Sensory Science.

Table of contents

List of figures

List of tables

Chapter 1

Introduction

1.1 Introduction

Electrochromism is a phenomenon in which materials change their optical absorption or transmission in response to an applied electrical field. The electrochromic (EC) phenomenon has been known since the early time of this century, but attracted a great deal of attention of scientists in only the recent two decades. This is due to the fact that the EC materials recently developed (typically WO_3 and its compounds) showed promise for their potential application in non-emissive alpha-numeric display devices and adjustable energy efficient windows. Low voltage operation, wide viewing angle, and the passive nature (i.e., the induced color remains even after switching off the applied voltage, also called memory effect) of these EC materials made them interesting candidates for use in flat panel display technology and large area optical transmittance control such as energy efficient windows. The significance in studying electrochromism is not only because of its potential application but also because of its interesting physical mechanism. The investigation on electrochromism is basically a combination of new material synthesis, electrochemical analysis, crystal structure determination and electro-optical characterization.

As an introduction in this chapter, a historical development of EC materials is reviewed. Considerable attention is given to the transition-metal oxides, especially to the EC properties and EC mechanism of tungsten oxide.

1.2 Electrochromic materials, a general review

A number of materials, both organic and inorganic, exhibit EC properties, although the physical mechanisms by which these materials change color can be different. We can categorize these materials into several different branches as shown in figure 1.1:

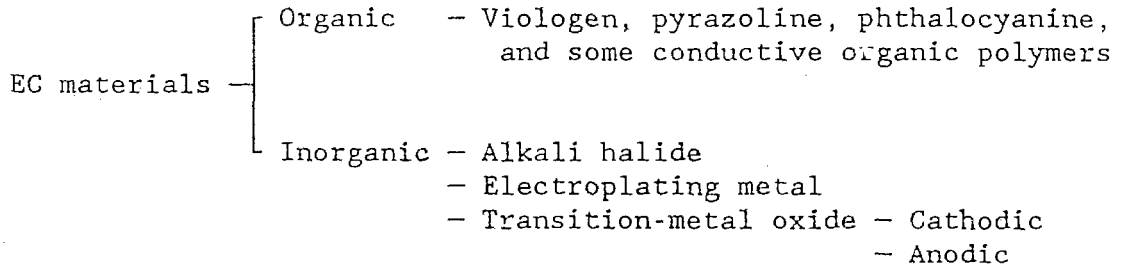

Fig.1.1 General categories of EC materials.

1.2.1 Organic EC materials

The coloration in organic materials is usually observed in an oxidation-reduction reaction. Michaelis and Hill (1933) reported first the coloration process in 4,4'-dipyridinium compounds and named them viologens. The viologens could change color under certain electrical potentials. In general viologens can be represented as

(1.1)

where R can be a methyl, alkyl or cyclo-alkyl group and X is a halogen atom. It is more common to describe the viologens with a formula: $A^{2+}X_2^-$ where A^{2+} represents 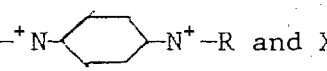 and X^- the halogen ion. Elofson and Edsberg (1957) studied methyl-viologen extensively and reported that A^{2+} underwent a two step reduction process as follows:

$$(1)\ A^{2+} + e^- = A^+ \quad ; \qquad (2)\ A^+ + e^- = A \tag{1.2}$$

The product from first reduction was dark blue. The use of viologens for EC display devices was suggested by Schoot et al in 1973. Diheptylviologen-dibromide ($R = C_7H_{15}$, $X = Br$) was used for this device application. The device was composed of Au(anode)/ 1M diheptylviologen-dibromide aqueous solution/SnO_2(cathode) with saturated calomel electrode (SEC) as a reference electrode. When an applied potential on the cathode was more negtive than -0.66V vs. SCE, the A^{2+} ion may absorb an electron and be reduced to A^+. An insoluble purple solid A^+Br^- was then precipitated on the cathode electrode as a film. The colored film could be kept unchanged for as long as several days to several months until it was completely removed by a reverse current (oxidation process) thus this process was reversible. A^+ might further absorb a second electron to form A and to produce a yellow color at a potential about -1.06V vs SCE. The second reduction process was reported as electrochemically irreversible. The EC properties of some other viologens for display were reported later (Van Dom, H.T. and Ponjee, J.J. 1974; Tsutomu, K. et al 1975). Various

substitutes for R and X in viologen compounds were studied. Most viologen EC systems reported were aqueous systems which always faced the problem of water electrolysis. The other organic EC systems studied were rare-earth diphthalocyanine compounds, such as lutetium-diphthalocyanine, (Moskalev and Kirin 1972; Corker et al 1979; Nicholson and Pizzarello 1979, 1980), pyridine (Platt 1961), pyrazoline (Pole et al 1976), and polymer systems (Kaufman 1980). Most organic EC systems suffered from two major problems. First of all, the use of aqueous solution and hence water electrolysis, and secondly soluble colored products , which causes color diffusion and image fuzziness.

1.2.2 Alkali-halide EC materials

The EC phenomena in inorganic materials can be traced back to as early as 1932 (Pohl 1932) when an alkali-halide single crystal of KCl or NaCl was heated to about 700 °C, the anion vacancy concentration and hence the ionic conductivity increased. When a high electric field (~500 V/cm) was applied to this crystal by a point cathode, the crystal turned dark blue. The coloration originated from injected electrons, trapped at anion vacancy sites, causing the formation of color centers like F, F^+ etc. The color center formation is a well-known phenomenon and has been a subject in several textbooks, e.g (Schulman 1962). The concentration of color centers is governed by thermodynamic equilibrium conditions and is very low at room temperature. Thus it is impractical to be used for display devices.

1.2.3 Electro-plating systems

An electro-redox reaction wherein a metal layer is deposited on the electrode, forming a solid metallic layer, is generally referred to as electroplating. The concept of reversible electroplating was first extended by Smith (1929) to fabricate light modulating devices. Based on this concept, Zaromb (1962) analyzed the design principle of a reversible electro-plating light valve and suggested using AgI solution in electro-plating system which could give silver plating on the cathode and I_2 on the anode. A silver bromide solution was employed in the device later by Zaromb (1966) to provide an easy-erasing plating system. Some other solution systems were also studied such as Cu^+ in 10% $HClO_4$ (Flanagan et al 1964) and silver nitrate solution (de Koster 1971). The main problem in electro-plating system seems to be non-uniformity in the plating process and the slow response time to change in optical properties.

1.2.4 Transition metal oxides

Several transition metal oxides show EC properties. The most popular systems are from the VI-B oxides. In this group, WO_3 and MoO_3 are the most thoroughly studied cathodic EC materials which can be electrochemically colored and bleached when used as the cathode in electrochemical cells. Cathodic EC materials include also V_2O_3, TiO_2 and Nb_2O_5. Another distinguishable group is anodic EC material including group VIII oxides like $IrO_x \cdot H_2O$, $Rh_2O_3 \cdot nH_2O$, $NiO \cdot nH_2O$ and $Co_2O_3 \cdot nH_2O$ which can be anodically colored in the electrochemical process when used as an anode. In this

section, a basic EC process involved in both cathodic and anodic materials will be introduced.

Cathodic oxides

It has been known since 1914 (Torossian 1914) that the tungsten oxides can be chemically reduced to form a blue compound. Talmey (1942, 1943) seems to be the first to propose that the tungsten and molybdenum oxides could be used as electrolytic recording paper. Later Brimm et al. (1951) also reported that electrolytic reduction of tungsten oxide produced a blue coloration. However, it was not until 1969 (Deb 1969) that tungsten oxide film was used in an actual electrochromic display device. A thin amorphous WO_3 film was used as the EC material and a color change was observed when the electrical potential across the film was at about 10^4 V/cm. Since then the studies of electrochromism has been pursued by many investigators. Later Deb (1973) reported that amorphous tungsten oxide film could also be colored when exposed to UV radiation. An increase in conductivity was observed when the WO_3 films turned from transparent to blue colored. Deb explained these coloration processes by F-type color centers. However, Green and Richman (1974) soon proposed that coloration of WO_3 film could be more efficiently achieved in an electrochemical cell. Faughnan, Crandall and Heyman (1975) further demonstrated that the coloration was due to electrochemical formation of a tungsten bronze based on a typical electrochemical cell as shown in figure 1.2

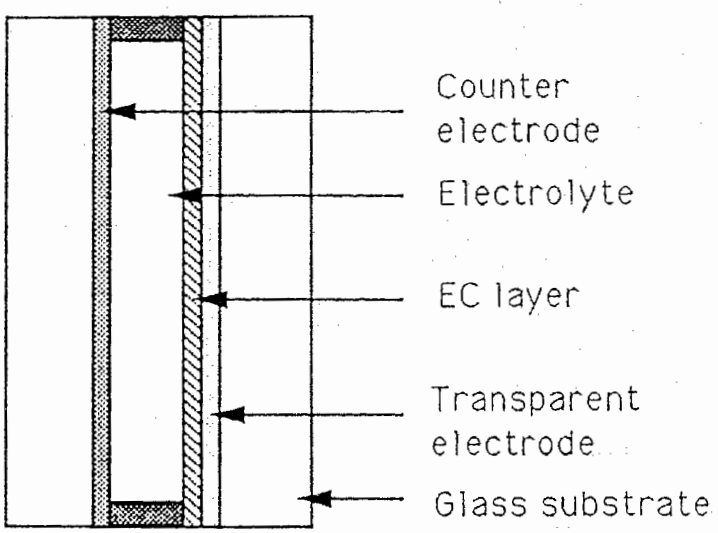

Fig. 1.2 Schematic illustration of an electrochemical cell

The cell can work in either a reflection mode or a transmission mode. A doped In_2O_3 or SnO_2 film was used as transparent layer which is electrically conductive. Amorphous or polycrystalline WO_3 films were used as the EC layer which was initially transparent. The electrolyte might be aqueous (e.g. 10% H_2SO_4 in H_2O), non-aqueous (e.g. $LiClO_4$ in propylene carbonate), or solid (e.g. Nafion* and poly-AMPS**). The cations contained in electrolytes were usually H^+, Li^+ and Na^+. The counter electrode was a material which should be reversible to the same ion as that involved in the EC reaction in the cell. The counter electrode might be the same

---

* Nafion is a Dupont trademark for polyperfluosulfonic acid.

** Polymerized 2-acrylamido-2-methylpropanesulfonic acid.

material as the EC layer (Morita and Washida 1980). When an electric potential was applied across the cell to reduce the electrical potential on the WO_3 films, the WO_3 film turned blue. The blue color in WO_3 film remained unchanged after the power supply was disconnected and could be erased by reversing the polarity of the applied potential. Faughnan, Crandall and Heyman (1975) suggested a tungsten bronze formation process by the following formula:

$$\underset{\text{(transparent)}}{WO_3} + xM^+ + xe^- \longrightarrow \underset{\text{(blue colored)}}{M_xWO_3} \qquad (1.3)$$

where M^+ could be H^+, Li^+, Na^+ or Ag^+. In contrast to the tungsten bronze model, Chang et al (1975) investigated coloration of WO_3 films in the above electrochemical cell as shown in figure 1.2 and interpreted the coloration mechanism as electrochemical extraction of oxygen from the WO_3 film with substoichiometric WO_{3-y} as the colored product, but they could not explain the coloration process when the WO_3 film was colored in a aprotic electrolyte system (non-aqueous system), such as a Li based electrolyte system. Hurdich (1975) studied the water effect in WO_3 films during the EC process and suggested the formation of a hydrated hydrogen tungsten bronze ($WO_{3-x}(OH)_x \cdot aq$). However, this explanation appears to be in conflict with earlier work (Glaser et al, 1951, 1964) which showed that hydrated hydrogen tungsten bronze was the reduction product of hydrated tungsten oxide ($WO_3 \cdot nH_2O$) and had the same structure as H_xWO_3. Meanwhile the tungsten bronze model was also suggested by many other investigators (e.g. Weibel, 1975; Hobbs and Tseung 1972, 1973, 1975). Studies using aprotic liquid electrolytes with Li^+ or Na^+ as the mobile cation (Weibel,

1975; Hersh, 1975; Green, 1976) showed more evidences of the tungsten bronze formation. However, it should be noted that most of the authors mentioned above paid attention to the optical properties of the WO_3 films. They usually used the tungsten bronze model to explain the I-V behaviors of their EC cells and the optical density in the colored WO_3 films. No direct experimental data were reported for the crystal structures of the tungsten bronzes. So several years later the tungsten bronze model was still disputed by some investigators. Using resonant nuclear reaction with boron, Deneville, Gerad and co-workers (Deneuville, 1980; Gerad, 1980) measured the hydrogen content in electrochemically colored and bleached amorphous WO_3 films and found a high H content in both cases within experimental error (quoted as 3%). Thus they proposed another model in which coloration was brought about not by the insertion of H, but by the redistribution of already incorporated H atoms in the WO_3 films from optically inactive sites to optically active sites. They suggested that the optical active sites have a different energy, so that the hydrogen rearrangement gave rise to a change in the chemical potential of H. Most of their data was obtained from WO_3 films colored by non-electrochemical techniques, such as ultra-violet illumination, annealing in vacuum and exposing to H_2 atmosphere. There were some obvious shortcomings in this model, not the least of which was an explanation for the quantity of charges passed through the cell needed on coloration and bleaching. This charge was several tens of mC/cm^2 for deep coloration, whereas in the redistribution model the only charge needed would be that to charge the double-layer capacitance on the electrolyte-WO_3 interface, typically, <20 $\mu C/cm^2$. Although the redistribution model was not accepted by most investigators, the high content of H atoms in bleached WO_3 films was not

explained and remained as an unsolved problem. A more detailed discussion about the coloration mechanism in WO_3 will be given in Chapter 2. Apart from the studies in EC mechanism of WO_3 films, there were many investigations in the fields related to the application of WO_3 EC cells, such as the methods of film preparation (Miyake et al 1983; Kaneko et al 1986; Zeller and Paola et al 1987; and Hiroshi and Yoshihiro 1990), utilization of different electrolytes (Miyamura et al 1981; Randin 1982; Lagzddons et al 1984 and Calvert et al 1986) and the design of an efficient EC cell structure (Hiroshi et al 1984; Kazusuke 1986; and Schlotter 1987).

Another well developed cathodic electrochromic material is MoO_3 (Deb 1966; Rabalais 1974 and Arnoldussen 1976) which shows a very similar electrochromic behavior to that of WO_3. The characteristic color of activated MoO_3 is blue or purplish blue. A detailed study of MoO_3 films in liquid electrolytes containing H^+ ions was reported by Deb and Witzke (1977). Due to its high solubility in aqueous solution, MoO_3 received much less attention than WO_3 films although there were still some investigations reported, such as the EC properties of MoO_3 films prepared by electron beam deposition (Nobuyoshi et al, 1984) and by Chemical Vapor Deposition (CVD) (Tracy and Benson, 1986).

The group V-B oxides, such as V_2O_5 and Nb_2O_5 also exhibit electrochromism. Gavrilyuk and Chudnovskii (1977) and Colton et al (1978) reported the electrochromism in evaporated V_2O_5 films and Witzke and Deb (1977) reported the electrochromism in sputtered V_2O_5 films. The bleached state of the V_2O_5 films was yellow and electrochemically induced color was

greenish-blue at low ion insertion levels. At a high ion insertion level, the V_2O_5 films turned dark-blue or gray. Due to the high solubility of V_2O_5 in acid, the electrolytes used with V_2O_5 films were usually metal-salt aqueous solutions like LiCl, KCl and RbCl in distilled water (Dickens et al, 1989) or $LiClO_4$ in non-aqueous solutions (Stuart et al, 1989). Nb_2O_5 was stable in both aqueous acidic electrolytes and in non-aqueous electrolytes (Dyer and Leach, 1978, Reichman and Bard, 1980). The Nb_2O_5 could turn blue when the content of the inserted H and Li atom in the films was high. Dyer (1978) reported electrochromism in amorphous TiO_2 films which showed a blue color when reacted with H^+. Later Ottaviani (1986) analyzed the EC process of pyrolytically prepared TiO_2 films in the $LiClO_4$/PC electrolyte and attributed the final colored product to Li_xTiO_2. The main drawback in the EC property of V_2O_5, Nb_2O_5 and TiO_2 is their low optical efficiency which means that a large amount of cations are needed to insert into these oxides for a required optical density.

Anodic oxides

Anodic oxides can be colored when used as an anode in the EC cell. In the coloration the anion may be incorporated into the coloring/bleaching processes although the EC mechanism involved is far less clear. EC properties were found in group VIII oxides including iridium oxide (Beni and Shay, 1978 and Rice, 1979), rhodium oxide (Gottesfeld, 1980) and nickel oxide (Micheal, 1987). It was found that only hydrated VIII oxides showed electrochromism (Lampert, 1984). Among anodic oxides, iridium was one of the most studied materials. In a symmetric cell with iridium oxide films as both cathode and anode with 0.5M ~ 2.0M H_2SO_4 aqueous

electrolyte, a color change could be observed on the anode Iridium film when the voltage across the cell was approximately 1.5 – 2.0 V (Dautremont-Smith, 1979). The characteristic color on the activated iridium anode was dark-blue. The coloration was proposed based on one of the following two mechanisms (Dautremont-Smith, 1982):

$$Ir_2O_3 \cdot nH_2O - 2H^+ - 2e^- \rightarrow Ir_2O_3(OH) \cdot (n-2)H_2O \qquad (1.4)$$

or $$Ir_2O_3 \cdot nH_2O + 2OH^- - 2e^- \rightarrow Ir_2O_3(OH)_2 \cdot nH_2O \qquad (1.5)$$

During the coloration process, electrons were extracted from the film by the external circuit and the current was passed ionically across the film/electrolyte interface. Two opposing models were suggested by the different ion processes at the film/electrolyte interface. However, it should be noted that, starting from the same hydrated iridium oxide, the chemical compositions of the two colored states proposed by these models are identical except for the degree of hydration. Discussions of electrochromism in other anodic VIII oxides can be found in review papers by Lampert (1984) and Dautremont-Smith (1982).

As shown above, several materials exhibit EC behavior, However, very few materials possess EC properties that are required to make EC display devices. The coloration mechanisms in various EC materials might be different, and each material has its own advantages and disadvantages. As far as the transition-metal oxide system is concerned, materials like tungsten oxides and iridium oxides seem to be good candidates for applications. The iridium oxide is relatively new in the literature. On

the other hand, the EC property of WO_3 has been extensively studied over the last two decades and will be further studied in this thesis. The detail discussion for WO_3 is carried out in the next chapter.

Chapter 2

Electrochromism in WO_3

The investigations of electrochromic phenomenon in tungsten oxides have been extended to a wide research area during the last twenty years. The attention arose because of its promising potential for application in display devices and its flexible oxidation states and various crystal structures. In this chapter, the basic property of bulk WO_3 will be first described. After that the property of WO_3 films prepared by various methods will be discussed. Most attention will be given to the understanding of the EC processes in WO_3 films, including the tungsten bronze formation process, coloration mechanism and the problems encountered in studies. At the end of this chapter, the main objectives of this thesis will be presented.

2.1 The basic knowledge of bulk WO_3

The understanding of crystal structures of bulk tungsten oxides is an essential in studying the EC properties of tungsten oxide films in the EC cell. Tungsten trioxide (WO_3) is the highest oxidation state compound in the tungsten-oxygen system. At room temperature, tungsten trioxide shows a monoclinic crystal structure (Loopstra 1969; Tanisaki 1960). WO_3 shows also at least five phase transitions in the temperature range from 900°C

to −180°C (Salje, 1977 and Tanisaki, 1960) changing from tetragonal(900°-740°C) - orthorhombic(740°-350°C) - monoclinic(350°-17°C) -triclinic(17°--40°C) - monoclinic(<-40°C). The crystal structure of WO_3 can be described as consisting of corner-shared WO_6 octahedra extended in three dimensions. this structure is basically a distorted ReO_3 structure. Fig. 2.1 shows the WO_3 structure. There are other stable tungsten oxide compounds existing in the tungsten-oxygen system in which the oxidation state of tungsten atoms can be varied from 2 to 6 (see table 2.1). Loopstra (1969) determined the lattice parameters of WO_3 powder at room temperature. The structure was monoclinic with a = 7.306(1)Å, b = 7.540(1)Å, c = 7.692(1)Å, and β = 90.881(5)°. The atom positions of W and O in this monoclinic unit cell are depicted in Fig. 2.2. The numbers on the circles indicate the atom positions in c - direction (perpendicular to the paper). The symmetry of WO_3 at room temperature belongs to space group $P2_1/n$. At room temperature WO_3 is an n-type semiconductor with a specific resistivity of 0.3 - 10 Ω cm (Crowder and Sienko 1963). The optical band gap of a single crystal WO_3 was found to be 2.7 ev (Sawada 1956).

Table 2.1 Crystallographic data for various tungsten oxides

Formula	Range	Crystal structure Cell dimensions Å	Color	Ref.
WO	$WO-WO_{1.9}$	cubic Pm3n a = 5.036	Gray	Rieck (1967)
WO_2	$WO_{1.99}$ – $WO_{2.02}$	monoclinic $P2_1$ a = 5.650; b = 4.892 c = 5.550; β = 140.42°	brown	Rieck (1967)
$W_{18}O_{49}$	$WO_{2.66}$ – $WO_{2.77}$	monoclinic P2/m a = 18.32; b = 3.97 c = 14.04; β = 115.2°	reddish	Rieck (1967)
$W_{20}O_{58}$	$WO_{2.88}$ – $WO_{2.92}$	monoclinic P2/m a = 12.05; b = 3.767 c = 23.59; β = 85.28°	blue	Rieck (1967)
WO_3	$WO_{2.95}$ – WO_3	720°-900° tetrag. P4/nmm a = 5.250; b = 3.915		Kehl (1952)
		320°-720° orthorhomb. a = 7.35; b = 7.56 c = 3.865		Salje (1977)
		17°-320° monoclinic $P2_1/n$ a = 7.306; b = 7.540 c = 7.692; β = 90.881°	yellow	Loops-tra (1969)
		-40°-17° triclinic a = 7.30; b = 7.52 c = 7.69; α = 88.50° β = 90.55°; Γ = 90.56°		Tanisa-ki (1959)
		< -40° monoclinic a = 5.27; b = 5.16 c = 7.67; β = 91.43°		same as above

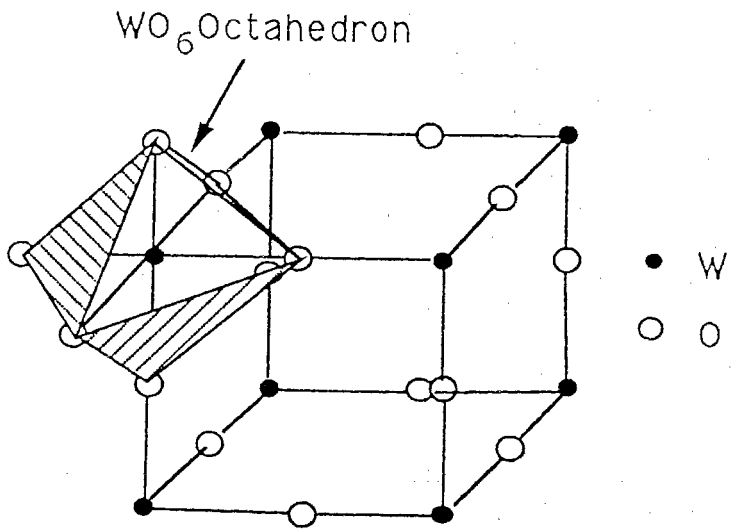

Fig. 2.1 WO_3 structure

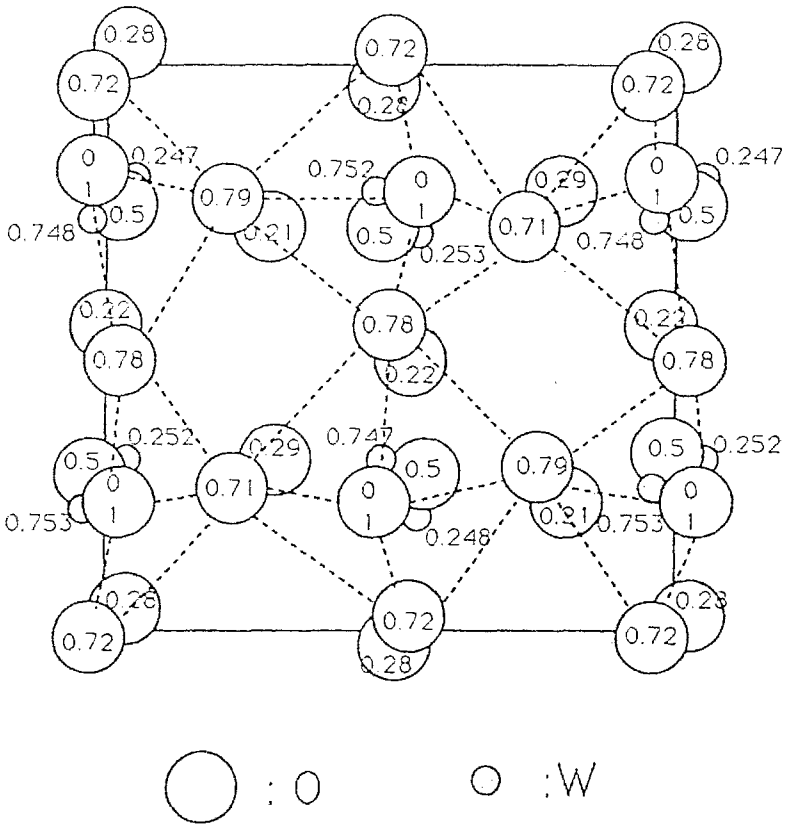

Fig. 2.2 Atomic positions in the monoclinic WO_3 unit cell

It was very difficulty to obtain pure WO_3 single crystals, due to its non-stoichiometric characteristic in the range of WO_3 to $WO_{2.95}$. Some edge-sharing WO_6 octahedra were suggested to exist in the main corner-sharing octahedra frame network (Salje et al 1979; Tilly 1982). The WO_3 melts at 1470°C (Kubaschewski et al 1958) and sublimes at about 1100 °C (Berkowitz et al 1957). According to Sienko and co-workers (1970) , WO_3 possesses a normally empty conduction band to which the electrons can be exited from shallow (0.03-0.05 eV) donor levels, such as oxygen vacancies or W-W interaction pairs that result from the collapse of the shared octahedron

corners. The carrier concentration, $n = 10^{17} - 10^{18}$ at room temperature (Crowder and Sienko 1963), increased as the oxygen vacancies increase, which leads to a blue color in the WO_3 powder.

Apart from the tungsten oxides listed in table 2.1, there are several hydrated tungsten oxides. Due to the similar chemical compositions with tungstic acids, hydrated tungsten oxide was not systematically identified and studied until the work by Freedman (Freedman 1959). Freedman found that if sodium tungstate in aqueous solution was precipitated by hydrochloric acid with various concentration and temperature, at least five different phases occurred, three of these were:

(i) *tungsten oxide hydrate* $WO_3 \cdot H_2O$, an orange-yellow product obtained with 2-9 N HCl at 100°C.

(ii) *tungsten oxide dihydrate* $WO_3 \cdot 2H_2O$, a yellow gel produced with 0.5-9.0 N HCl at 25°C.

(iii) *white* $WO_3 \cdot 0.5H_2O$ *or* $H_2W_2O_7$, which often contained some alkali and might be written: $Na_2O \cdot (WO_3 \cdot 0.5H_2O)_{8-10}$, prepared with diluted sodium tungstate solution with 2-6 N HCl at 25°C.

Later Freedman and Leber (1964) further confirmed these phases by chemical analysis and X-ray powder diffraction.

Two new phases of tungsten trioxide at room temperature were recently developed. They were synthesized from tungstate (e.g. sodium tungstate Na_2WO_4) and hydrated tungsten oxides:

(i) *hexagonal (h) tungsten oxide hydrate*, $h\text{-}WO_3 \cdot 1/3H_2O$, (Gerand et al 1981). After a yellowish gel resulted from mixing the solutions of sodium tungstate and 10 N HCl in an autoclave at 120°C for 20

hours, a hexagonal $WO_3 \cdot 1/3H_2O$ was obtained. The structure parameters for this product were a = 7.359(3)Å, c = 7.704(5)Å, Z = 12. The structure of h-$WO_3 \cdot 1/3H_2O$ could be described as an infinite plane of WO_6 octahedra sharing their corners and forming six-member rings in the (001) plane. The probable space group was Fmm2.

(ii) *pyrochlore (p) tungsten oxide hydrate*, p-$WO_3 \cdot 0.5H_2O$, (Günter et al 1989; Coucou and Figlarz 1988). Günter obtained p-$WO_3 \cdot 0.5H_2O$ by mixing 20 ml of 1 M Na_2WO_4 solution with 28 ml of 1.2 M HCl at room temperature in a sealed tube heated at 155°C for 3 days. Coucou prepared p-$WO_3 \cdot 0.5H_2O$ in two steps: first pyrochlore-type ammonium tungstate $[(NH_4)_2O]_xW_2O_6$, x~0.5, was prepared by heat-treatment of ammonium tungstate $(NH_4)_{10}W_{12}O_{41}$ in an acidic solution, then the pyrochlore-type ammonium tungstate was treated by 6N HNO_3 to produce p-$WO_3 \cdot 0.5H_2O$. The crystal structure of p-$WO_3 \cdot 0.5H_2O$ was cubic belonging to the Fd3m space group. The lattice parameters determined by two authors were very close: a = 10.270(3)Å (Coucou 1988) and a = 10.305(3)Å (Günter 1989). The structure of p-$WO_3 \cdot 0.5H_2O$ was actually a stack of hexagonal h-WO_3 layers in the (111) direction (Figlarz 1989).

These two tungsten oxide hydrates can both be dehydrated at a temperature range from 200°C to 250°C, resulting in a pure h-WO_3 or p-WO_3. The h-WO_3 and p-WO_3 are not stable when they are heated at a temperature greater than 350°C above which these phases change to monoclinic.

2.2 Preparation and general physical properties of WO_3 films

In the past various methods have been used for preparation of tungsten oxide films. Vacuum evaporation was one of the widely used techniques in WO_3 film preparation (Deb 1969, 1973; Hersh and Kramer 1975; Faughnan et al 1975; Schirmer et al 1977; Benjamin and Allen 1979). WO_3 powders were usually evaporated from a Mo (Miyake et al 1983) or W (Morita and Washida 1984) boat at a vacuum of $\sim 10^{-5}$ torr onto a substrate such as soda lime glass, indium-tin coated glass, antimony or fluorine-doped tin oxide coated glass or β-Al_2O_3. The as-prepared WO_3 film was amorphous and transparent with a light blue color if the substrate was kept at room temperature. Miyake et al (1983) studied the crystal structure of WO_3 films evaporated at different substrate temperature, and reported that WO_3 films became polycrystalline when the substrate temperature was above 400 °C. Miyake (1983) assigned bulk WO_3 structure (monoclinic) to the x-ray diffraction patterns of crystallized WO_3 films. In most cases as-prepared films were substoichiometric with O:W ratio from 2.7 to 2.9 (Deneuville et al 1978, 1980; Gerad et al 1980). Many authors annealed amorphous WO_3 films in N_2 or vacuum to recrystallize the films (at $T > 350$ °C) or in air and O_2 to get stoichiometric films. Reactive sputtering was another method commonly used in the WO_3 film preparation (Green et al 1976; Barna 1979; Crandall and Faughnan 1976; Goldner et al 1983; Kaneko et al 1988). The sputtering atmosphere was usually Ar-O_2 and the argon-oxygen pressure during sputtering was generally varied from 5×10^{-2} to 5×10^{-3} torr with oxygen concentration from 5% to 50%. The prepared films could be either amorphous or polycrystalline depending on the substrate temperature during the sputtering. Hurdritch (1975) prepared WO_3 films by

spraying metatungstic acid ($H_6W_{12}O_{39}$ $15.5H_2O$) onto Mo, Al, or Au coated quartz substrate at the temperature range from 130 to 350 °C. The composition of the sprayed films was determined to be WO_3 $x(H_2O)$ where x decreased with increase in substrate temperature from 0.23±0.03 at 140 °C to 0.02±0.03 at 320 °C. Zeller and Beyeler (1977) also used a solution spray technique to prepare WO_3 films and their results were similar to that of Hurditch. There were some other techniques for WO_3 film preparation like Anodic oxidation of W (Benjamin and Allen 1979, Paola et al 1978) and chemical vapor deposition (CVD) (Davazoglou and Donnadieu 1987).

It seems difficult to compare various methods of WO_3 film preparation. The reported EC properties of WO_3 films varied from one to the other although the same technique was being used. It was understood that the EC properties of WO_3 films were very sensitive to the preparation conditions like substrate temperature, deposition rate, deposition atmosphere, chemical purity in source materials, and post-deposition treatment. From high resolution electron microscope studies, Shiojiri et al (1978) reported that in the case of evaporated films (100-150 Å thick), the crystallite size varied between 10-20 Å and crystallites had the monoclinic structure. Green (1978) mentioned that the crystallite size varied from 20-500 Å in sputtered WO_3 films depending upon the preparation conditions. He reported that in sputtered films, crystallites greater than 250 Å exhibited a tetragonal structure. However, he has not mentioned any crystal structure for the films with crystallites smaller than 250 Å.

2.3 Electrochromism in WO_3 films

2.3.1 The electrochemical process

As mentioned in section 1.2.4, in an attempt to understand the physical mechanism of coloration in WO_3 films, several models have been developed. Following the literature, we can divide the coloration process of WO_3 films into two categories: one is the electrochemical coloration process as it occurs in the EC cell shown in figure 1.2 and the others are non-electrochemical coloring processes such as were brought about by UV illumination and vacuum annealing. Our main concern is with the electrochromism based on an electron-ion intercalation process which leads to the formation of tungsten bronze. Figure 2.3 depicts the electrochemical coloring process in a Li(metal)/Li^+ in electrolyte/WO_3(film) cell in which the Li^+ ion is the active species. The coloration process in the cell involves ionization of lithium atoms at the interface of the counter electrode (lithium metal)/electrolyte, migration of lithium ions across the electrolyte, the transfer of lithium ions through the interface of the electrolyte/WO_3 film, neutralization of the lithium ions at the surface of the WO_3 film with injected electrons and the chemical diffusion of these accumulated lithium atoms within the WO_3 film. The final coloration in the WO_3 film is due to the formation of the lithium tungsten bronze. In the bleaching process, the lithium moves in the reverse direction. This coloring/bleaching process in the WO_3 film has been expressed by equation (1.3):

$$WO_3 + xM^+ + xe^- \longleftrightarrow M_xWO_3$$

where M^+ can be H^+, Li^+, or Na^+. Although tungsten bronzes were believed to be formed during the coloration process, there was a lack of direct experimental data to show the existence of tungsten bronzes, at least no analyzed data on the crystal structures of the tungsten bronzes were reported.

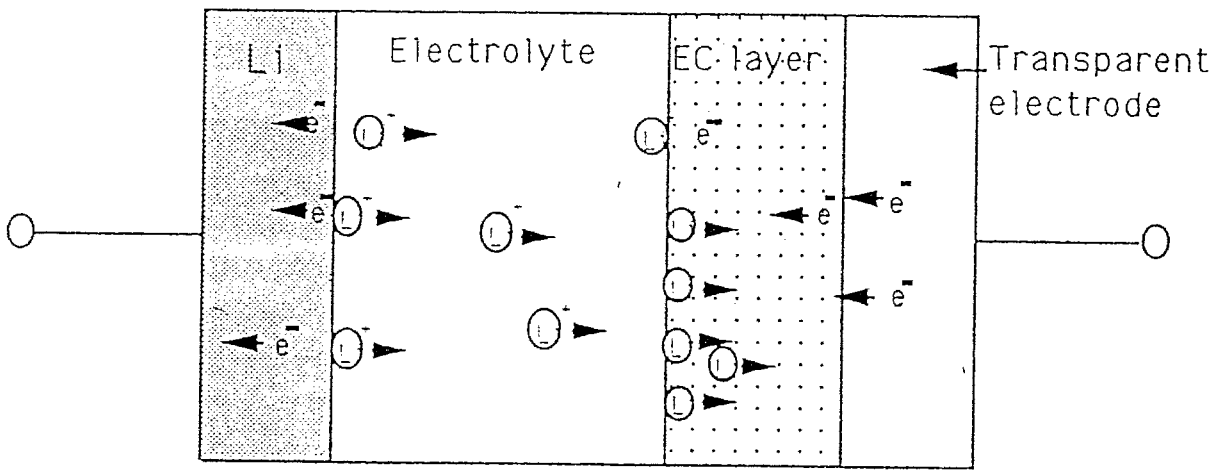

Fig. 2.3 Illustration of electron-ion injection process

2.3.2 The coloration mechanism

W^6 to W^5 intervalence transfer model

To explain the blue color induced in M_xWO_3 films, a basic injection explanation seems not enough. Faughnan et al (1975a, 1975b) assumed that after the M^+ and e^- have come into the film, the injected e^- is trapped by

W^{6+} forming W^{5+} (i.e. localized on a W atom), and M^{+} remains in an interstitial site. Using an existing theory of intervalence transfer absorption (e.g. in "Prussian Blue" [KFe(II)Fe(III)$(CN)_6$ H_2O], where the optical absorption can be written as $Fe(a)^{2+} + Fe(b)^{3+} + hv \rightarrow Fe(a)^{3+} + Fe(b)^{2+}$ where a and b refer to two different sites), they suggested an intervalence transfer of W^{6+} to W^{5+} for the amorphous WO_3 film during coloration, i.e. the injected electrons were trapped by W^{6+} forming W^{5+}, and H^{+} remained ionized in interstitial sites. Energy was required to raise the electron from one tungsten site over a barrier to another W site. The transition in the WO_3 film could be similarly represented as $W^{5+}(a) + W^{6+}(b) + hv \rightarrow W^{6+}(a) + W^{5+}(b)$, where hv was the photon energy absorbed by an electron at a site. Figure 2.4 shows this theory schematically.

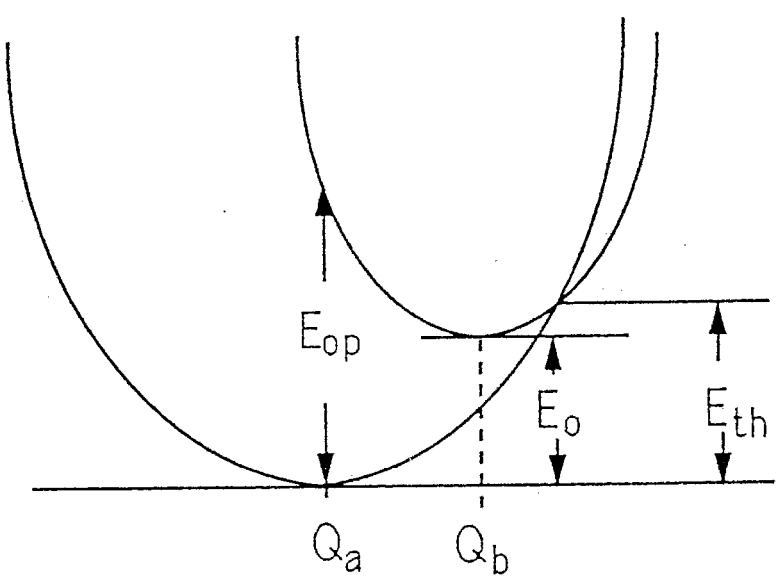

Fig. 2.4 Intervalence transfer of the electron from W^{6+} to W^{5+}

E_{op} = energy at the peak of the optical absorption band.

E_{th} = energy for thermal activation (hopping) of an electron from site a to site b.

E_o = difference in ground state energy between site a and b.

Q_a, Q_b = coordinates for the electron on site a and b.

The trapped electron at site a(W^{5+}) can be excited into a nearest site b(W^{6+}) by absorbing a photon with energy $\geq E_{op}$ and then undergoing a radiationless transition (phonon emission) to localize on Q_b. By comparing with the experimental data, the width of absorption band, oscillator strength, and the energies listed above can be qualitatively expressed in terms of this model. However, this model could not explain the high, almost metallic values of electronic conductivity in the colored A_xWO_3 films at high x (>0.32) value as observed by Crandall and Faughnan (1977). Also the theory suffers from the fact that Pfiter and Sichel (1980) could not find any presence of W^{5+} in an electrochemically colored amorphous H_xWO_3 film using ESR, causing them to reject the intervalence transfer model. A modified intervalence transfer model was developed by Schirmer et al (1977). This model was basically the same as that suggested by Faughnan et al (1975a, 1975b) with the addition of a local structure distortion being brought about by the electron trapping and W^{5+} formation lowering the energy of the occupied state relative to the unoccupied state of the surrounding W^{6+}. Schirmer et al (1977) also reported that the amorphous state was necessary for electron localization and W^{5+} formation to occur.

Drude model

The optical absorption in colored WO_3 films can also be more generally interpreted as being predominantly due to free electrons. The dependence of free electron absorption on the free carrier density can be described by the classical Drude model (e.g see Goldner et al 1983):

$$\epsilon = \epsilon_1 + i\epsilon_2 \qquad (2.1)$$

$$\epsilon = (n + iK)^2 = n^2 - K^2 + i2nK \qquad (2.2)$$

where ϵ_1 and ϵ_2 are respectively the real and imaginary parts of the dielectric constant ϵ, n is refraction index and K the extinction coefficient. ϵ_1 and ϵ_2 can be further expressed as

$$\epsilon_1 = 1 - w_p^2\tau^2/(1+w^2\tau^2) \qquad 2.3$$

$$\epsilon_2 = w_p^2\tau/w(1+w^2\tau^2) \qquad 2.4$$

where w_p is the plasma resonance frequency and determined by the free electron density n_e:

$$w_p^2 = n_e e^2/\epsilon_o m^* \qquad 2.5$$

where m^* is the electron effective mass. The absorption coefficient is related to K by

$$\alpha = 4\pi K/\lambda = 2wK/c \qquad 2.6$$

where λ is the free space value of the light wavelength and c the speed of light in free space. Combining equations 2.1 to 2.6, we obtain

$$\alpha = w_p^2 \tau / nc(1+w^2\tau^2) = n_e e^2 \tau / \epsilon_o m^* nc(1+w^2\tau^2) \qquad (2.7)$$

which we can use measured values of the host matrix refractive index n to obtain absorption coefficient. The classical Drude model does not consider the detail electronic structure at the atomic level, but suggests a free electron behavior, into which the effects of phonon or ionized defect scattering and interaction of free carriers are incorporated by a frequency-dependent relaxation time, $\tau = \tau(w)$. Using this model, Schirmer et al (1977) were able to obtain a good fit to the experimental absorption data of polycrystalline WO_3 films. Goldner et al (1983, 1985) further reported that the Drude model could be used to fit both absorptivity and reflectivity of rf sputtered polycrystalline WO_3 films. They measured the absorption and reflection of the WO_3 films colored by Li^+ cation (1M $LiClO_4$ in propylene carbonate as electrolyte), and confirmed that the free electrons dominate the behavior of electrochromic polycrystalline WO_3 films. Meanwhile, Svensson and Granqvist (1985) studied the application of amorphous WO_3 film in "smart windows" and found that the Drude-model gave a good explanation for the experimental data. But the micro-mechanism of the electrochromic process in WO_3 films was still left as an open question.

2.4 Electrochemical studies in EC devices

As discussed above, the blue coloration in a tungsten oxide film is produced by ion-electron double insertion in an electrochromic device. An EC device is basically a battery, except for the visible coloration. As depicted by figure 2.3, many physical or electrochemical processes may be responsible for governing the kinetics of coloration and bleaching behavior in an EC cell. The cell's parameters: optical contrast, response time, chemical reversibility, and life time, are closely related to these physical and electrochemical processes as well as to the physical and chemical properties of the EC material. In this section, requirements of an EC layer (WO_3 films) in a practical display EC cell are discussed, and special consideration is given to the cell's response time and life time.

The response time is one of the most important parameters in an EC cell. As discussed before, the coloration and bleaching processes include the transport of electrons at the counter (Li metal) and the working (WO_3 EC layer) electrodes, the migration of cations in the electrolyte, and the diffusion of the neutral atoms in the working electrode. The response time will be determined by the total time spent in these steps. However, among these processes, those with a fast speed can be ruled out as rate controlling. In an EC cell both counter electrode and the working electrode are electric conductors (the WO_3 film is a mixture of electron and ion conductor), the transport speed of electrons at the counter electrode and the working electrode should be very fast compared with the other processes (Yamada et al 1983). The ion diffusion in the electrolyte can be made fast by using fast ion conductors and thin layers. It is also

known that the diffusion speed of Li^+ in the electrolyte is several orders of magnitude higher than that in the WO_3 films (Mohapatra 1978). Ho et al (1980) showed that in the case of H^+, Li^+ or Na^+ based EC cells, the diffusion of H, Li or Na atoms inside the WO_3 host matrix controlled the coloration/bleaching speed except at the very beginning of the process. At short times, the coloration/bleaching process was mainly controlled by the transport of active species (H^+, Li^+ or Na^+) across the WO_3/electrolyte interface barrier (Faughnan et al 1975b; Crandall et al 1976). Typical diffusion coefficients of H, Li and Na in the WO_3 films are listed in table 2.2.

Table 2.2 Diffusion coefficients of various ions in WO_3 films

system	chemical diffusion coefficient	Ref
H_xWO_3	10^{-10} cm^2/sce	(Morita 1982)
Li_xWO_3	10^{-13} cm^2/sec	(Mahapatra 1978)
Na_xWO_3	10^{-16} cm^2/sec	(Dautremont-Smith et al 1977)

Faughnan and Crandall (1980) reported that the response time (for optical contrast change of 1:4 or 1:12) of an EC cell with hydrogen insertion was about 1 to 4 seconds and Mahapatra (1978) estimated the response time with lithium insertion was about 10 seconds. It was understood that the response time of an EC cell is dependent on the sizes of injected atoms and the structure of the WO_3 host. To improve the response time for EC cells, Matsuhiro and Masuda (1980) reported a new evaporation procedure in

which the WO_3 films were evaporated at a relatively high background pressure (>6 x 10^{-4} torr) of dry nitrogen. The films so deposited were of low density (<0.55 bulk density) and high porosity, thus explaining the improved rate of atom insertion and extraction. In a symmetric sandwich configuration: ITO(indium doped tin oxide)/WO_3/$LiClO_4$ in propylene carbonate (PC)/Li_xWO_3/ITO cell, the coloration/bleaching time was about 0.5 second for an optical density change of 0.9 at 633 nm. However, the stability of such deposited films needed improvement. Searching for either a new phase of tungsten oxide or tungsten compounds with different structures could be rewarding.

Long term stability of the EC cell over many cycles (coloration/bleaching cycles) is crucial for a commercial cell in the real market. Usually a EC cell can be run as many as 10^4 cycles (Scholotter 1987) to 10^7 cycles (Kazusuke 1986). Randin (1978) has investigated the chemical and electrochemical stability of evaporated WO_3 films in various aqueous and non-aqueous electrolytes. His evaporated films showed a dissolution rate of 25 Å per day when immersed in an electrolyte of 10:1 glycerin:H_2SO_4 within a sealed ampule at 50 °C. In aqueous 1N H_2SO_4 the dissolution was appreciably faster because of WO_3 dissolution in water (Arnoldussen 1981):

$$WO_3 + H_2O \longrightarrow 2H^+ + WO_4^{2-} \qquad (2.8)$$

The dissolution problem can be greatly reduced by using Li^+ or Na^+ based non-aqueous or even solid electrolytes (e.g. $LiClO_4$ in propylene carbonate, Li_3N and Na^+-β-Al_2O_3). The WO_3 film was found much more stable in aprotic electrolytes (Randin 1978). The only problem encountered with

using Li^+ and Na^+ based electrolytes was the slow response time. The moisture incorporated in the WO_3 films during the preparation also aroused attention. Knowles (1978) reported that in an evaporated $WO_3/LiClO_4$ in propylene carbonate EC cell, the optical contrast gradually decreased during a fixed time potentiostatic coloration pulse, and this so called aging effect could be restored to close to its initial performance by UV illumination of the WO_3 film while held in the bleached state. It has been suggested that the presence of water in the WO_3 film was responsible for the observed degradation in the performance. Schlotter and Pickelmann (1979, 1980) studied the behavior of evaporated WO_3 films in Li^+ and Na^+ non-aqueous electrolytes and found that some Li or Na content not making a contribution to the coloration was present in the bleached state. This residual Li or Na content increased with both the number of the coloration/bleaching cycles and the depth of the coloration. They explained this phenomena as results of the reaction between inserted Li or Na and absorbed water in the film.

2.5 Statement of objectives

The EC property of WO_3 films has been studied for about twenty years. However, as discussed in Chapter 1 and this chapter, several important aspects of fundamental understanding in the EC property of WO_3 films were still incomplete and unclear. In the past most studies used amorphous WO_3 films and concentrated on the optical absorption changes; there was a lack of direct studies on crystal structures of either hydrogen or lithium tungsten bronze. The tungsten bronze model was generally accepted, but little was known about these formed tungsten bronzes. It is generally

understood that the optical absorption, electrical conductivity and many other physical properties of a material are strongly dependent on its crystal structure. To explain the tungsten bronze formation process, knowledge of the crystal structures of tungsten bronzes is essential. In this thesis, based on the studies with polycrystalline WO_3 films and WO_3 powder, the formation processes of hydrogen and lithium tungsten bronzes were intensively investigated. This thesis will discuss the crystal structures of hydrogen and lithium tungsten bronzes formed in the coloration process, the dependence of these crystal structures on hydrogen and lithium concentration, and the conditions under which the coloration/bleaching process is reversible. In order to improve the response time of the EC cell, it seems necessary to develop some new tungsten compounds suitable for fast ion insertion. Two new EC materials: hexagonal cesium tungsten oxides and pyrochlore cesium tungstate will be discussed in this thesis.

Chapter 3

Theoretical background for electrochemical analysis of EC cells

Electrochromism in WO_3 materials is basically an electrochemical reaction of electroactive species with the host lattice matrix. During coloration, the main happening is the active species intercalation into the WO_3 EC electrode. In this chapter, the general thermodynamic property of an EC cell and the ion transportation behavior inside the EC electrode will be discussed.

3.1 Gibbs free energy and EMF of an EC cell

Consider the general EC cell shown in figure 2.3, in which the active species Li can be ionized at the Li anode and migrate across the electrolyte and then be inserted into the WO_3 layer to form Li_xWO_3. The thermodynamic state of the EC cell is usually a function of temperature, T; pressure, P; and the molar number of active species i, n_i. The change in internal energy of the system can be described by:

$$\delta U = \delta Q + \delta W + \Sigma_i \mu_i \delta n_i$$

were $\delta Q = T\delta S$ is the heat absorbed by the system; $\delta W = -P\delta V$ the mechanical work done by the system; $\mu_i = (\delta U/\delta n_i)_{S,V,n}$ the chemical potential of species i, thus the δU can be rewritten as:

$$\delta U = T\delta S - P\delta V + \Sigma_i \mu_i \delta n_i \qquad (3.1)$$

where V is the volume. In an EC cell, the changes in heat and in volume are commonly neglected, so it is convenient to describe the system with Gibbs free energy G:

$$G = \Sigma_i \mu_i n_i \qquad (3.2)$$

by the Gibbs-Duhem equation:

$$S\delta T - V\delta P + \Sigma_i n_i \delta \mu_i = 0 \qquad (3.3)$$

the change in G can be obtained as:

$$\begin{aligned} \delta G &= \Sigma_i n_i \delta \mu_i + \Sigma_i \mu_i \delta n_i \\ &= -S\delta T + V\delta P + \Sigma_i \mu_i \delta n_i \end{aligned} \qquad (3.4)$$

At constant temperature ($\delta T = 0$) and pressure ($\delta P = 0$), δG is given by

$$\delta G = \Sigma_i \mu_i \delta n_i \qquad (3.5)$$

As is discussed in the previous chapters, an EC cell is not more than a battery except for the visible color change. In a Li based EC cell the initial open circuit voltage between the WO_3 working electrode and the Li metal counter electrode is about 3.0V. This voltage, also called EMF (the electromotive force), can be measured by a compensation method, i.e. by

balancing it against a voltage of equal magnitude and opposite sign. The EMF of an EC cell can also be measured simply using a voltmeter with a high input impedance. During the coloration, corresponding to a battery discharge, the active species (eg. Li^+) transfer from anode to cathode within an EC cell and the electrons pass through the external circuit under the cell's electromotive force. The work done by the EC cell on a external circuit in this case is $E\delta q$ if E is the cell's voltage (EMF), and δq the total charge of electrons passed through the external circuit. The quantity δq can be expressed as $\delta q = ez\delta n$, where e is the basic electronic charge, z the valence of the active species, and δn the total number of the active species transferred from cathode to anode. If the coloration is a reversible process, the work done to the environment must accompany the decrease of Gibbs free energy in the cell:

$$\delta G = - ezE\delta n \qquad (3.6)$$

Referring to equation (3.5) and considering only one kind of active species, the Gibbs free energy of an EC cell system is also given by

$$\delta G = (\mu_{cathode} - \mu_{anode})\delta n \qquad (3.7)$$

where $\mu_{cathode}$ and μ_{anode} are the chemical potential of the active species at the cathode and anode, respectively. Equation (3.7) gives the Gibbs free energy change upon one active species moving from the anode to the cathode (if $\delta n = 1$). Hence the EMF of an EC cell is related to the chemical potential by

$$E = -(1/ze)(\mu_{cathode} - \mu_{anode}) \qquad (3.8a)$$

In studying lithium intercalation the anode is usually lithium metal and so the chemical potential of lithium at the anode is a constant. Equation of (3.8) can be written as

$$E = -(1/ze)(\mu_{cathode} - \text{constant}) \qquad (3.8b)$$

Equation (3.8) shows that the EMF of an EC cell results from the different chemical potential of the active species of valence z at the cathode and at the anode. The EMF of an EC cell may therefore be regarded as a qualitative measure of a tendency towards reaction, as may also be the change in the Gibbs free energy δG.

3.2 Nernst equation and electrochemical determination of thermodynamic properties

The purpose of this thesis is to study the thermodynamic behavior of ion insertion into the cathode host, and thus it is useful to bring a basic electrochemical equation, the so called Nernst Equation as well as some other thermodynamic relations into this discussion.

3.2.1 Nernst equation

The chemical potential of an active species can be further expressed as

$$\mu_i = \mu^0 + KT\ln\alpha_i \qquad (3.9)$$

where K is the Boltzmann constant, and α_i the activity of species i. μ^0 is the chemical potential of the species at a standard state ($\alpha_i = 1$). Substituting equation (3.9) into (3.8b), one obtains

$$E = E^0 - (KT/ze)\ln(\alpha_{cathode}) \qquad (3.10)$$

which is a form of the Nernst equation where E^0 includes every constant and can be treated as the initial potential of the cathode with respect to a defined standard potential (initial cell's EMF).

3.2.2 Thermodynamic relations

In a practical EC cell, the EMF of the cell and the current passing through the cell are the only electrical parameters that can be measured. It will be shown that most thermodynamic properties of an EC cell can be obtained from basic relations of EMF to the Gibbs free energy and other thermodynamic parameters. First of all it is useful to introduce a semiempirical expression for the EMF-x (x is the stoichiometrical parameter of the active species in the cathode host such as Li_xWO_3). The x in experiments is related to the total current and the time during which the current passes through the cell:

$$x = \frac{M_c}{zFm_c}\int_t Idt \qquad (3.11)$$

where M_c is the molecular weight of the cathode host and m_c is the mass of the cathode and the F is the Faraday's constant. Consider n atoms entering

into a system with N sites, a simple relation for EMF-x can be obtained from the following assumptions:

(i) there is no interactions between the intercalated atoms;

(ii) no more than one atom can occupy a given site;

(iii) the energy for all sites is the same.

In this case, the entropy of the system is just K (the Boltzmann constant) times the number of ways to put n distinguishable atoms into N sites:

$$S = K\ln\left(\frac{N!}{n!(N-n)!}\right) \approx K\ln\left(\frac{N^N}{(n^n)(N-n)^{N-n}}\right) \qquad (3.12)$$

where Stirling's approximation (for large N)

$$N! \approx (\sqrt{2\pi N})N^N e^{-N} \approx N^N$$

is used to simplify the expression for the entropy S. Suppose that n_0 intercalated atoms make the stoichiometric parameter x equal to 1, then we have $x = n/n_0$ and $x_{max} = N/n_0$, and the entropy S can be further written as

$$S = -K[x\ln x - x_{max}\ln x_{max} + (x_{max} - x)\ln(x_{max} - x)] \qquad (3.13)$$

Because the energy for every site is the same, the total internal energy is then

$$U = nu_0 \qquad (3.14)$$

where u_0 is the energy of one atom in the site. With the Helmholtz free energy $F = U - TS$ and the chemical potential $\mu = (\delta F/\delta n)_{T,V} = (\delta F/n_0 \delta x)_{T,V}$, we have

$$F = n_0\{xu_0 + KT\{x\ln x - x_{max}\ln x_{max} + (x_{max} - x)\ln(x_{max} - x)\} \quad (3.15)$$

and

$$\mu = u_0 + KT\ln[x/(x_{max} - x)] \quad (3.16)$$

From (3.8b) and (3.16), the relation for EMF-x is then

$$E = E^0 - (KT/ze)\ln[x/(x_{max} - x)] \quad (3.17)$$

Equation (3.16) shows an important relation between the chemical potential and the concentration of an active species in the cathode. The chemical potential of the active species will increase when the concentration increases. This means that the electrical potential of the cathode will decrease with respect to a standard reference electrode. If the interaction between the inserted atoms is considered, one more term should be added in the EMF-x expression (Armand 1978, Mckinnon 1980):

$$E = E^0 - r(x/x_{max}) - (KT/ze)\ln[x/(x_{max} - x)] \quad (3.18)$$

where $r(x/x_{max})$ is the interaction term between the inserted atoms, and r is positive for repulsive interaction. For the repulsive interaction (r >

0), the electrical potential of cathode drops much faster than non-interaction (r = 0). Further discussions for EMF-x relations has been made by Mckinnon (1980).

3.2.3 Phase analysis

Equations (3.17) and (3.18) show that the EMF (or the Gibbs free energy) of a cell is a function of the contents of the active species in the cathode. For a system of k canonical components and m phases, the Gibbs phase rule predicted that the number of independent intensive variables is determined by (e.g. see Hutchinson 1962):

$$f = k + 2 - m \tag{3.19}$$

where f is also called the freedom of the system. In a binary system, k = 2, and if only one phase exists, m = 1, then the system has three independent intensive variables: temperature T, pressure P and the free energy G. In a real experiment, the temperature T and the pressure P is fixed, so G as well as the EMF of the cell is the only variable which can be varied with the insertion or extraction of the active species. In this case the system is said to have one degree of freedom. In our case, the cathode Li_xWO_3 can be treated as binary system, the Li forms one part and the WO_3 forms another part in this system. In the experiments, a constant current is forced to pass through the cell, if only one phase exists in the cathode, the EMF of the cell can vary with the time caused by the content changes of the active species Li in the Li_xWO_3 system. When two phases exist in the cathode (in this case k = 2 and m = 2), according to

equation (3.19), the independent intensive variable f reduces to two. Obviously the free energy G of the system will be invariant if the temperature T and the pressure P on the system is fixed, thus the EMF of the cell has to be a constant even though the content of the active species Li in Li_xWO_3 varies with time. If the EMF of the cell is recorded as the function of the time, a plateau should be observed when more than one phase appears in the cathode.

3.3 Coulometric titration analysis

The qualitative knowledge of the transport kinetics of the considered species in solids is of importance for understanding the transport mechanism and the behavior of inserted species in the cathode. A coulometric titration technique offers was used to analyze the transport property of active species in the cathode: the hydrogen and lithium diffusion coefficients in the EC materials. In this section, a basic principle of coulometric titration technique is described.

According to equation (3.8a) and (3.18) the cell voltage EMF at equilibrium is a measure of the chemical potential difference between the cathode and the anode. If one considers a constant electric current pulse driven through the cell by an external source: the cations inside the electrolyte will move across the electrolyte/cathode boundary and become neutralized by injected electrons. In a short period, these neutralized active species will accumulate at the boundary and cause a concentration gradient inside the cathode. This concentration variation then leads to a cell voltage change δE (see the expression (3.8a) or (3.8b)). The

concentration gradient will eventually disappear by chemical diffusion of the active species after the current pulse and the cell voltage will reach a new equilibrium value as is depicted by figure 3.1.

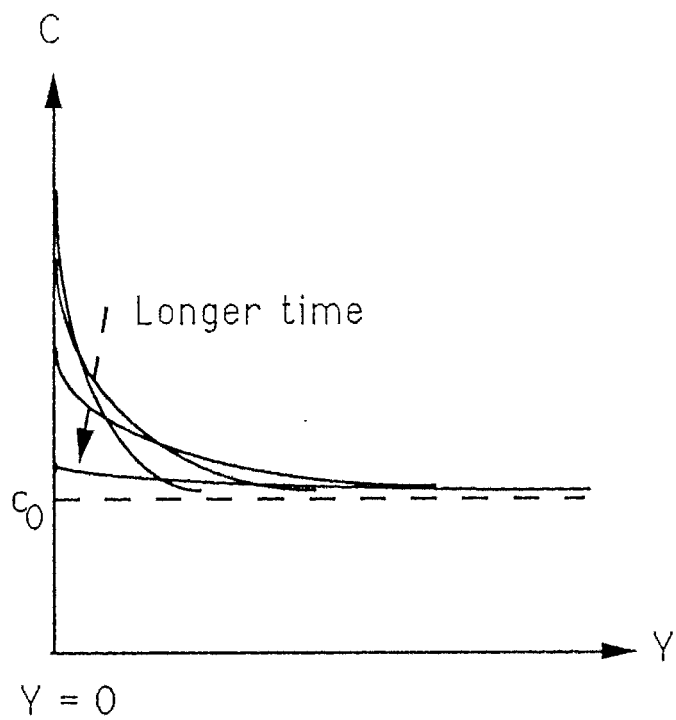

Fig. 3.1 The profile of inserted atom concentration in the cathode.

The concentration gradient profile of the active species inside the cathode can be obtained through Fick's second law:

$$\frac{\delta c}{\delta t} = \frac{\delta}{\delta y}\left[D\frac{\delta c}{\delta y}\right] \tag{3.20}$$

where D is the chemical diffusion coefficient of the active species inside the cathode and y is the direction normal to the surface of the cathode with y = 0 at the electrolyte/cathode boundary. The initial and boundary conditions are:

$$c = c_0 \quad (0<z<L) \qquad \text{for } t = 0 \tag{3.21}$$

$$\left.\frac{\delta c}{\delta y}\right|_{y=0} = \frac{-I}{DSze} \qquad \text{for } t \geq 0 \tag{3.22}$$

$$\left.\frac{\delta c}{\delta y}\right|_{y=L} = 0 \qquad \text{for } t \geq 0 \tag{3.23}$$

where I is the constant current, s the surface area of the cathode attached to the electrolyte, and L the thickness of the cathode film. At t = 0, the concentration of active species is a constant inside the cathode as it is indicated by (3.21). During the current pulse, the concentration gradient is proportional to the current I, but inversely proportional to the diffusion coefficient D and the surface area S in equation (3.22). A semi-infinite boundary condition is represented by equation (3.23) which suggestes that no active species go through the film. Using the relation:

$$\frac{\delta(c/N_A)}{V_m} = \delta x$$

equation (3.20) can be solved. The solution with these conditions is (Weppner and Huggins 1977):

$$\frac{\delta E_t}{\delta \sqrt{t}} = \frac{IV_m}{FS(\sqrt{D\pi})} \left[\frac{\delta E_x}{\delta x}\right] \qquad \text{for } t \ll L^2/D \qquad (3.24)$$

where I represents the imposed current, V_m the molar volume of the cathode material, F the Faraday's constant, x the stoichiometric parameter, S positive cathode surface, N_A Avogadro's constant, D the chemical diffusion coefficient, $[\delta E_t/\delta\sqrt{t}]$ the local slope of the coulometric titration curve upon the current pulse and $[\delta E_x/\delta x]$ the derivative value of EMF–x curve. As we can see in this equation that, if the slope of E_t vs $\sqrt{t}$ is constant during the current pulse, the chemical diffusicn coefficient of the considered species is then able to be calculated from measured slope of $\delta E_t/\delta\sqrt{t}$ and derivative value of $\delta E_x/\delta x$. An example of coulometric titration curve is illustrated in figure 3.2. It should be point out that the current step mothed discussed does not consider any phase change in the host. The diffusion coefficient measured with this method has the meaning only when the host is in a single phase region during the intercalation.

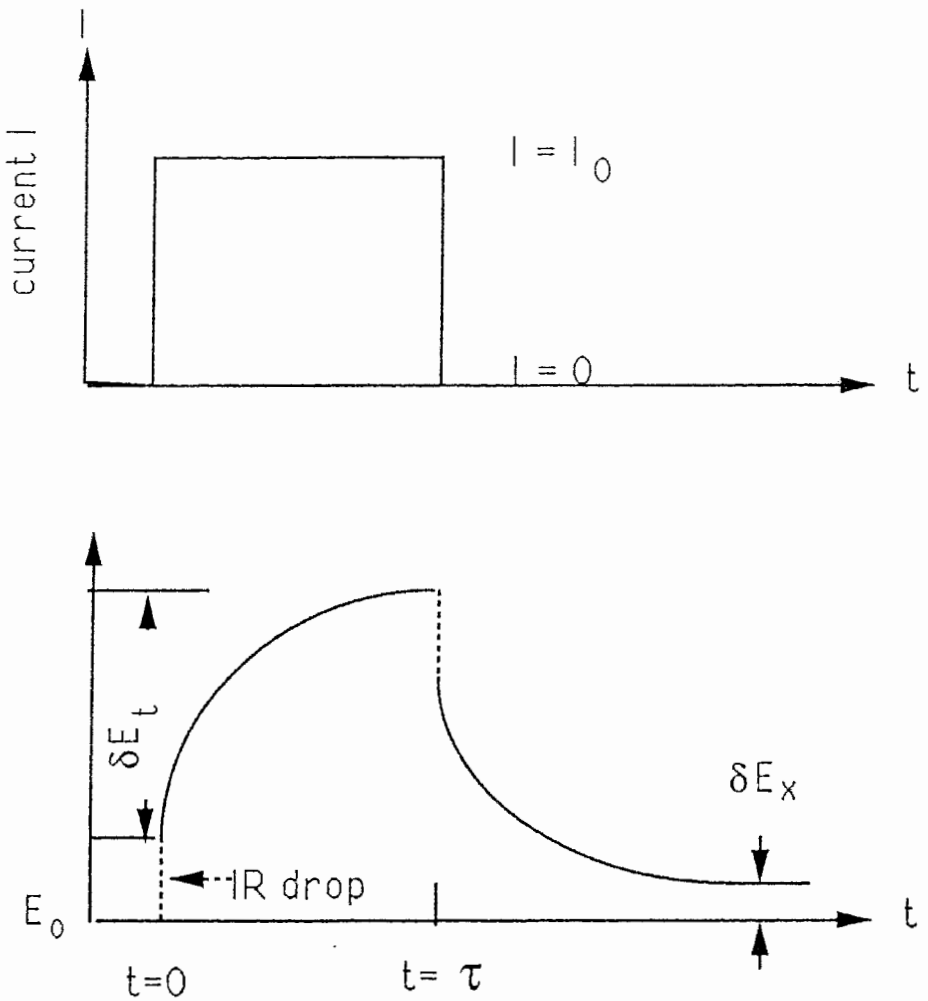

Fig. 3.2 The coulometric titration curve, where δE_t is the transient potential change due to the current pulse and the accumulation of active species at the cathode surface; δE_x is the EMF change of the cell for two different equilibrium states.

Chapter 4

Experimental techniques

In this thesis, we investigated the EC properties of tungsten trioxides, WO_3 and two cesium tungsten compounds: hexagonal $Cs_{0.30}WO_3$ and pyrochlore $(Cs_2O)_{0.4}W_2O_6$. The studies included electrochemical cell design, source material and EC layer preparation, electrochemical analysis, and crystal structure determination. Since the electrochemical cells are the basic tools used in this study, the structures of various electrochemical cells will be first described in detail. Then the system used to obtain reliable EMF-x data, the basic techniques used in the powder X-ray diffraction experiments and the principle of X-ray profile refinement will be discussed. Some other techniques used to characterize the EC materials will also be briefly described.

4.1 The construction of electrochemical cells

Three types of EC cells were used in this work. The first type was a traditional three electrode electrochemical cell which was mainly used to study hydrogen intercalation. Figure 4.1 shows the structure of this cell. Thin layers of tungsten trioxides or tungsten compounds were used as the

working electrode (also the cathode in the cell), Pt foil was used as the counter electrode and SCE (saturated calomel electrode) as the reference electrode.

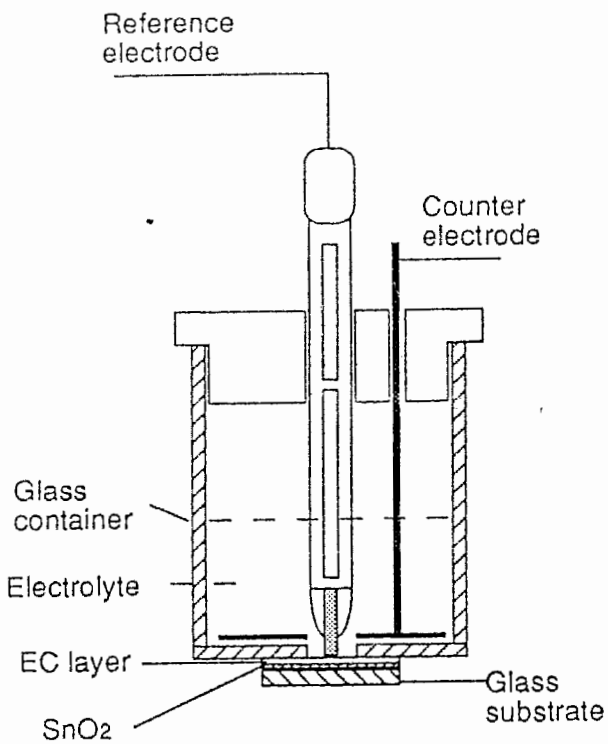

Fig. 4.1 The traditional electrochemical cell used in studying the hydrogen intercalation into EC layers with SCE as the reference electrode, EC layer as working electrode and Pt foil as counter electrode.

The electrolyte containing H^+ was usually a solution of 10% H_2SO_4 in water. In the experiments, the current source was connected to the cell through the working and the counter electrodes. The voltage between the working electrode and the reference electrode was measured as the electrochemical potential of the working electrode. This voltage is also known as the electromotive force (EMF) of the cell.

The second type of EC cell was used to study lithium intercalation into EC layers. In this cell, the EC layers (tungsten oxides or compounds) were also the working electrodes, but the lithium foil worked as both counter and reference electrode. Figure 4.2 shows the structure of the cell.

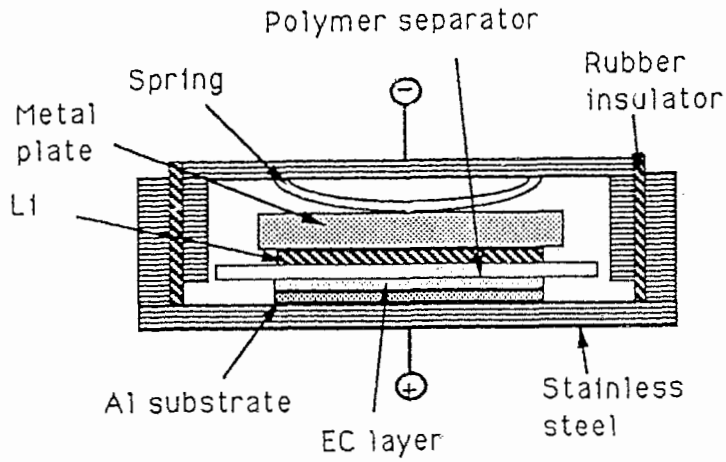

Fig. 4.2 Structure of the battery cell used in lithium intercalation.

A porous polymer sheet (polypropylene, Celgard 2502 from Celanese Corp.) which could absorb 50% electrolyte in volume was inserted between the working and counter electrode as a separator. The electrolyte with Li^+ was made of 1M $LiClO_4$ in propylene carbonate (PC) or in 50:50 volume mixture of propylene carbonate (PC) and ethylene carbonate (EC). As is shown in figure 4.2, the cell were finally sealed in a bottom battery shell so this kind of cell will be called a battery cell in later chapters. To prevent the lithium species from reacting with oxygen and moisture in air, the cell was constructed in an argon filled glove box (VAC Model HE-493, U.S A.). In the experiments, the current source was connected to the cell through the steel electrodes and the voltage measured between the two electrodes was recorded as the EMF of the cell. The electrochemical potential of lithium in the original EC layers is usually much lower than that in Li foil, thus the spontaneous process in the battery cell is that the Li atoms ionize (oxidize) at the interface of Li (foil)/electrolyte and the Li^+ ions neutralize (reduce) at the interface of electrolyte/EC layer. Therefore, the Li foil in the battery is also called the anode and the EC layer the cathode in this thesis.

The third type of EC cell used in the X-ray diffraction studies is shown in figure 4.3. The structure of this cell was basically the same as the battery cell: the EC layer was the working electrode (cathode) and the lithium foil was the reference and the counter electrode (anode). The distinguishable difference of this cell was that the crystal structure changes in the EC layers could be readily detected by the X-ray experiment throughout the beryllium windows in the cell. As shown in figure 4.3, the cell was sealed in between the Be sheet and the stainless steel holder.

The X-ray beam could pass through the Be window without significant energy loss in the experiments. This cell is frequently used in this thesis and will be called the X-ray cell in later parts of this thesis. By means of the X-ray cell, the crystal structures of tungsten oxides and compounds could be detected at any moment during the lithium intercalation.

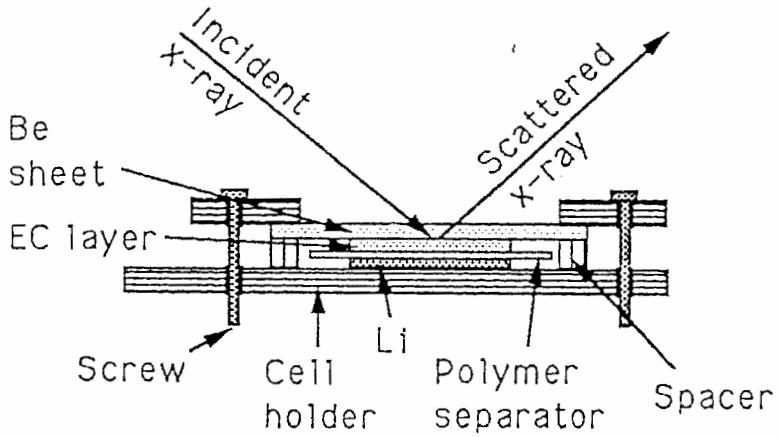

Fig. 4.3 The X-ray cell used in the structure analysis of the EC films upon lithium intercalation.

4.2 EC layer and electrolyte preparations

Films prepared by evaporation

Two kinds of EC layer were used in our EC cells, the first one was a transparent thin film prepared by evaporation and the other a powder film prepared by a spread method with some special tools. The transparent films were evaporated in a vacuum system at about 1 ~ $5x10^{-5}$ torr. The substrates used were SnO_2 coated glass, Al foil, and the Be metal sheet. In evaporating WO_3 films, the substrates were usually kept at room temperature. When evaporating Cs_xWO_3, the substrates have to be heated to about 300°C to prevent the films from peeling off. The film thicknesses were in the range from 300 nm to 2000 nm. Most evaporated films were amorphous and became polycrystalline after annealed at 400°C to 600°C in air. As this thesis is mainly concerned with the EC property of WO_3 and tungsten compounds in relation to their crystal structures, only polycrystalline films were used.

Powder film preparations

The lithium intercalation in WO_3 powders was also investigated. For this purpose, powder films were prepared for insertion into an electrochemical cell. The source material was made of 5 g WO_3 powder, 0.5 g carbon black which ensures good electrical contact between the powder particles, 0.1 g EPDM (Ethyl Propylene Dyne Molemer) binder, and a certain amount of cyclohexane. After thoroughly mixing these components, this material was spread onto a substrate such as Al foil or stainless steel sheets with a

special spreader which is shown in figure 4.4. The powder film prepared in this way was of good adhesion to the substrate. Usually a 1.2 cm x 1.2 cm powder film with Al or stainless steel foil was cut and inserted into the battery cell or the powder films of the same size were peeled off the substrate and inserted into the x-ray cell. The powder films made by this method had densities around 15 to 25mg/cm^2.

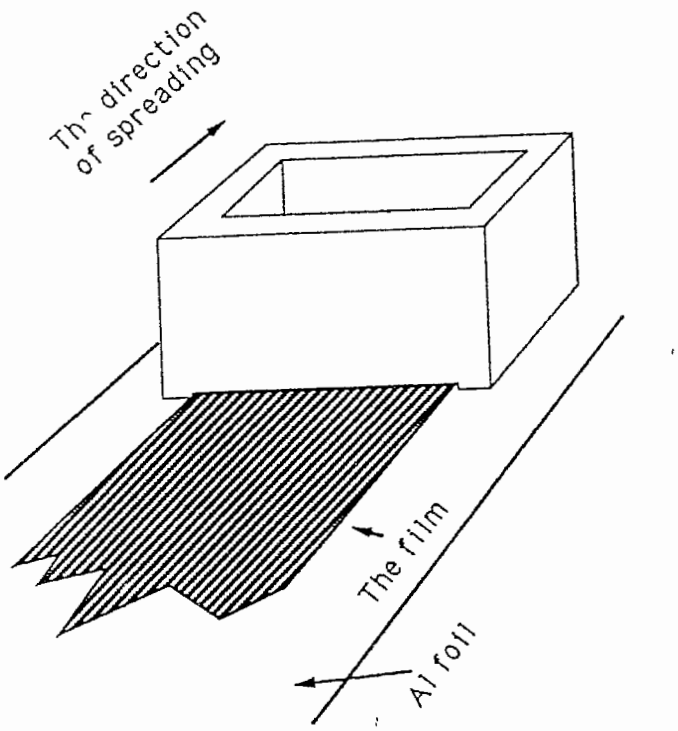

Fig. 4.4 The spreader used to prepare powder films

Electrolyte preparations

The hydrogen based electrolyte consisted of 10% H_2SO_4 in deionized water. Other electrolytes containing H^+ were also used, such as poly-AMPS (2-acrylaino-2metheyl-1-propane-sulfonic acid). The electrolyte containing Li^+ ions is consisted of 1M $LiClO_4$ in propylene carbonate (PC) or a 50:50 volume mixture of propylene carbonate (PC) and ethylene carbonate (EC). The $LiClO_4$ was first dried at 120 °C in a vacuum of about $1x10^{-2}$ torr for 24 hours before being dissolved in the PC or PC/EC. The PC and EC were vacuum distilled at least twice to eliminate the water contamination. The lithium based electrolyte was prepared and kept in an argon filled glove box (VAC Model HE-493 U.S.A.).

The EC layer pre-treatments

The EC layers (the powder films or evaporated films) used in the EC cells usually have rough surfaces which could prevent the electrolytes from uniformly attaching to the EC layer. On the other hand, there might be some porous structure in the layer; air or argon stored in the porous structure could reduce the real surface area between the EC layer and the electrolyte. In order to ensure good physical and electrical contact between the electrolyte and the EC layer, the EC layers used in EC cells were all pre-treated. The EC layers were first immersed in electrolytes (say the 1M $LiClO_4$ in PC/EC) in a container and then the argon in the container was evacuated to about 2×10^{-3} torr for about 10 minutes to ensure that the gasses (air or argon) in the EC layer were mostly removed. After evacuation, the container was refilled with argon at a pressure of 8

kg/cm^2 for another 10 minutes to eliminate any air gap between the electrolyte and the EC layer. In the battery and X-ray cell, a porous polymer sheet was used as separator to absorb the electrolyte. The procedures used to have the polymer separator absorb the electrolyte was the same as that used for the EC layers.

4.3 Electrochemical techniques for thermodynamic property determination

It has been known that thermodynamic properties of the EC cell can be obtained from the EMF-x curve at constant temperature and pressure. The EMF of an original EC cell depends on the property of the EC layer, the active species, electrolyte and the reference electrode. The EMF–x curves were obtained by applying a small constant current to the cell, and recording the voltage across the cell at the same time. The current was usually very small so that at each moment, the cell is considered to be in the quasi-equilibrium state and the voltage across the cell was considered as the equilibrium EMF. The x could be calculated by the constant current, the mass of the cathode and the time of current flow (see equation 3.11). For example, for lithium intercalation into a 20 mg WO_3 powder film, if the current selected was 23 μA, then the x change in Li_xWO_3 is $\delta x = 1$ in 100 hours, which we called charge/discharge rate. For an evaporated film 1.5 μm thick, the mass of the film with 1.2 cm x 1.2 cm was about 1.3 mg, thus the current for a 100 hour rate was 1.5 μA or for 50 hour rate was 3.0 μA. In this thesis, the EMF–x data were collected by a computer system which is shown in figure 4.5.

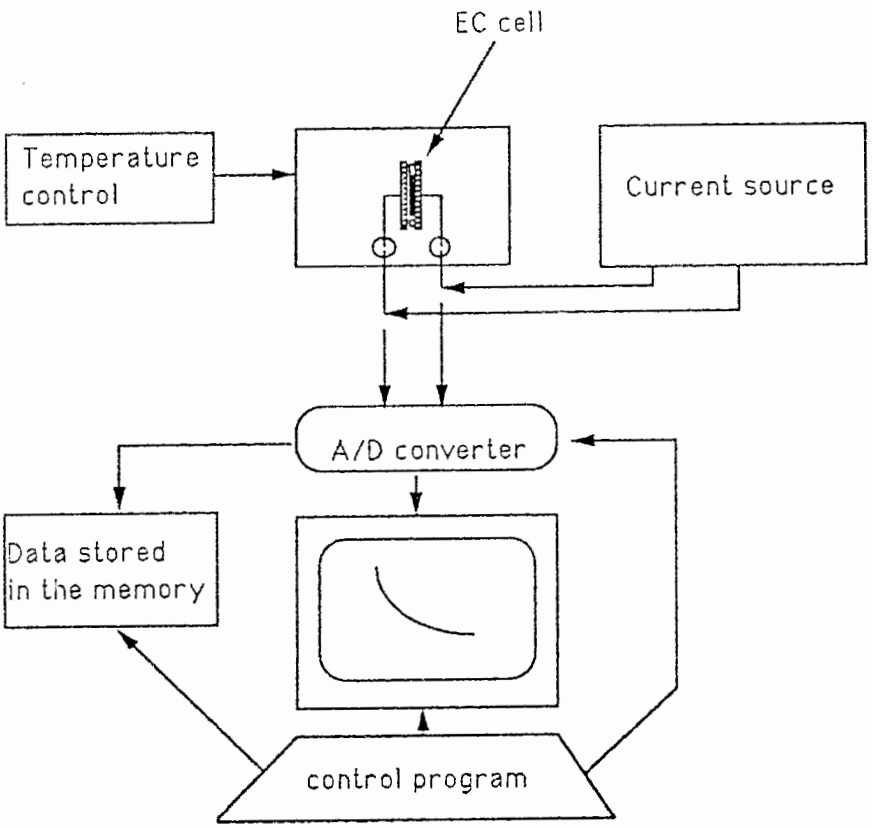

Fig. 4.5 The computer system for EMF–x data collection

The cell was kept at constant temperature (usually 30°C ± 0.1°C) in a thermostat, a program in the computer would record the EMF values whenever the EMF changed by a certain value (e.g 2 mV). The EMF–x data could also be obtained by applying an electric potential across the cell until the current passing through the cell was very small and recording the total charge passing through the cell. A potentiostat/galvanostat (PAR 173 with PAR 179 coulometer) was used in this case.

Another electrochemical analysis was to determine the chemical diffusion

coefficients of the hydrogen and lithium atoms in the EC layer. The chemical diffusion coefficients were measured with PAR 173 potentiostat/galvanostat at control I mode. A constant current (I_o) step of width τ was applied across the cell, a transient voltage response δE_t across the cell arose from the accumulation of active species on the surface of the cathode. After the current pulse, the voltage of the cell would reach a new equilibrium value due to the concentration change of the active species in the cathode. The voltage difference at two equilibrium states before and after the current pulse was recorded as δE_x. In the experiments, the δE_t was recorded as a function of time and δE_x as function of δx. The width of current step τ of 0.5 to 2.0 seconds was used in most cases. The chemical diffusion coefficient D was then calculated from the slope of $\delta E_t \sim \delta/t$ curve and/or from the ratio of $\delta E_t/\delta E_x$ as expressed by equation 3.30.

4.4 X-ray structure analysis

General description

The X-ray diffraction experiments were carried out on an X-ray diffractrometer (Philips PW-1730) using CuKα radiation. For most powder and film samples, the X-ray data were collected using steps of $2\theta = 0.05°$. The counting time at each step was varied from 2 to 40 seconds depending on the intensity requirements. The powder samples were usually finely

grounded and sifted by 44 μm or 100 μm sieves previous to the X-ray diffraction analysis in order to reduce any possible preferred crystal grain orientation. To study the crystal structure of WO_3 powder and film after lithium intercalation, the X-ray cell was used. Since lithium is a very active species, a WO_3 powder or film with inserted lithium can not be opened to the air otherwise the inserted lithium will quickly react with the oxygen and moisture in the air. For the structure analysis of the WO_3 film after hydrogen intercalation, the films with intercalated hydrogen were taken from the EC cell and loaded into the x-ray machine with the samples exposed to air. The effects of the air on these samples will be discussed later with the experimental data.

Crystal structure determinations

The crystal structure analysis includes the determination of the unit cell of the Bravais lattice, the space group, and the atom positions in the unit cell. For the Bravais lattice, we need to know the cell's symmetry and dimensions which are related to the peak positions and indices in the X-ray diffraction pattern. The method to determine the dimensions of the unit cell can be found in textbooks (e.g. see Lipson and Steep 1970). To determine the space group and the atom positions in the unit cell, we need to analyze the intensities of the X-ray diffraction patterns. The intensity of peak (h, k, l) in the X-ray diffraction patterns can be expressed as:

$$I_{h,k,l} = SL_{h,k,l}|F_{h,k,l}|^2 M_{h,k,l} \qquad (4.3)$$

where S is the scale factor, $M_{h,k,l}$ the multiplicity, $L_{h,k,l}$ the Lorentz-polarization factor and the $F_{h,k,l}$ the structure factor:

$$F_{h,k,l} = \sum_{j=1}^{N} g_j \exp[2\pi i(hx_j + ky_j + lz_j)] \qquad (4.4)$$

where the g_j is the product of the atomic scattering factor f_j and the isotropic thermal vibration factor T_j for the atom j in the unit cell. The sum Σ in equation 4.4 should go over the total atoms (from j = 1 to N) in the unit cell. The atomic scattering factor can be expressed as

$$f_j = \sum_{i=1}^{4} a_{j,i} \exp(-b_{j,i} \sin^2\theta/\lambda^2) + c \qquad (4.5)$$

where $a_{j,1}$ to $a_{j,4}$, $b_{j,1}$ to $b_{j,4}$ and c are constants and related to the characteristic of the atom j. These constants can be found from the X-ray diffraction handbook: "International Tables for X-ray Crystallography" Edited by Henry, N. F. M. and Lonsdale, K. 1965. The thermal vibration factor T_j is

$$T_j = \exp[-B_j(\sin^2\theta)/\lambda^2] \qquad (4.6a)$$

where B_j is the temperature factor of atom j, given by

$$B_j = 8\pi^2\bar{U}^2 \qquad (4.6b)$$

where $\bar{U}^2$ is the mean square amplitude of vibration of the jth atom from its equilibrium position in a direction normal to the reflecting plane. The intensity I_c of (h,k,l) peak was calculated by equations (4.3), (4.4)

and (4.5) and then compared to the observed intensity $I_o(h,k,l)$. In the calculations, the scale factor S, temperature factor B_j and the atomic positions (x_j, y_j, z_j) could be refined until a smallest discrepancy factor R was obtained:

$$R = \frac{\Sigma\left|I_o(h,k,l) - I_c(h,k,l)\right|}{\Sigma I_o(h,k,l)} \qquad (4.7)$$

where the sum should go over whole (h,k,l) peaks observed. The process used to minimize the R factor is called structure refinement. In practical powder X-ray diffraction patterns, the observed peaks are not geometric lines but broadened. Rietveld (1967, 1969) proposed an equation which could be used to fit the practical X-ray diffraction peak profile:

$$\Gamma_{i,c} = \Gamma_{i,b} + \sum_{h,k,l} G_{i,h,k,l} I_{h,k,l} \qquad (4.8)$$

where $\Gamma_{i,c}$ is the intensity calculated at point i (at a certain angle position), $\Gamma_{i,b}$ is the background intensity, $G_{i,h,k,l}$ is a normalized peak profile function, and $I_{h,k,l}$ is the intensity of peak (h, k, l). The total X-ray intensity at point i should consider all (h,k,l) reflections. Based on Rietveld concept, the whole profile of X-ray diffraction pattern could be calculated point by point. Many computing programs have been developed (e.g. by Wiles and Young (1981); Howard and Hill 1986). In this thesis, a computer program named Rietveled profile refinement program, developed by Howard and Hill (1986), was used to analyze X-ray diffraction patterns and to determine the crystal structure. In this computing program three peak profile functions are available: Pseudo-Voigt, Pearson VII and Voigt function which can be used to fit the observed peak shapes (Howard and

Hill 1986). The value of $I_{h,k,l}$ calculated by the program depends on the symmetry of the unit cell, the atom positions in the unit cell, temperature factors of atoms and the total scale factor. All those parameters are adjustable in the program. In producing the refinements, the program reads a control data file with suggested scale factor, space group, atom positions and peak shape, and calculates the diffraction pattern. After comparing the calculated data and the observed data, some parameters are then adjusted by the program in order to reduce the R factor. The process was repeated until the refinement was finished. In this way the crystal structure of the studied material was determined.

The structure refinements in two special cases

As described in section 4.1, to study the lithium intercalation into WO_3, the X-ray experiment was carried out on the beryllium X-ray cell. The x-ray data obtained in this case were associated with the beryllium sheet absorption. Referring to figure 4.3, the intensity change caused by beryllium sheet absorption can be expressed as:

$$I_r = I_o \exp(-2\mu l/\sin\theta) \qquad (4.9)$$

where I_o is the diffraction intensity without the beryllium absorption, I_r the recorded intensity associated with the beryllium absorption, μ the absorption coefficient of the beryllium to the X-ray radiation used, l the thickness of the beryllium sheet and the θ the diffraction angle. In order to use equations (4.3)–(4.8) to refine the crystal structure, the recorded X-ray data I_r should be converted to I_o according to equation (4.9).

The second case considered here is the preferred orientation of crystal grains in the sample, especially in the film samples. When we analyze the X-ray data from the polycrystalline films, some peaks may have extraordinary intensities due to the presence of preferred oriented crystallites in the film. To include preferred orientation into the intensity calculation, the intensity can be expressed as (Rietveled 1969)

$$I_p = I_o \exp(-\alpha^2) \tag{4.10}$$

where I_o is the normal intensity, I_p is the intensity associated with the preferred orientation in the sample and the α the acute angle between the scattering vector and the normal to the surface of the preferred oriented crystallites. The intensity I_p has maximum value when the scattering vector and the normal of the oriented crystallites are in parallel. In the computer program the I_p is expressed as

$$I_p = I_o[P2 + (1 - P2)\exp(P1\alpha^2)] \tag{4.11}$$

where P1 and P2 are refinable parameters. It is obvious that $I_p = I_o$ when P2 = 1 or P1 = 0.

4.5 Other physical and chemical tools

Some other physical and chemical means were also used to characterize the general properties of tungsten oxides and compounds including the measurements in optical absorption, X-ray energy dispersion, thermal gravimetric analysis (TGA) and surface area determination.

Optical absorption

The optical absorption measurements were carried out in the region of visible and near infrared spectra with the double beam optical spectrometer (Model Cary 17). The optical absorption measurements were recorded as optical density (OD):

$$OD = \mathrm{Log}_{10}\left(\frac{I_i}{I_t}\right) \qquad (4.12)$$

where I_i is the intensity of incident light onto the sample and I_t the intensity of transmitted light out of the sample. The optical density measurements were mainly carried out for the evaporated WO_3 films at their initial, colored and bleached states. In the measurements, the WO_3 films on the transparent substrates were placed into the sample chamber and a transparent substrate in the reference chamber. The intensity of the light passing through the sample (WO_3 on substrate) was I_t and light intensity through the reference substrate was I_i. The optical densities of initial, colored and bleached WO_3 films were reported by the spectrometer.

Energy-dispersive X-ray spectroscopy

The energy dispersive X-ray spectrometer (EG&G ORTEC) was used to analyze the chemical compositions of cesium tungsten compounds. The samples were excited with an electron beam accelerated by a voltage of 15 kv in the vacuum. The characteristic X-ray energies emitted from the samples were analyzed by a Si(Li) diode.

Thermal gravimetic analysis (TGA) and surface area determinations

The thermal gravimetric analysis (TGA) is a powerful tool to analyze thermal decomposition of solid materials, such as H_2WO_4. The experiment was carried out on a Thermal Gravimetric Analyzer (Du Pont Instruments 951) under a helium gas flow of 50 ml/min. About 50 mg to 70 mg powder sample was used in each measurement. The sample was loaded in the TGA at room temperature and kept in helium gas flow for at least 20 minutes before running the TGA. In the experiments, temperature linearly increased from room temperature to 1000°C at a rate of 10° - 20°C/min.

To understand differences of lithium intercalation in different WO_3 powders, the surface areas of various WO_3 powders were measured. The measurements were carried out on a Quantaorb Sorption System and based on the theory that the physical adsorption of inert gas on a solid powder is proportional to its total surface area. About 0.5 g WO_3 powder was used in each experiment. The sample was loaded in a U type glass tube and heated at 200°C under a gas flow of the mixture of 70% helium and 30% nitrogen for 30 minutes to eliminate any moisture and gas absorbed on the powder

surface; then the U tube was immersed into liquid nitrogen while keeping helium and nitrogen gas flow went through the U tube. The quantity of nitrogen gas adsorbed by the sample inside the U tube at low temperature is compared to a known quantity of nitrogen and then the surface area of the sample was calculated.

Chapter 5

Hydrogen and lithium intercalation in WO_3 films

As discussed in the previous chapters that the EC process in an electrochemical cell is an active species intercalation together with a visible color change. The hydrogen and lithium intercalation into evaporated WO_3 films will be discussed in this chapter.

5.1 The crystal structure of WO_3 source material

To study the electrochromic mechanism in WO_3 films, a clear understanding of the basic crystal structure of source tungsten trioxides is of importance. Most WO_3 powders used in this thesis were purchased from the commercial sources, Aldrich Chemical Company, U.S.A (99% tungsten(VI) oxide, 1314-35-8). The crystal structure of the WO_3 powder was analyzed by X-ray powder diffraction. The results are shown in table 5.1 and figure 5.1. It was found that the original WO_3 powder has a monoclinic structure. The lattice parameters were calculated from 31 peaks of the X-ray diffraction patterns, they are a = 7.3100(8), b = 7.5402(7), c = 7.6948(5) and β = 90.90(1)°. This data are quite close to a published data (Loopstra 1969): a = 7.306, b = 7.540, c = 7.692Å and β = 90.881°.

Table 5.1 (a) Observed and calculated peak positions of X-ray diffraction patterns for the WO_3 powder.

h k l	d_o	d_c
0 0 2	23.104	23.120
0 2 0	23.581	23.598
2 0 0	24.353	24.355
1 2 0	26.600	26.603
1 1-2	28.602	28.614
1 1 2	28.903	28.931
0 2 2	33.258	33.273
2 0-2	33.573	33.555
2 0 2	34.144	34.102
1 2-2	35.415	35.398
1 2 2	35.653	35.660
2 2-2	41.453	41.433
2 2 2	41.901	41.891
3 2 0	44.265	44.263
3 1-2	45.372	45.369
3 1 2	45.957	46.007
0 0-4	47.267	47.254
0 4 0	48.300	48.278
4 0 0	49.907	49.907
1 1-4	50.331	50.338
1 1 4	50.723	50.733
0 2-4	53.460	53.478
0 4 2	54.159	54.182
2 4 0	54.805	54.793
4 2 0	55.912	55.916
2 2-4	59.204	59.239
2 2 4	C0.026	59.945
4 2-2	60.974	60.961
4 2 2	61.624	61.655
1 3 4	62.237	62.244
4 1-3	63.242	63.231

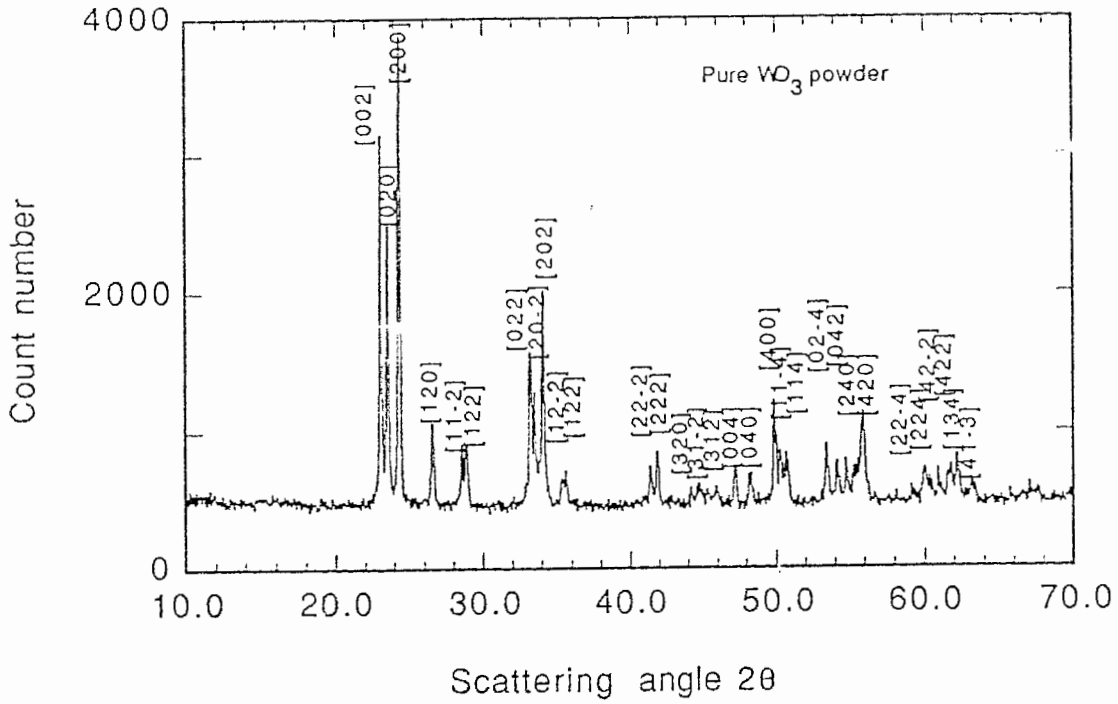

Fig. 5.1 The X-ray diffraction pattern of the WO_3 powder.

It will be seen later that it is more difficult to index the X-ray diffraction peaks from the evaporated WO_3 films, so the indices of these powder diffraction peaks are very useful as reference.

5.2 Characteristics of evaporated WO_3 films

WO_3 films were evaporated on three kinds of substrates: aluminum foil,

SnO_2 coated glass and the beryllium sheet. All freshly evaporated WO_3 films were amorphous as was identified by the X-ray diffraction patterns. The as-prepared films were of light blue color which might be due to the lack of oxygen in the films. To obtain a polycrystalline film, the as-prepared WO_3 film was annealed in air at the temperature from 350°C to 600°C. The WO_3 film turned transparent after the annealing. It was found that the adhesion of the WO_3 film to the substrate was very sensitive to the surface condition of the substrate and the evaporation rate. The substrate was carefully cleaned and the evaporation rate was controlled at a range from 50Å – 100Å/min, otherwise the WO_3 films could easily peel off the substrate no matter what the substrate temperature was. Figure 5.2 shows X-ray diffraction patterns of an annealed WO_3 film at 400°C on Al foil. It has a monoclinic structure. The calculated lattice constants for this annealed WO_3 film are shown in table 5.1 (b). As a comparison, the lattice constants for source WO_3 powder and the data in the literature (Loopstra 1969) are also listed. The agreement is quite good.

Table 5.1 (b) The lattice constants of evaporated WO_3 film and source WO_3 powder. Numbers in parentheses are standard deviations of the last significant digits.

	a (Å)	b (Å)	c (Å)	β (°)
Evaporated WO_3 film	7.319(5)	7.521(3)	7.707(4)	90.89(3)°
Source WO_3 powder	7.310(1)	7.540(2)	7.695(2)	90.90(2)°
(Loopstra 1969) data	7.306	7.540	7.692	90.881°

It was found that the calculated lattice constants for various WO_3 films

(on various substrate or annealed at various temperature) varied within a small range. Usually the X-ray diffraction peaks from the evaporated films were much broader (some peaks are broadened to about 1°) than that from the powders, and fewer peaks were observable in the film X-ray pattern Thus the lattice constants calculated from the film X-ray patterns may not be as accurate as that from the powder X-ray pattern.

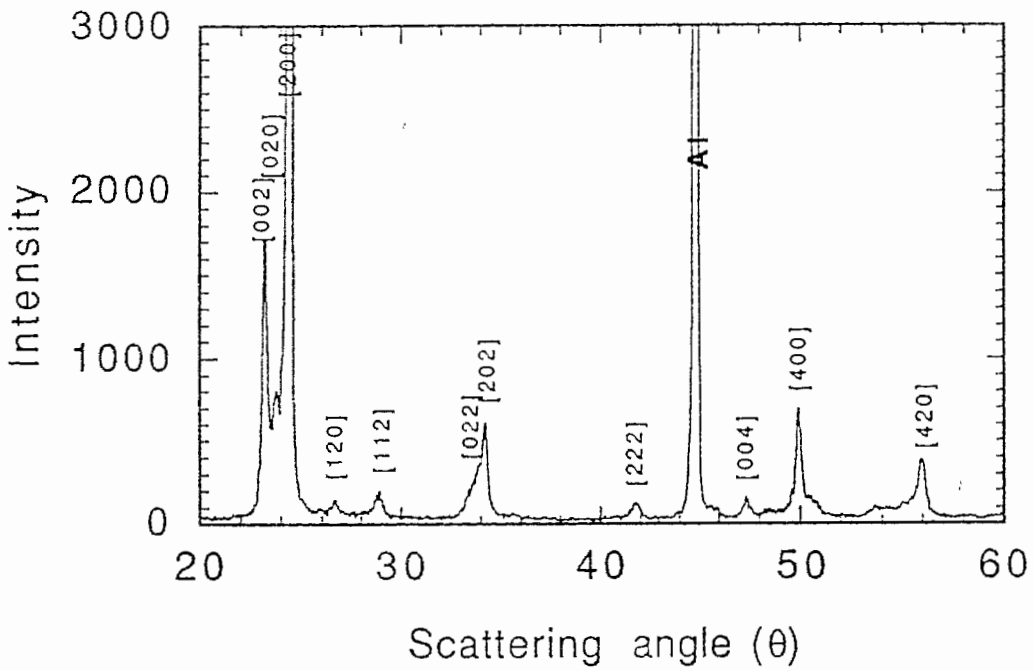

Fig. 5.2 The X-ray diffraction pattern of evaporated and annealed (400°C) WO_3 films on Al substrate.

5.3 Hydrogen intercalation in evaporated WO_3 films

The electrochemical cell used for hydrogen intercalation was shown in figure 4.1. 10% H_2SO_4 was used as the electrolyte and SCE was used as

reference electrode. The polycrystalline WO_3 films were obtained by annealing as prepared WO_3 films in air at 400°C for 2 to 3 hours. The thickness of the WO_3 films was about 600 - 2000 nm. We determined the crystal structure of the hydrogen tungsten bronze, hydrogen diffusion coefficients in WO_3, and the optical density change in the WO_3 film.

The cell's initial EMF was usually 400 mv (WO_3 vs. SCE), which could be varied to -200 mv by connecting the cell to an external power source in the coloration process. The coloration process will also be called the discharge or intercalation process in this thesis. By reversing the polarity of the external source, the WO_3 film could be bleached. The bleaching process will also be called the charge or deintercalation process. The cells were usually discharged to −200 mv for coloration and charged back to +500 mv for bleaching.

5.3.1 The crystal structure of the H_xWO_3 bronze

Figure 5.3 shows the X-ray diffraction patterns of initially prepared WO_3 film, colored H_xWO_3 film with hydrogen concentration of $x = 0.1$ and $x = 0.4$ and bleached WO_3 film. As can be seen, at low hydrogen concentration ($x = 0.1$, in figure 5.3), the crystal structure of H_xWO_3 is almost the same as the original WO_3 film (monoclinic). A crystal structure change was observed at higher hydrogen concentration ($x = 0.4$). In the bleached state, the X-ray diffraction pattern changes back to the initial state.

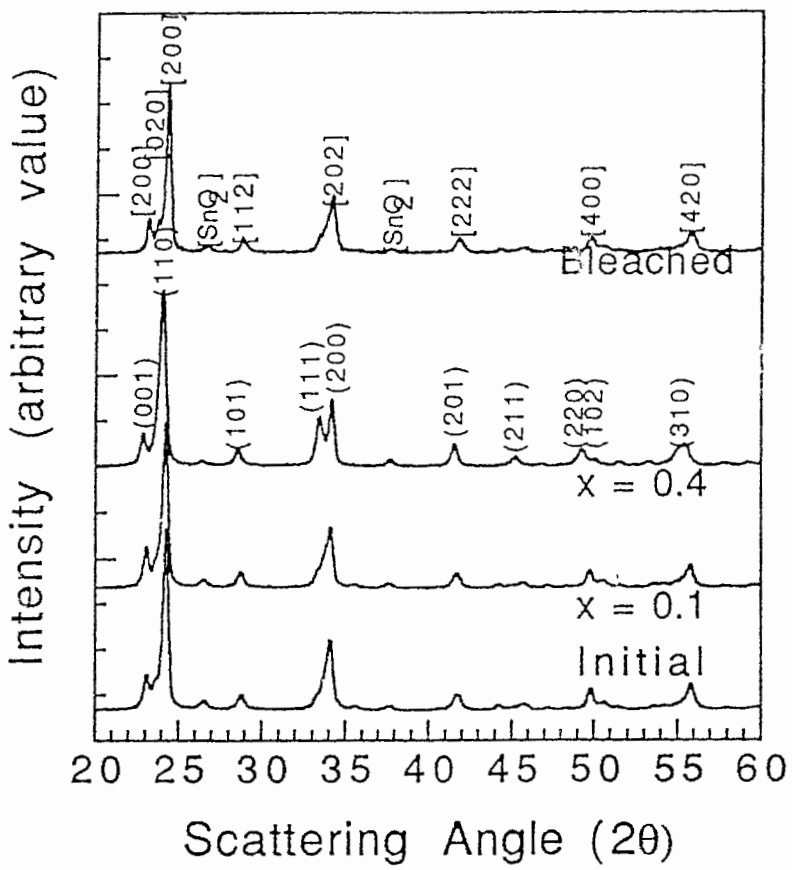

Fig. 5.3 The X-ray diffraction patterns of WO_3 films at initial, colored and the bleached states.

Using the Rietveld profile refinement program, the structure of the colored H_xWO_3 film (x = 0.4) was analyzed. The blue colored hydrogen tungsten bronze (x = 0.4) has a tetragonal symmetry. The space group is P4/nmm – D^7_{4h}. The systematic absences in the X-ray diffraction pattern

were hk0 with h + K = odd. From the profile refinement, the structural parameters of H_xWO_3 in an unit cell were found and the results are shown in table 5.2:

Table 5.2 The structural parameters of tetragonal H_xWO_3 in an unit cell.

Space group P4/nmm, a = 5.221(3)Å, b = 3.862(5)Å

Refinement R factor: 0.068

Origin at 2/m	x	y	z	B
2W in 2(c) 4mm	0.25,	0.25,	z,	1.0;
	0.75,	0.75,	-z,	1.0;
2O in 2(c) 4mm	0.25,	0.25,	0.50 + z,	1.2;
	0.75,	0.75,	-0.50 - z,	1.2;
4O in 4(e) 2mm	0.00,	0.00,	0.50,	1.2;
	0.50,	0.50,	0.50,	1.2;
	0.50,	0.00,	0.50,	1.2;
	0.00,	0.50,	0.50,	1.2.

where z is a refinable parameter and B is an isotropic temperature factor. The final refined z is 0.428. Due to weak interaction between hydrogen atoms and X-rays, we were not be able to determine the hydrogen positions in the unit cell. Table 5.3 lists the refined results for peak intensities and figure 5.4 depicts the profiles of raw (+++) and calculated (——) x-ray patterns for this tetragonal hydrogen tungsten bronze. The final refinement R factor (as expressed by equation 4.7) is 0.068 or 6.8%.

Table 5.3 A list of observed and calculated peak positions and intensities for the tetragonal hydrogen tungsten bronze.

h,k,l	$2\Theta_o$	$2\Theta_c$	I_{obs}	I_{cal}
0 0 1	22.10°	23.04°	21.8	23
1 1 0	24.14°	24.10°	100	100
1 0 1	28.70°	28.76°	10.3	10.4
1 1 1	33.60°	33.60°	31.0	31.1
2 0 0	34.19°	34.36°	23.9	17.6
2 0 1	41.69°	41.77°	11.0	8.9
2 1 1	45.34°	45.40°	7.7	7.8
2 2 0	49.43°	49.34°	15.9	17.4
1 0 2	50.24°	50.40°	5.7	6.3
1 1 2	53.49°	53.57°	4.5	4.5
3 1 0	55.59°	55.69°	15.3	14.6
0 3 1	58.04°	58.16°	1.6	1.5
0 2 2	59.35°	59.55°	2.0	1.8
3 1 1	60.94°	61.04°	13.7	11.6
2 1 2	62.26°	62.43°	7.3	7.4

From the refinement results, it can be seen that most calculated peak intensities agree with the experiment data. The main discrepancy between the calculated and the observed data (expressed by the R factor) comes from peak (200). In the calculation the tetragonal H_xWO_3 film was found having a preferred orientation in the (110) direction which was caused by preferred orientation in the (200) direction in the original monoclinic WO_3 film.

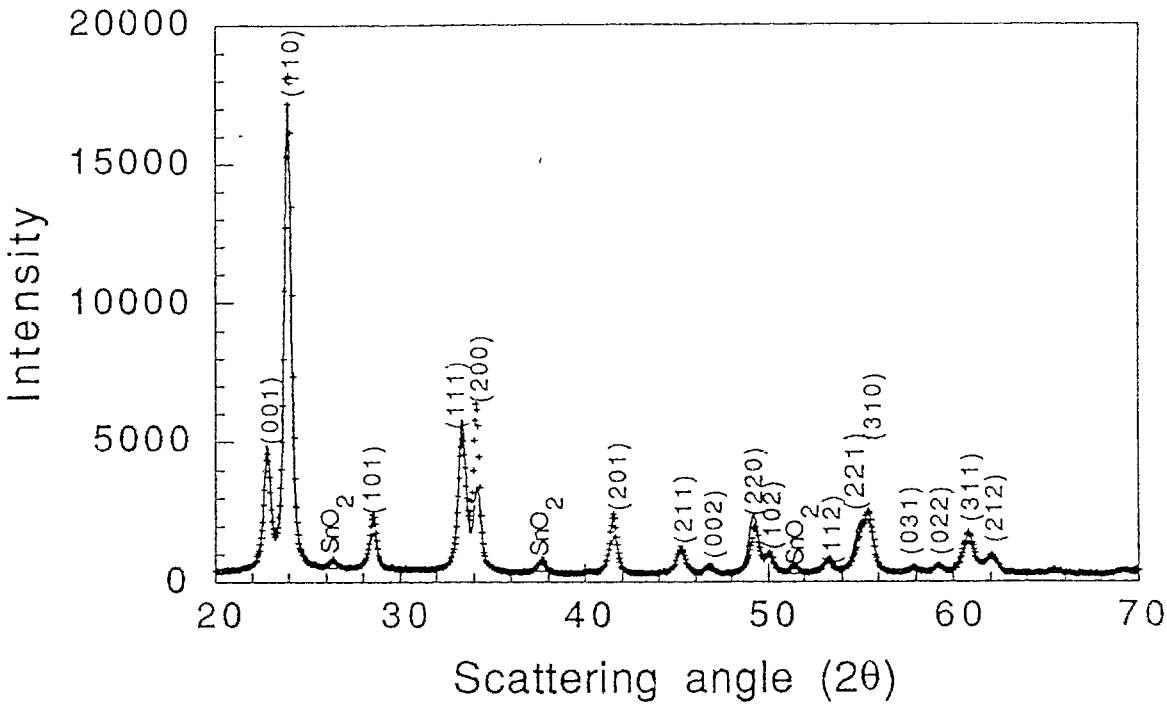

Fig. 5.4 Illustration of raw (+++) and calculated (——) X-ray scattering pattern for tetragonal H_xWO_3 film.

5.3.2 Optical properties of the H_xWO_3 film

The optical absorption spectra of initial and colored WO_3 films were measured in the visible and infrared spectral regions. The optical densities in colored WO_3 films were also measured as a function of charge density passing through the cell. Figure 5.5 shows the absorption spectra for WO_3 films at initial, colored and bleached states. The blue color was due to the hydrogen intercalation and the formation of hydrogen tungsten bronze. The hydrogen content in this colored sample was $x = 0.15$ in H_xWO_3. It can be seen that the main absorption region is in the near infrared. The maximum absorption peak appears at 900 nm (1.38 ev). The colored sample can be bleached by taking the hydrogen out of the WO_3 films.

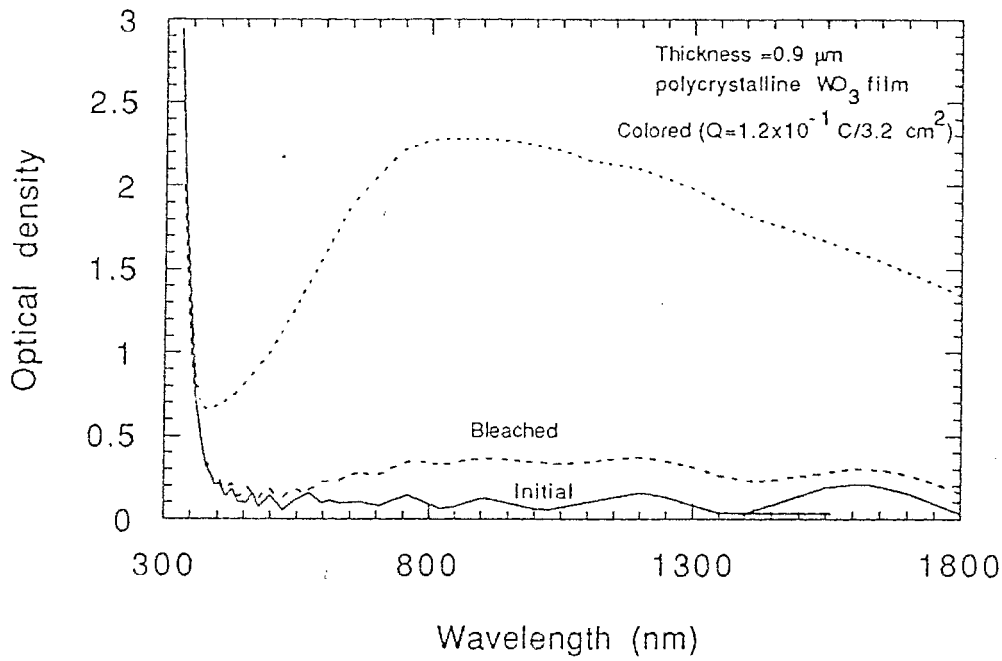

Fig. 5.5 The optical absorption of initial, colored and bleached H_xWO_3 films.

The relation between relative optical densities of the colored WO_3 film and the inserted charge densities was analyzed. The optical density was measured at a fixed wavelength of 623.8 nm (He-Ne laser). Figure 5.6 shows the results in which the optical density of original WO_3 films were set to be zero. A linear relation between the optical density and the charge density appears in the range from 0 to 30 mC/cm^2. The WO_3 film used in this experiment had the thickness of 0.6 μm and density of about $6g/cm^3$. The molecular weight of WO_3 is 231.85g/mol. Thus the hydrogen content in the linear region varied from x = 0 to 0.2 in H_xWO_3. As seen in figure

5.6, at a charge density of 30 mC/cm^2 (x = 0.2) the optical density in the WO_3 film is approximately 1.0, large enough for display systems. From the crystal structure analysis, it has been known that a phase change in the H_xWO_3 film appears at about x = 0.4 which means that the H_xWO_3 films may work as an EC layer in a single phase region in a display systems.

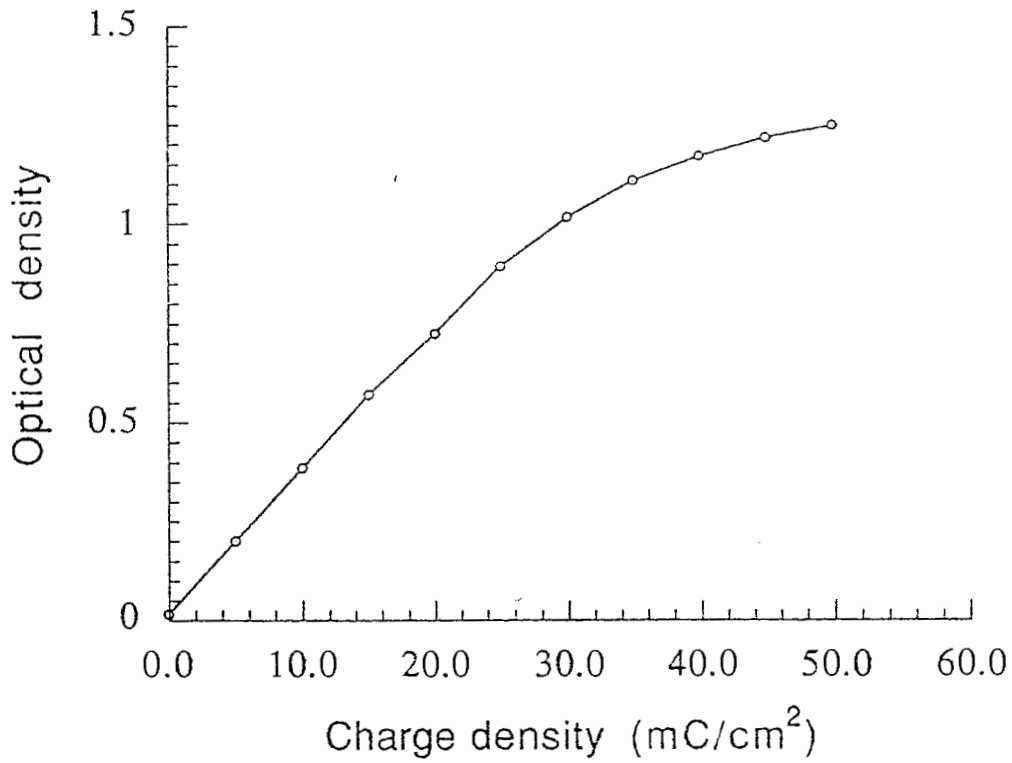

Fig. 5.6 The relation of optical density in H_xWO_3 films to the injected charge density.

5.3.3 Hydrogen diffusion into the WO_3 films

As was discussed in Chapter 4, the hydrogen atoms intercalate into the WO_3 host if the electrical potential of the WO_3 host film is lowered by applying an external electrical perturbation. The hydrogen ions from the electrolyte enter into the surface of the WO_3 film and meet the electrons injected from the other side of the film. The neutralized hydrogen atoms will accumulate at the surface of the WO_3 film and establish a hydrogen concentration gradient due to which the hydrogen atoms will diffuse into the bulk of the film. The diffusion speed of the hydrogen atoms in the WO_3 film is an important parameter for the response time of an EC cell. We determine the diffusion coefficient of hydrogen in the WO_3 films using the current step method (Weppner and Huggins 1977). From equation (3.30)

$$\frac{\delta E_t}{\delta \sqrt{t}} = \frac{2IV_m}{FS\sqrt{(D\pi)}}\left[\frac{\delta E_x}{\delta x}\right] \qquad \text{for } t \ll L^2/D \qquad (5.1)$$

This equation may be transformed to a simpler algebraic form if E vs. $\sqrt{t}$ shows a linear relation over the entire time period of the current step. Consider a current impulse at $0 < t < \tau$, the $\delta\sqrt{t} = (\sqrt{\tau} - \sqrt{t_0}) = (\sqrt{\tau})$ and the expression on the left side of equation 5.2 become $\delta E_t/\sqrt{\tau}$. After the current pulse, an amount of δx of intercalated hydrogen is redistributed inside the film and this additional hydrogen will cause an EMF change δE_x. Using

$$\delta x = \frac{I\tau M_c}{Z_A m_c F} \qquad (5.2)$$

where I is the constant current, M_c the molecular weight of cathode

material (here WO_3), m_c the mass of cathode in the cell, Z_A the valence number of intercalated active species (for hydrogen, Z = 1), and F Faraday's constant. With the linear condition and equation (5.2) the diffusion coefficient D can then be expressed as:

$$D = \frac{4}{\pi\tau}\left[\frac{m_c V_m}{M_c S}\right]^2\left[\frac{\delta E_x}{\delta E_t}\right]^2 \qquad t \ll L^2/D \qquad (5.3)$$

The hydrogen diffusion coefficients in WO_3 films were obtained directly from the determination of δE_t and δE_x. Figure 5.7 shows the experimental data of E_t vs. $\sqrt{t}$ for H_xWO_3 cathode at x = 0.16 and x = 0.23. Linear relationships were found between the E_t and $\sqrt{t}$, and thus the chemical diffusion coefficient of hydrogen in the WO_3 films can be determined with equation (5.3).

The calculated hydrogen diffusion coefficients in H_xWO_3 are shown in table 5.4.

Table 5.4 The diffusion coefficients of hydrogen in H_xWO_3 films

x	D_H (10^{-10} cm^2 s^{-1})
0.00	6.4
0.07	1.0
0.16	2.1
0.23	2.5

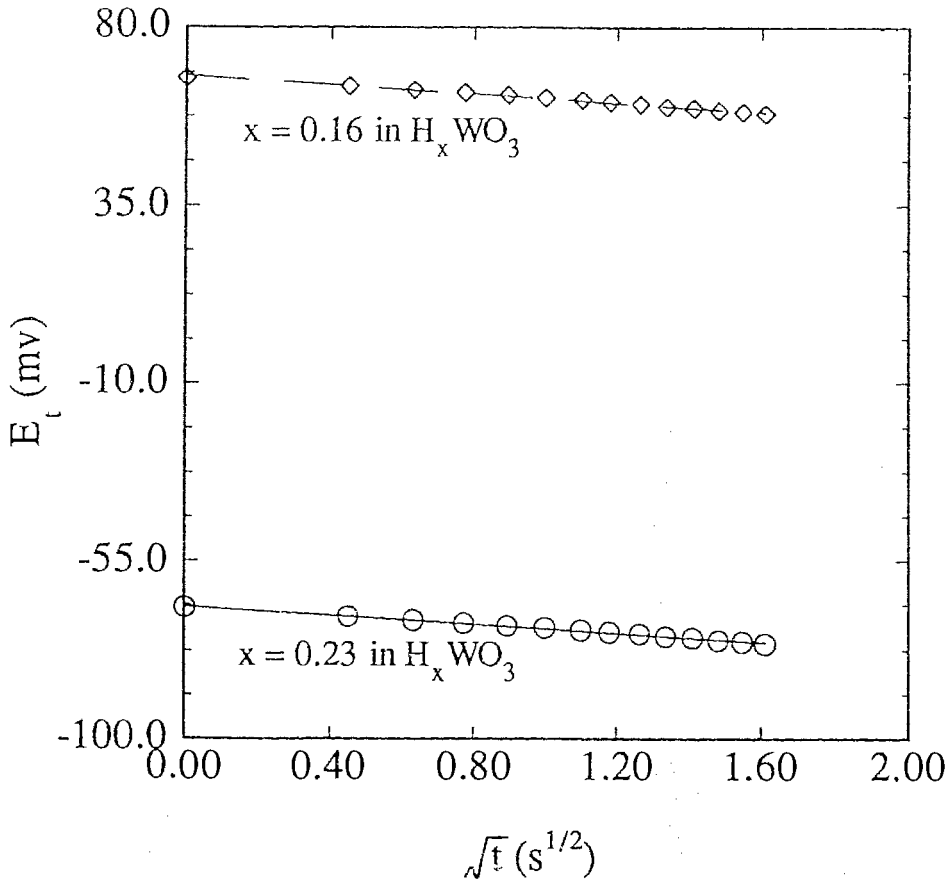

Fig. 5.7 The plot of E_t vs. $\sqrt{t}$ during the current pulse.

5.3.4 Discussion of hydrogen tungsten bronze

Since Deb (1969) first reported the electrochromic phenomena in the WO_3 films, hundreds of papers have been published in order to understand the EC mechanism. As was discussed in Chapter 1 and 2, the tungsten bronze formation (or ion - electron double injection) model has been widely accepted, however, most previous work was based on amorphous WO_3 films. There was a lack of studies for the crystal structure of electrochemically formed H_xWO_3. In this chapter it has been shown that the hydrogen tungsten

bronze can be electrochemically formed and has the tetragonal symmetry at $x = 0.4$ in H_xWO_3. It was also shown that tetragonal H_xWO_3 would change back to the initial monoclinic WO_3 after the sample was bleached.

There were studies in the literature of the crystal structures of H_xWO_3 powders and single crystals formed with chemical reactions or other methods. At least four phases were reported in the range of $x = 0.1$ to $x = 0.5$ (Glemser and Naumann 1951; Dickens and Hurditch 1967). They were $H_{0.1}WO_3$ (tetragonal), $H_{0.23}WO_3$ (tetragonal), $H_{0.33}WO_3$ (orthorhombic) and $H_{0.5}WO_3$ (cubic). In this thesis, one phase change was observed for the H_xWO_3 film. The crystal structure data of the H_xWO_3 films determined here is similar to the data obtained by Dickens (1967) for $H_{0.23}WO_3$. As will be seen later in the studies for Li_xWO_3 structure, the phase change in WO_3 host is not only dependent on the x in Li_xWO_3, but also dependent on the preparation conditions of the WO_3 host. The same may be true for H_xWO_3, in that the x value in tetragonal H_xWO_3 film is different from that in the H_xWO_3 powder. It should be mentioned that the crystal structure of H_xWO_3 film was measured when the H_xWO_3 film was exposed to the air. It was not clear how fast the hydrogen inside the H_xWO_3 films would react to the oxygen in the air. The hydrogen content in tetragonal H_xWO_3 might be of a value lower than 0.4 after the colored film was exposed to the air.

It is worth to point out that the measurements for hydrogen diffusion coefficient was based on several assumptions: the real surface area S was known; the diffusion was semi-infinity; δE_t vs. $\sqrt{t}$ was linear; and $t \ll L^2/D$. Some of these assumptions were hard to verify, thus the diffusion coefficients measured in this thesis have only relative meaning. We will

compare the diffusion coefficients for different atoms in the same host or we will compare the diffusion coefficients for one type of atoms in different hosts.

5.4 Lithium intercalation in evaporated WO_3 films

Studies for the intercalation of lithium into WO_3 films are the another important part in this chapter. It will be shown that the coloration in WO_3 films in a lithium based EC cell is based on the formation of lithium tungsten bronzes. The EC cell used for Li intercalation has been shown previously in figure. 4.2. The initial EMF (WO_3 vs. Li) of the cell varied from 3.00V to 3.15V. The WO_3 film turned blue color when the lithium intercalated into the film and turned bleached when the lithium deintercalated.

5.4.1 Electrochemical analysis for Li_xWO_3 films

As is discussed in chapter 3, the chemical potential of lithium in the WO_3 cathode is related to the cell's EMF by equation (3.8):

$$\begin{aligned} EMF &= -(1/ze)(\mu_{cathode} - \mu_{anode}) \\ &= -(1/ze)(\mu_{cathode} - \text{constant}) \end{aligned}$$

thus the cell's EMF gives a direct measurement of the chemical potential for the lithium in the WO_3 film. Figure 5.8 shows EMF data for two cells. In one cell (400 in figure 5.8), the WO_3 film (cathode) was annealed at

400°C in air for 2 hours and in the other cell (600 in figure 5.8), the WO_3 film was annealed at 600°C. Two plateaus are observed on the EMF-x curve when the cells discharge from 3.2V to 2.0V. The first one appears when the EMF goes down to 2.75V and the second one appears when the EMF was reduced to 2.55V. This means that the WO_3 cathode in the cell may undergo two phase changes during the Li intercalation. The plateaus in the charge process are not so obvious as those in the discharge but they do exist as can be identified later in the derivative plots.

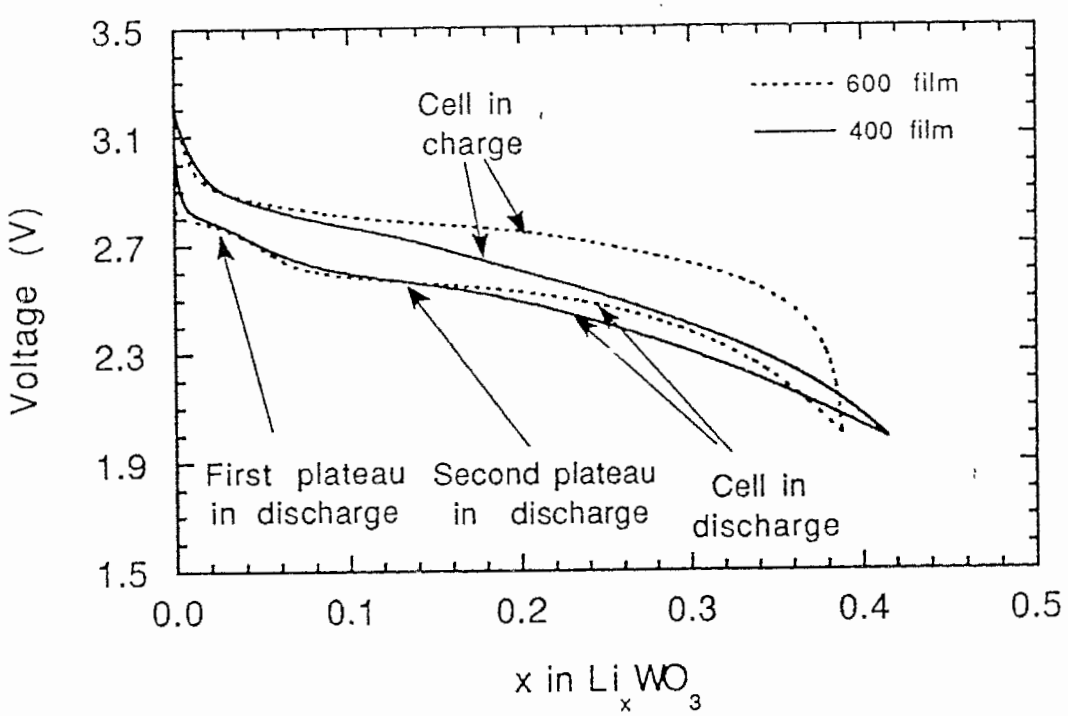

Fig. 5.8 The discharge/charge curves for the $Li/LiClO_4$ in $PC/EC/WO_3$ in battery cells, one cell (——) with the WO_3 film annealed at 400°C and the other (---) with the WO_3 film annealed at 600°C.

The phase change can be more clearly seen from the derivative plot of figure 5.8 (see figure 5.9). The peaks in the derivative curves correspond to the plateaus in the EMF–x curve as well as the phase changes in the cathode. As indicated in figure 5.9 (a), two phase changes are observed in WO_3 films in discharge. It will be seen in the next section that the first phase change in discharge corresponds to a phase change of monoclinic WO_3 to tetragonal Li_xWO_3 and the second phase change in discharge corresponds to that of tetragonal Li_xWO_3 to cubic Li_xWO_3.

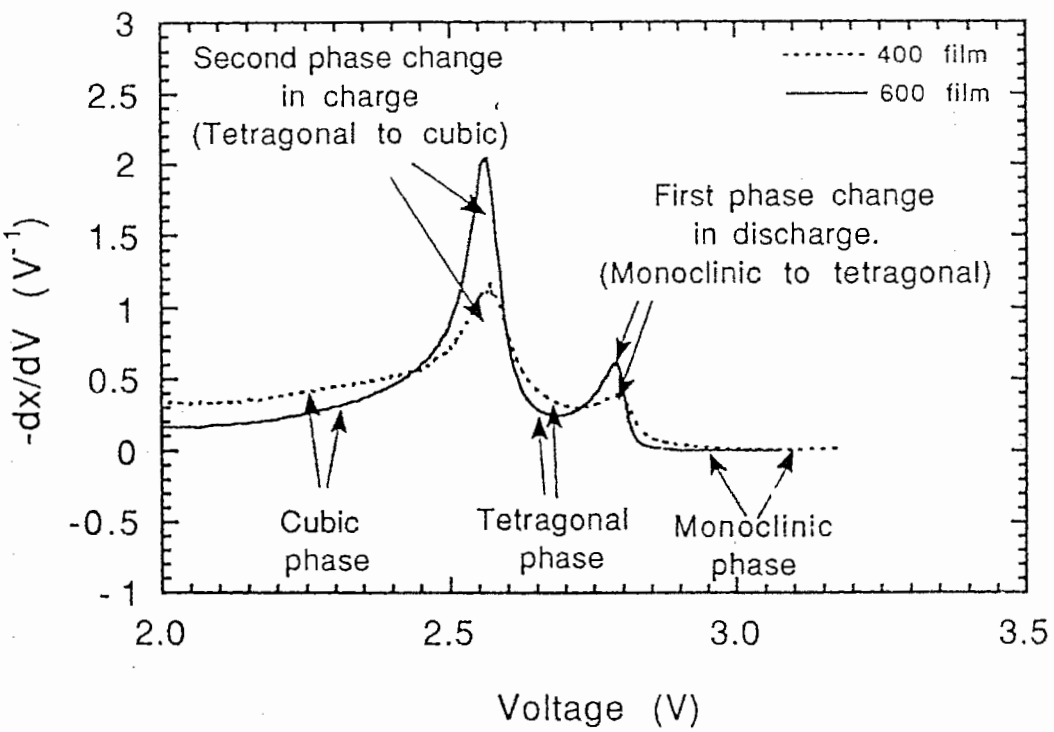

Fig. 5.9 (a) The derivative plots of discharge EMF curves in figure 5.8

The phase changes also appear in the charge. As indicated in figure 5.9 (b), two peaks occur in the charge process: one at 2.78V should correspond to the phase change of the cubic Li_xWO_3 to tetragonal Li_xWO_3 and another at 2.85V should correspond to tetragonal Li_xWO_3 to monoclinic WO_3 phase changes. This means that the Li_xWO_3 film shows a reversible phase transition during the discharge/charge in the voltage range of 2.0V to 3.2V. The quantities of lithium ions incoming to and outgoing from the WO_3 film are found to be equal. In the next section, the crystal structure of tetragonal and cubic Li_xWO_3 will be analyzed.

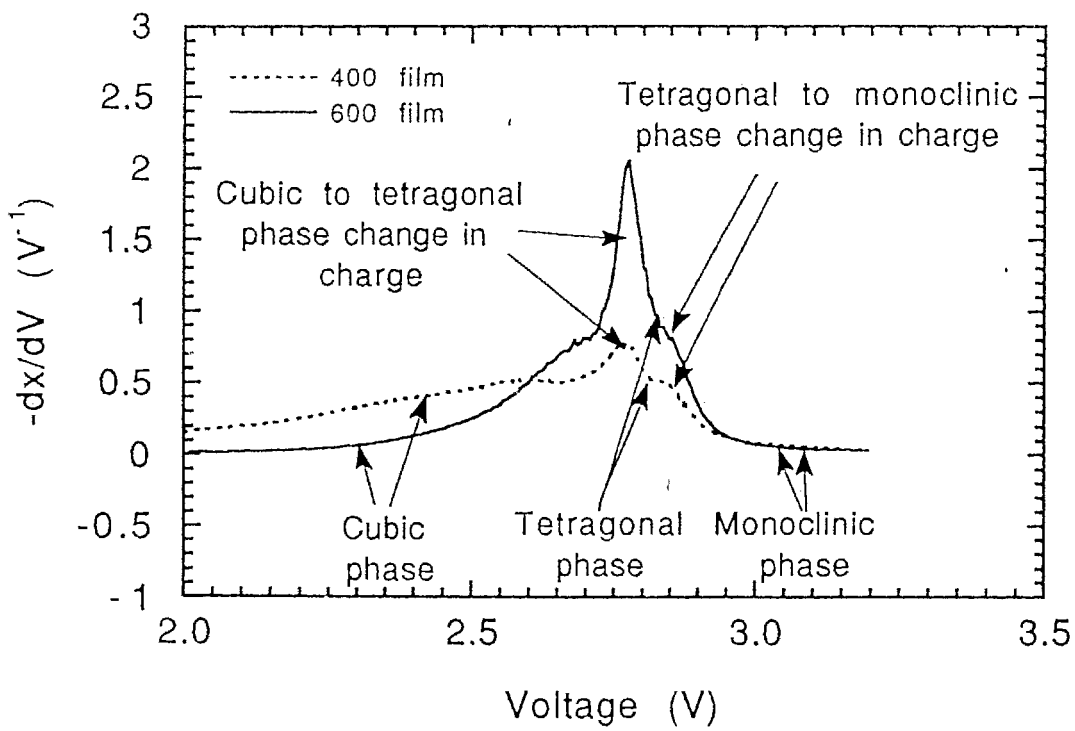

Fig. 5.9 (b) The derivative plots of charge curves in the figure 5.8

5.4.2 The crystal structures of electrochemically formed Li_xWO_3 films

5.4.2.1 Tetragonal and cubic phase in Li_xWO_3 films in the discharge process from 3.2V to 2.0V

The structure data were obtained from X-ray diffraction experiment using X-ray cells with beryllium windows (see Fig. 4.3). The WO_3 film was deposited on a piece of beryllium sheet (thickness of 0.25 mm) and then annealed at 400°C for 2 hours in air to obtain the polycrystalline film. The Li_xWO_3 in the X-ray cell was expected to undergo the same phase changes as that in a battery cell. Figure 5.10 shows the EMF–x curve of the X-ray cell in the discharge/charge processes. It is found that the EMF curves from the X-ray cell show the same phase changes as from the battery cell. The derivative curves for the X-ray cell shown in figure 5.11 lead to the same conclusion.

The X-ray diffraction data from the discharge process were analyzed. From the above EMF–x curves, it is known that the crystal structure of the Li_xWO_3 film depends on the lithium concentration x or the EMF of the cell. To measure the structure changes in the Li_xWO_3 film, a number of constant voltages were applied to the X-ray cell in discharge. The X-ray cell was kept at each selected voltage for at least 20 hours before the X-ray experiment was performed. Seven different voltages were selected from 3.2V to 2.0V. From the X-ray data, two new crystal structures of Li_xWO_3 were determined.

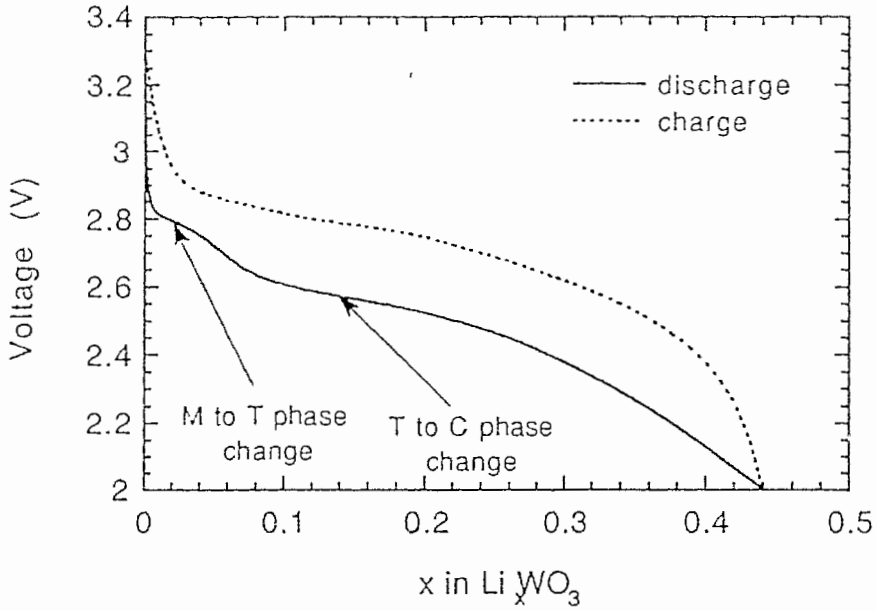

Fig. 5.10 The discharge/charge curves of Li_xWO_3 film in the x-ray cell.

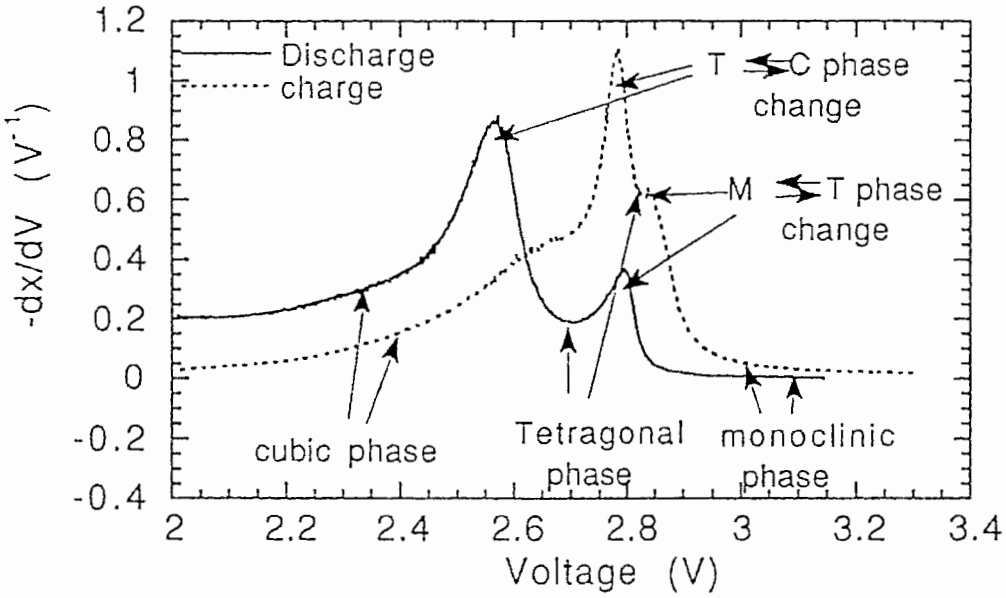

Fig. 5.11 The derivative plots of EMF-x curves of Li_xWO_3 films in the x-ray cell.

Tetragonal phase

It was found that the original monoclinic structure in WO_3 films changes to a tetragonal phase at V = 2.7V and x = 0.05 in Li_xWO_3. Figure 5.12 shows the X-ray diffraction patterns for the original WO_3 (a) and lithium intercalated Li_xWO_3 (b) film at 2.7V. The initial WO_3 film (at initial cell's voltage of 3.15V) has the monoclinic structure (or pseudo-orthorhombic) as can be identified by the presence of (002), (020) and (002) peaks. It will be seen later that these three peaks are reduced to two peaks when Li_xWO_3 becomes tetragonal (a = b) and further reduced to one peak when Li_xWO_3 becomes cubic (a = b = c). At 2.7V, the X-ray diffraction pattern is changed. To analyze the crystal structure of Li_xWO_3 in the X-ray cell, the recorded intensity I_r should be corrected to I_o by (see equation 4.9)

$$I_o = I_r \exp(2\mu l/\sin\theta) \qquad (5.4)$$

The Reitveld profile refinement method was used to analyze the structure. In calculation those angle regions where the main beryllium reflection peaks appear were excluded. The refined crystal structure parameters are listed in table 5.5. It was found that the tetragonal Li_xWO_3 has the same crystal structure as that of tetragonal H_xWO_3. The difference is that the x (0.05 in tetragonal Li_xWO_3 is much less than x (0.4) in tetragonal H_xWO_3. Due to the weak reaction between the Li atom and the X-rays, we were not able to determine the lithium positions in the unit cell.

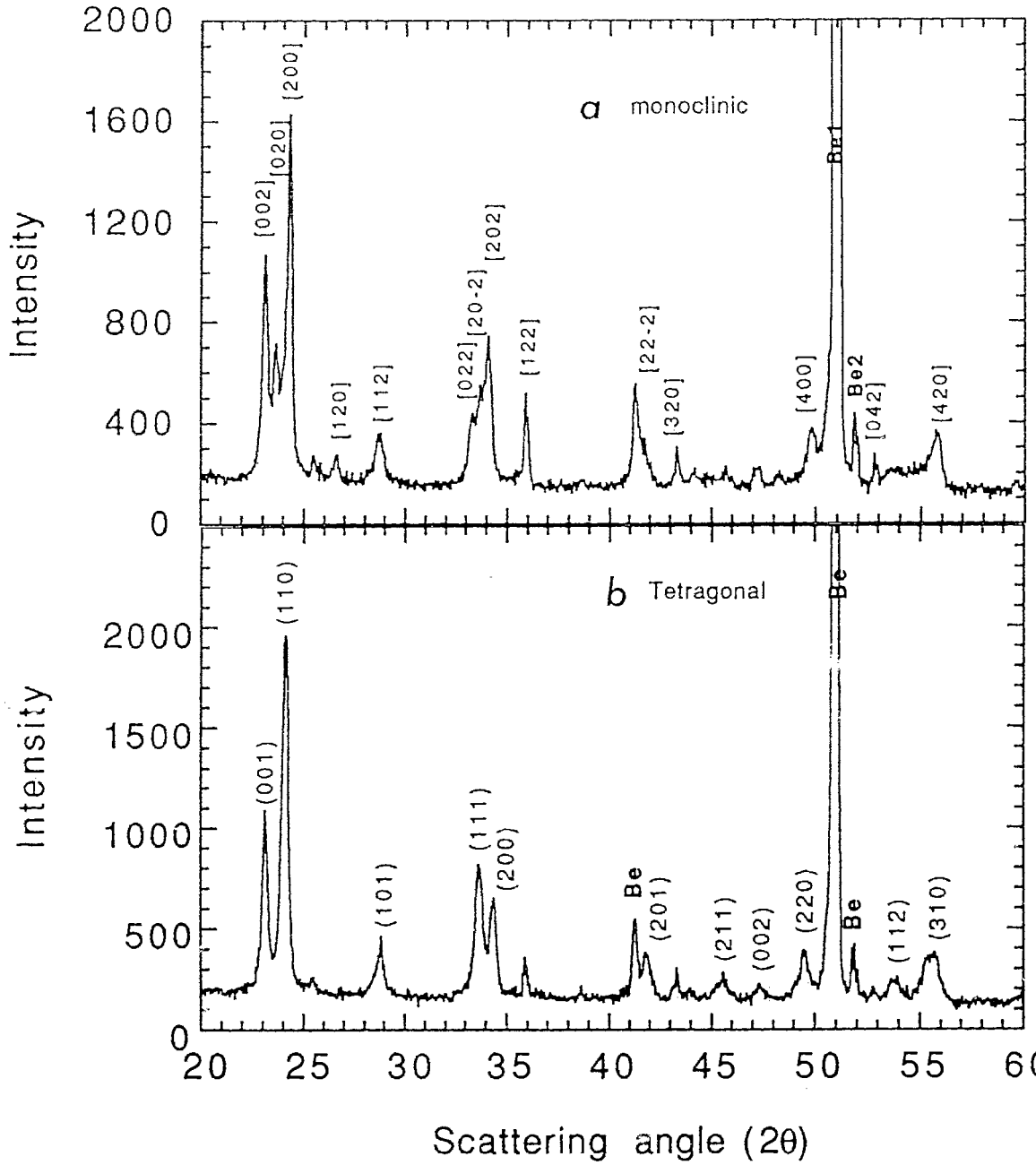

Fig. 5.12 The X-ray diffraction patterns of monoclinic WO_3 film (a) and tetragonal Li_xWO_3 film in the X-ray cell at 2.7V (b).

Table 5.5 The structural parameters of tetragonal Li_xWO_3 film in unit cell

Cell dimensions: a = 5.205(3)Å, c = 3.836(2)Å.

Final R factor: R = 0.023

Space group: P4/nmm

Origin at 2/m	x	y	z	B
2W in 2(c) 4mm	0.25,	0.25,	0.434,	3.6
	0.75,	0.75,	0.566,	3.6
2O in 2(c) 4mm	0.25,	0.25,	0.926,	1.0
	0.75,	0.75,	0.074,	1.0
4O in 4(e) 2mm	0.00,	0.00,	0.00,	1.0
	0.50,	0.50,	0.50,	1.0
	0.50,	0.00,	0.50,	1.0
	0.00,	0.50,	0.50,	1.0

Table 5.6 shows the raw and calculated peak positions and intensities of the X-ray patterns for the tetragonal Li_xWO_3 film. Figure 5.13 shows the results of profile refinement.

Table 5.6 Raw and Calculated peak positions and intensities of the X-ray patterns for the tetragonal Li_xWO_3 film.

h k l	$2\theta_o$	$2\theta_c$	I_o	I_c
0 0 1	23.19°	23.19°	44.5	43.6
1 1 0	24.18°	24.18°	100.0	98.1
1 0 1	28.89°	28.91°	14.2	14.5
1 1 1	33.73°	33.75°	37.1	38.6
2 0 0	34.43°	34.46°	22.1	21.4
2 0 1	41.84°	41.95°	11.4	10.2
2 1 1	45.64°	45.59°	6.6	6.9
0 0 2	47.38°	47.40°	3.7	3.9
2 2 0	49.43°	49.43°	13.5	13.8
3 1 0	55.85°	55.85°	12.0	11.8
3 1 1	61.23°	61.28°	9.4	8.7

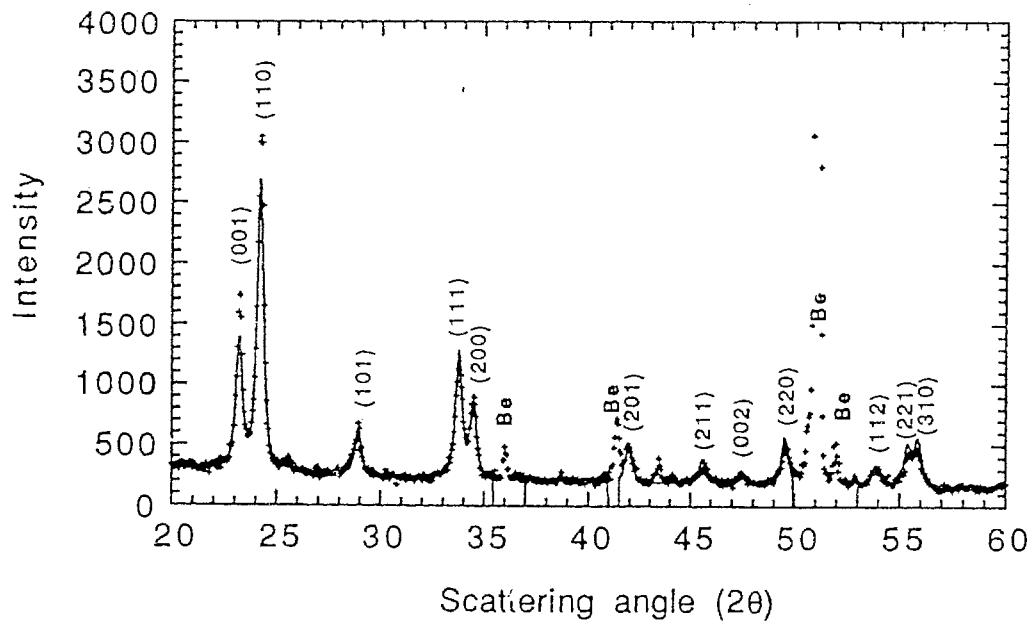

Fig. 5.13 The raw X-ray data (+++) and calculated profile (——) of tetragonal Li_xWO_3 film at 2.7V.

cubic phase

With the same method, the structures of the Li_xWO_3 film in the X-ray cell at the voltage range from 2.4V to 2.0V in discharge were determined. A cubic phase was observed in the voltage range from 2.4 to 2.0V in discharge. The lithium concentration is about x = 0.28 to x = 0.5 in the cubic Li_xWO_3 phase. The structure refinement reveals that the cubic Li_xWO_3 belongs to the Pm3m space group. There are four atoms in a unit cell: the tungsten atom is at 0,0,0; three oxygen atoms are at 0.5,0,0; 0,0.5,0; and 0,0,0.5, respectively. For an X-ray pattern obtained at 2.0V, table 5.7 lists the final refined results of raw and calculated peak positions and intensities for the cubic lithium tungsten bronze. The refine factor R obtained is 0.036.

Table 5.7 Raw and calculated peak positions and intensities for the X-ray pattern of cubic Li_xWO_3 film at 2.0V.

a = 3.7256(4)Å

h k l	$2\theta_o$	$2\theta_c$	I_o	I_c
1 0 0	23.89°	23.90°	100.0	100.6
1 1 0	34.04°	34.06°	48.0	47.9
1 1 1	41.95°	41.98°	11.5	9.8
2 0 0	48.88°	48.89°	14.4	15.3
2 1 0	55.08°	55.10°	26.2	27.5
2 1 1	60.84°	60.88°	13.8	12.7

Figure 5.14 shows the raw (+++) and the calculated (——\ cubic Li_xWO_3 x-ray pattern profile. The angle regions where the main beryllium reflection peaks appear were excluded from the calculation.

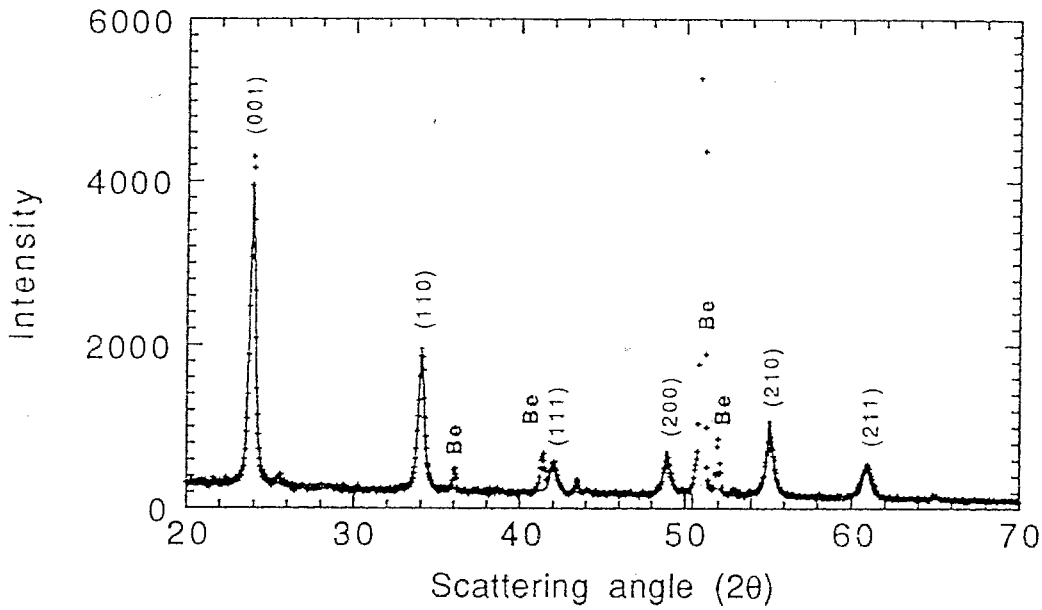

Fig. 5.14 The X-ray diffraction patterns of Li_xWO_3 film at 2.0V in the X-ray cell and the calculated profile.

Sienko and Troung (1961) reported the crystal structure of thermodynamically formed $Li_{0.394}WO_3$, $Li_{0.374}WO_3$ and $Li_{0.365}WO_3$ powders and claimed that the lithium tungsten bronzes have the cubic symmetry (lattice constants a = 3.715Å to 3.723Å). Our film data are quite close to their results except that the cubic phase of Li_xWO_3 film exists in a relatively wide x range. However the tetragonal Li_xWO_3 phase is first reported in this thesis. From the above data analysis, the phase regions in Li_xWO_3 films at the discharge process can be approximately determined. The results are summarized in table 5.8:

Table 5.8 Summary of phase variations in the Li_xWO_3 film

Phases	Monoclinic Li_xWO_3	Tetragonal Li_xWO_3	Cubic Li_xWO_3
Voltage range* (v.s Li^+/Li)	3.15V–2.85V	2.75V–2.65V	2.4V–2.0V**
x range	0.0 to 0.01	0.03 to 0.08	0.28 to 0.5**

* The voltage ranges of 2.85V–2.75V and 2.65V–2.40V are the phase transition regions in which more than one phase may exist.

** The voltage range for the cubic phase can be lower than 2.0V and the the x in cubic Li_xWO_3 can be higher than 0.5 as will become clear later.

5.4.2.2 The crystal structure of Li_xWO_3 film during the charge process

Fig. 5.11 (derivative plot of EMF data) show that the Li_xWO_3 cathode undergoes two phase transition to turn back to the monoclinic structure in the charge process. The -dV/dx peak appearing in the voltage range from 2.70V to 2.80V corresponds to the cubic -> tetragonal phase transition and the -dV/dx peak in the voltage range from 2.83V to 2.88V corresponds to the tetragonal -> monoclinic phase transition. Since the tetragonal phase exists in a very narrow voltage region: 2.81V – 2.82V in the charge process, pure tetragonal phase in the charge was not clearly observed in this experiment. This problem is discussed in the next chapter. The monoclinic structure in the Li_xWO_3 was observed after the cell was charged back to 3.4V. Figure 5.15 shows the X-ray diffraction patterns of the WO_3

film in the X-ray cell at 3.4V (after charge). The WO_3 film shows the monoclinic structure after the charge (bleach) process.

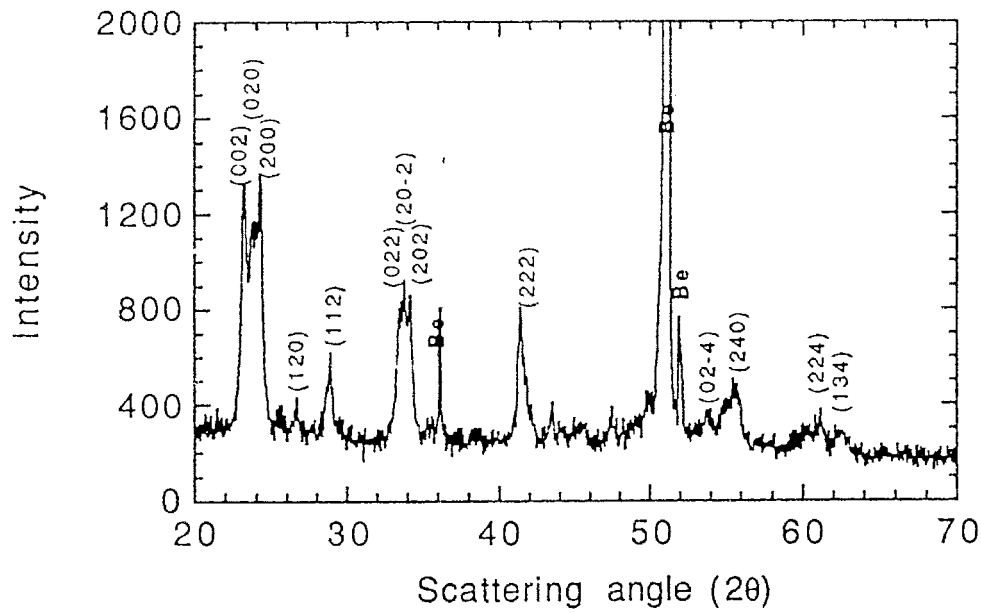

Fig. 5.15 The X-ray diffraction pattern of the WO_3 film in the X-ray cell after charged back to 3.4V.

5.4.2.3 The phase change of Li_xWO_3 below 2.0V

From all data discussed above it can be concluded that the WO_3 films undergo a reversible discharge/charge (coloration/bleaching) process in the electrical potential range of 3.4V and 2.0V. It will be of interest to ask what is the lowest voltage limit above which the discharge/charge process is reversible. The discharge/charge curves shown in figure 5.16 (a) and (b) can answer this question. The figure 5.16 (a) shows that the discharge/charge process can stay reversible as long as the lower voltage was above 1.0V (at x ~ 1.0) because the same shape of discharge curves appeared in the subsequent discharge/charge cycles.

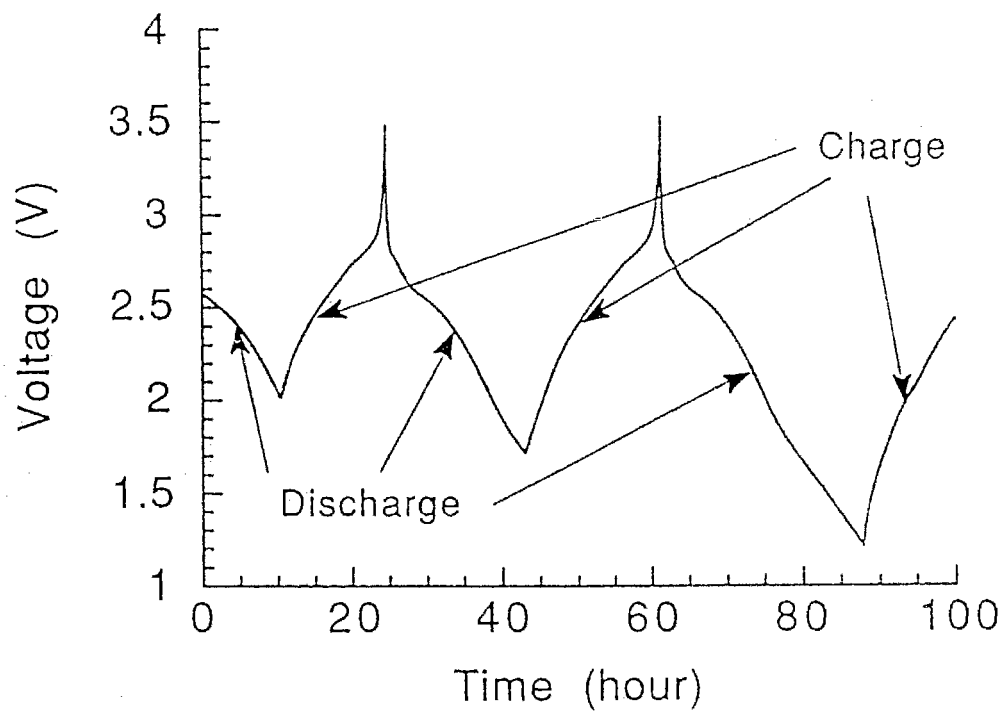

Fig. 5.16 (a) The discharge/charge process of Li_xWO_3 film in the battery cell between 3.2V and 1.2V. The cell was charging and discharging at 25 hour rate.

Figure 5.16 (b) shows that the discharge/charge process became irreversible when the cell discharged to a voltage lower than 1.0V. A very long plateau occurred at about 1.0V in the discharge process. After the long plateau a totally new curve appeared and never turned back to the initial state again. The irreversible process can also be identified from the fact that the total quantity of inserted lithium in the first discharge process is much greater than that of extracted lithium in the charge process.

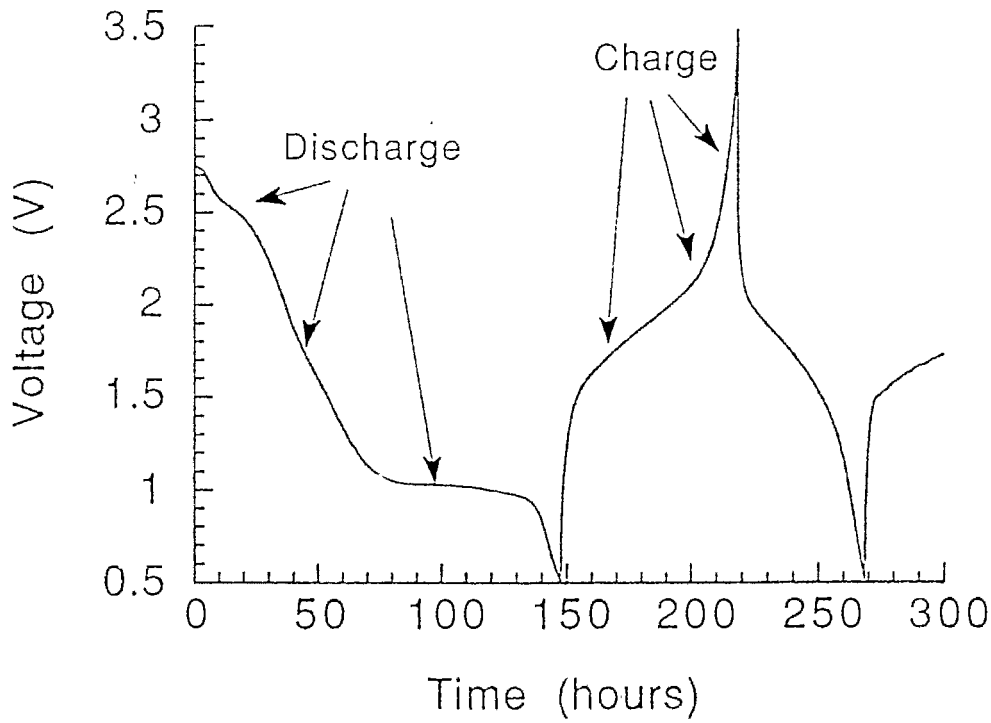

Fig. 5.16 (b) The discharge/charge process of a Li/$LiClO_4$ PC/WO_3 cell between 3.2V and 0.5V.

Figure 5.17 shows the x-ray diffraction patterns of the Li_xWO_3 at 1.2V, 0.8V, 0.5V and back to 3.2V. The Li_xWO_3 film shows the cubic structure at 1.2V ($x \sim 0.9$). Some unknown new phase(s) appeared at 0.8V. The cubic

phase completely disappeared at 0.5V. The structure of the Li_xWO_3 film at 0.5V was close to amorphous because no noticeable diffraction peak were observed in the X-ray diffraction pattern. It is noted that the crystal structure of the Li_xWO_3 film after the cell charges back from 0.5V to 3.2V is a totally new structure. On the other hand, the Li_xWO_3 film could not be bleached if the cell's voltage went below 1.0V, since the lithium content in the Li_xWO_3 film could not be zero again.

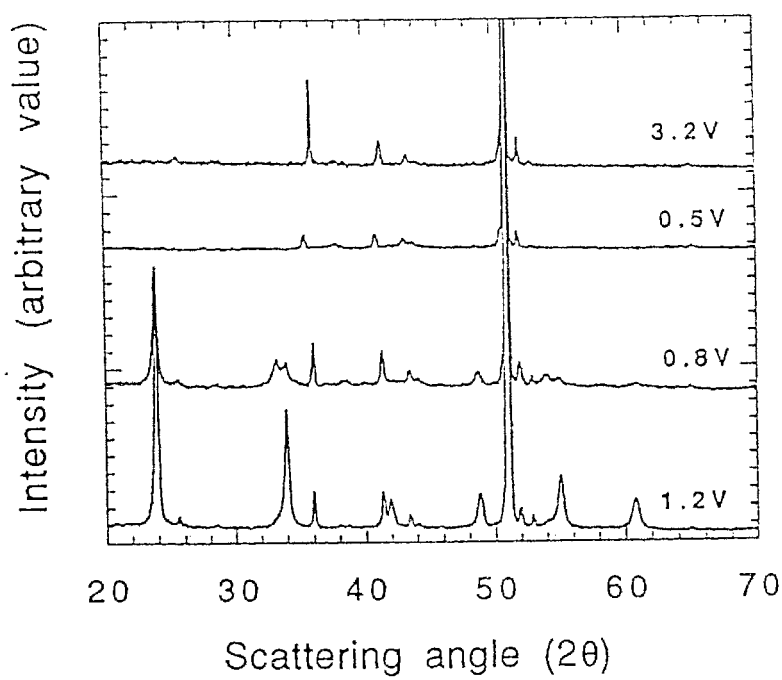

Fig. 5.17 The X-ray diffraction patterns of Li_xWO_3 film at 1.2V, 0.8V, 0.5V and charged back to 3.2V in the X-ray cell.

5.4.3 Optical and electrochemical properties of Li_xWO_3 films

The intercalation of lithium into WO_3 films causes not only the crystal structure change but also the electrical and the optical property changes in WO_3 films. The originally transparent WO_3 films turned blue after the intercalation of the lithium as was observed after the hydrogen intercalation. Figure 5.18 shows the optical absorption spectra of WO_3 films (0.9 μm) at original, colored (lithium intercalated) and the bleached state.

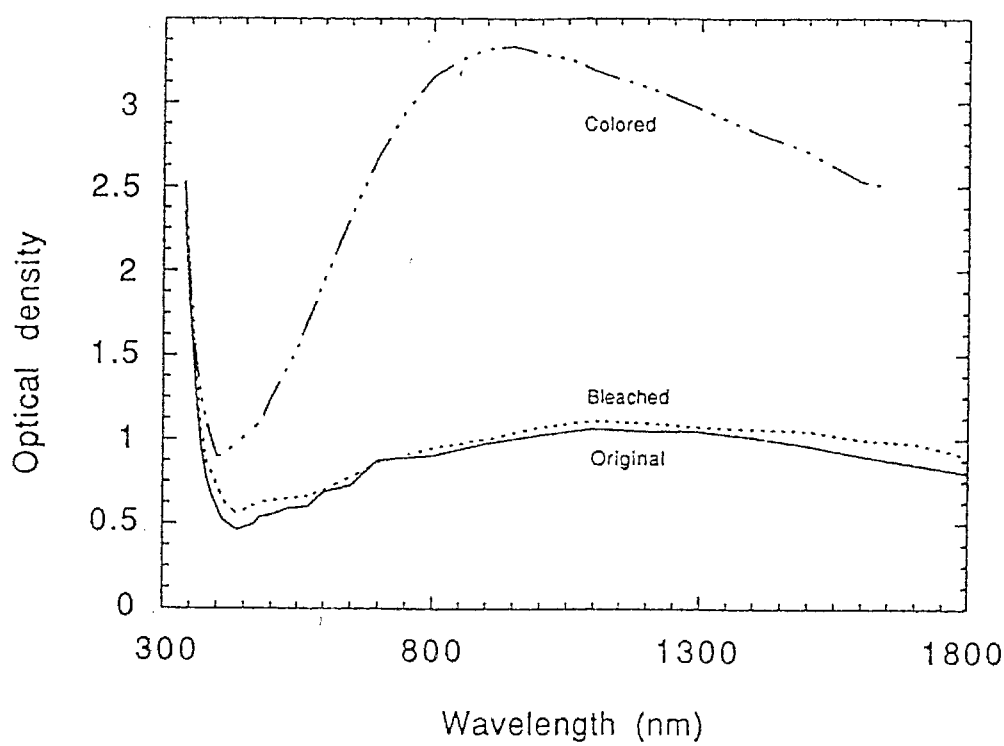

Fig. 5.18 Optical absorption of WO_3 films upon lithium intercalation

The absorption spectrum of the colored Li_xWO_3 film is quite similar to that of the H_xWO_3 films. The main absorption occurs at near infrared spectrum region of 900 nm. The lithium concentration in the colored sample was about x = 0.16. The measurements were conducted using the same procedure as for H_xWO_3 films. Figure 5.19 shows the relation of optical density and the charge densities (proportional to the lithium concentration). A relative optical density was used in Fig. 5.19 in which the optical density of transparent WO_3 film was set to be zero.

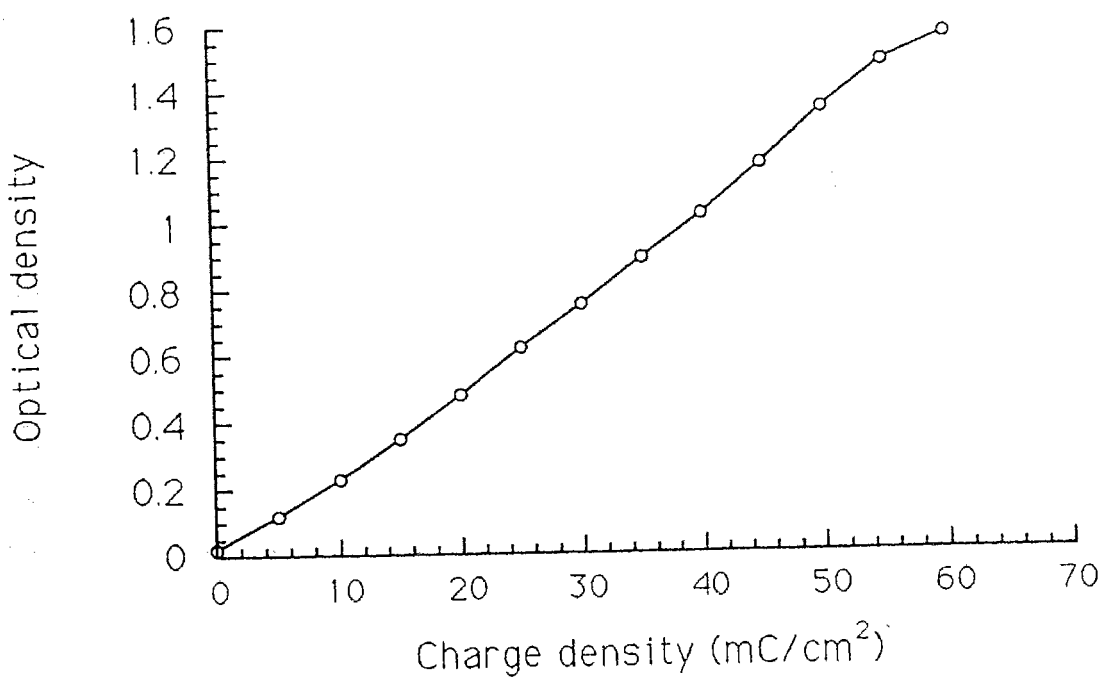

Fig. 5.19 The relation between the optical density of Li_xWO_3 film and the inserted charge density.

The optical density in the Li_xWO_3 film shows an approximately linear relation to the charge density in the range from 0 to 50 mC/cm^2, i.e in

the range of lithium concentration from x = 0 to x = 0.22 above which the slope of the curve decreases.

The chemical diffusion coefficient of the lithium in the WO_3 films were also measured. Since we have the data of $\delta E_x/\delta x$ from the battery cell, the lithium diffusion coefficients D_{Li} were calculated using the slope of $\delta E_t/\delta\sqrt{t}$ obtained by the current step technique. Table 5.9 lists the results. The lithium diffusion coefficient D_{Li} was measured in the discharge. As was indicated by Fig. 5.11, Li_xWO_3 underwent two phase transitions in the discharge when x varied from 0 to 0.5. The diffusion coefficient measurement was based on a theory suitable only for a single phase host. The data in table 5.9 correspond to the D_{Li} in three single phases (monoclinic x = 0.0; tetragonal x = 0.05; and cubic x = 0.3, x = 0.48). It is found that the D_{Li} in the tetragonal phase is almost the same as that in the cubic phase.

Table 5.9 The lithium diffusion coefficients in WO_3 and Li_xWO_3 films.

x in Li_xWO_3	Voltage of the cell (v.s Li/Li^+)	D_{Li} ($cm^2\ s^{-1}$)
0.0	3.2V	1.7×10^{-11}
0.05	2.7V	3.0×10^{-12}
0.3	2.5V	4.0×10^{-12}
0.48	1.9V	4.1×10^{-12}

5.5 Discussions

From above experiments it is clear that the hydrogen and lithium tungsten bronzes are formed in the coloration process. In this section the optical

properties and the crystal structures of these tungsten bronzes will be further discussed.

The optical density

The original WO_3 films were transparent in the visible and near infrared regions. The optical absorption of the WO_3 film changed after the hydrogen or lithium intercalated. Comparing the optical absorption spectra of H_xWO_3 (figure 5.5) and Li_xWO_3 (figure 5.18) films, both tungsten bronzes have their broadened absorption peaks in the near infrared region at about 900 nm (1.38 eV). This phenomena is due to the free electron behaviour in the colored H_xWO_3 and Li_xWO_3 films (Mendelsohn and Goldner 1984; Goldner el at 1985). After intercalation, the hydrogen or the lithium atoms are believed to be ionized at interstitial sites of the WO_3 host and the electrons are freely moving in the W 5d conduction band. Thus the optical absorption of colored WO_3 films are mainly dependent on the concentrations of intercalated active species.

It should be noticed that there were some different properties between the H_xWO_3 and the Li_xWO_3 films. It was found that the blue color in the Li_xWO_3 films was much more stable than that in the H_xWO_3 films. In an EC cell, the color in H_xWO_3 films usually existed from several hours to several days in an open circuit condition, however, the color in the Li_xWO_3 films could exist from several days to several weeks. The stability differences of the H_xWO_3 and Li_xWO_3 were also found in the EMF of their cells. In a hydrogen based EC cell, the voltage measured between colored H_xWO_3 film and the SCE was not stable. The voltage (typically -50 mV vs. SCE) of

H_xWO_3 in the colored state could change back to the original EMF (~350mV) in several hours. However, in a lithium based battery or X-ray cell, the voltage (2.0V) between the colored Li_xWO_3 film and the Li anode remained for several weeks to several months. These differences may mainly be due to the small size of hydrogen, which makes it more active than lithium, the hydrogen atoms in the colored H_xWO_3 film may reacted more easily with the anion in the electrolyte than the lithium atoms in the Li_xWO_3 film.

The crystal structures of colored H_xWO_3 and Li_xWO_3 films

It has been shown that the WO_3 host changes crystal structures from monoclinic(M) to tetragonal(T) and to cubic(C) after lithium or hydrogen intercalation. Figure 5.20 depicts unit cell relations among these phases. From the diagram, the relations of the unit cell dimensions can be obtained:

$$a_M = 7.310\text{Å}, \quad b_M = 7.540\text{Å}, \quad c_M = 7.695\text{Å}, \quad \beta = 90.89°$$

$$a_T \sim \frac{(a_M + b_M)}{2\sqrt{2}} = 5.250\text{Å}, \quad c_T \sim \frac{c_M}{2} = 3.848\text{Å} \qquad (5.5)$$

$$a_C \sim \frac{(a_M + b_M + c_M)}{6} = 3.758\text{Å} \qquad (5.6)$$

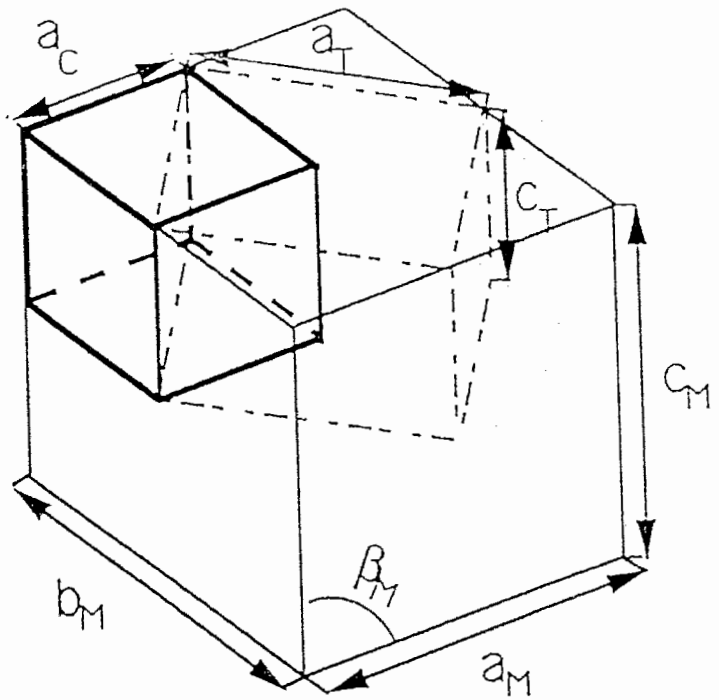

Fig. 5.20 The relations of tetragonal and cubic unit cells to the monoclinic unit cell.

Since the β angle in WO_3 is very close to 90°, the structure of the WO_3 host is a pseudo-orthorhombic. In the original WO_3 host, the WO_6 octahedra are zigzaged in three dimensions, so one has to choose a big unit cell to show its symmetry. There are eight zigzaged WO_6 octahedra sharing in corners in one unit cell.

After the hydrogen or lithium intercalation, the structure of the WO_3 host changes to tetragonal. The zigzags of the octahedra in the c direction disappear ($c_T = \frac{1}{2}c_M$) and W–O bonding lengths in the a and b directions

become equal ($a_T = b_T$). There are two WO_6 octahedra in one tetragonal unit cell.

With more intercalated lithium, the structure of the WO_3 host finally changes to cubic. The zigzags of WO_6 octahedra finally disappear in three dimensions ($a_C \sim \frac{1}{2}a_M$, $\frac{1}{2}b_M$ or $\frac{1}{2}c_M$) and the W-O bonding length becomes equal in three dimensions ($a_C = b_C = c_C$); there is then only one WO_6 octahedron in the unit cell. In figure 5.21, comparable unit cell dimensions for three phases are plotted, they are $\frac{1}{2}a_M$, $\frac{1}{2}b_M$, $\frac{1}{2}c_M$, $a_T/\sqrt{2}$, c_T and a_C.

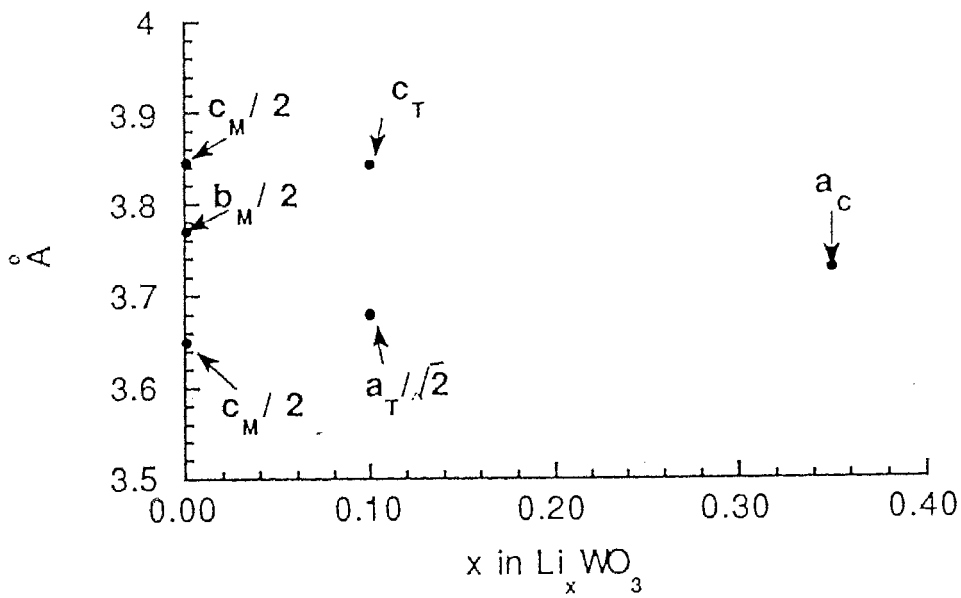

Fig. 5.21 The comparison of unit cell dimensions among three phases.

It will be interesting to discuss the volume change for these three phases. There are eight WO_6 octahedra in the monoclinic unit cell, two in

the tetragonal cell and one in the cubic cell. It is easy to calculate the unit cell volumes for monoclinic (V_M), tetragonal (V_T) and cubic (V_C) phases. keeping the unit cell relations in mind (see figure 5.20), we compared the values of $V_M/8$, $V_T/2$ and V_C. The data are listed in table 5.10.

Table 5.10 The comparison of unit cell volumes of three phases

Phase	Unit cell volume	Comparison
Monoclinic WO_3	$V_M = 424.1Å^3$	$V_M/8 = 53.01Å^3$
Tetragonal Li_xWO_3	$V_T = 104.3Å^3$	$V_T/2 = 52.15Å^3$
H_xWO_3	$V_T = 104.0Å^3$	$V_T/2 = 52.00Å^3$
Cubic Li_xWO_3	$V_C = 51.73Å^3$	$V_C = 51.73Å^3$

It was found that the lattice dimensions of WO_3 host shrink after lithium or hydrogen intercalation. As was mentioned before, the intercalated hydrogen and lithium atoms were suggested to be at interstitial sites as depicted in figure 5.22. The hydrogen and lithium atoms will be ionized at room temperature and the electrons will enter into the tungsten 5d conduction band, or one may say the electrons will enter into the tungsten 5d orbital, localizing around the W atoms. The ionized H^+ or Li^+ ions at interstitial positions could attract the surrounding $O^=$ ions in the lattice. This attraction may cause the lattice to change to a smaller size.

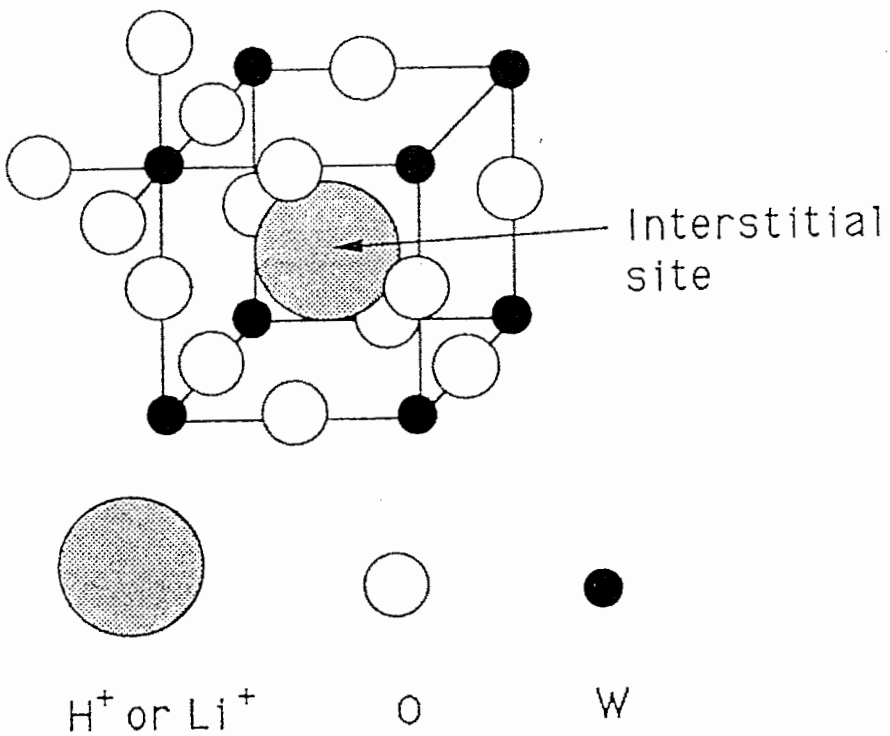

Fig. 5.22 The interstitial site in the WO_3 host.

Chapter 6

Lithium intercalation in WO_3 powders

In Chapter 5 we studied the intercalation of hydrogen and lithium atoms in the evaporated WO_3 films. In this chapter the lithium intercalation in various WO_3 powders will be investigated. The data obtained in this chapter may help us to further understand the lithium intercalation mechanism in the WO_3 materials.

6.1 WO_3 powders made from H_2WO_4

There were two kinds of WO_3 powders used in this study: the one was commercial WO_3 powder as mentioned at 5.1 and the other was made from thermo-decomposition of H_2WO_4 (tungstate) powder in air according to the following reaction:

$$H_2WO_4 \xrightarrow{\text{heated}} WO_3 + H_2O \qquad (6.1)$$

A TGA (thermal Gravimetric Analysis) data (figure 6.1) shows that the tungstate began its decomposition at about 200°C. A pure WO_3 was obtained when temperature reached to 300°C. The weight loss (6.6%) at the temperature region from 200°C to 300°C could be attributed to the loss of water as described by the reaction of (6.1) and the loss of the moisture originally adsorbed in the H_2WO_4 powders. When the temperature was raised

to 750°C some WO_3 may begin to evaporate. Three WO_3 powders were prepared with this method, they were obtained by heating H_2WO_4 powder (99.5% 7783-03-1, Aldrich) at 400°C, 700°C and 900°C in air for 10 to 15 hours. In the following discussion, we will call them 400, 700 and 900 WO_3 powder, respectively.

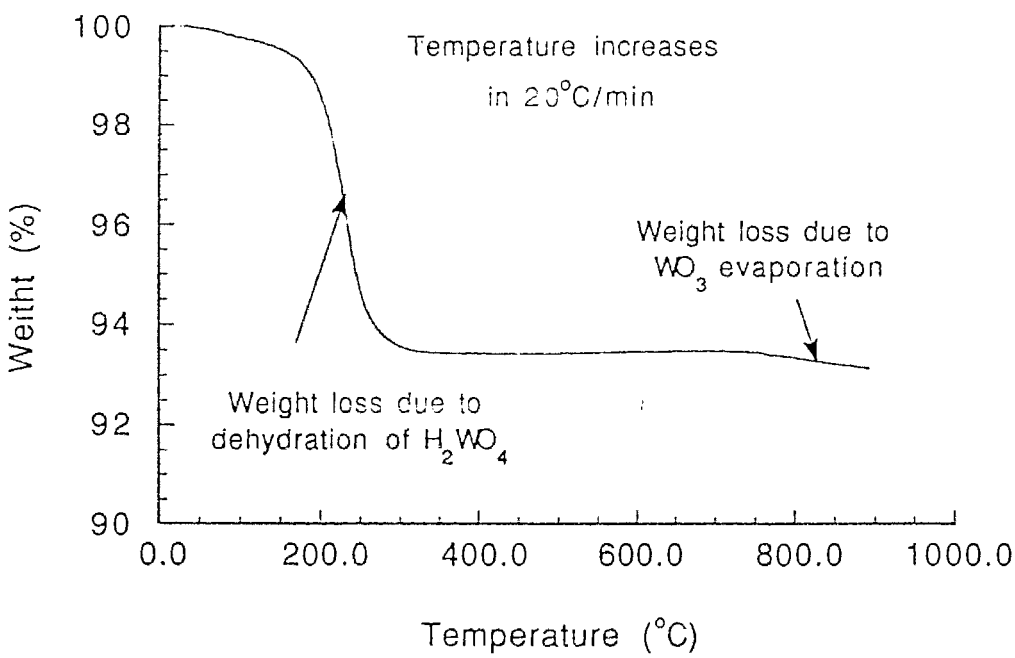

Fig. 6.1 The TGA data for the thermal decomposition of H_2WO_4 powder

6.2 Physical characters of prepared WO_3 powders

6.2.1 Crystal structures

It has been known that the crystal structure of the commercial WO_3 is monoclinic. All WO_3 powders obtained by heating the H_2WO_3 also showed the monoclinic structure. Their X-ray diffraction patterns are shown in figure 6.2 (a), (b) and (c). It was found that the higher the preparation temperature was, the sharper the diffraction peaks were. From the TGA analysis, it was clear that the H_2WO_4 decomposed completely at 300°C, above which the higher temperature would make the crystal grains grow larger.

6.2.2 Surface areas

The surface area was another indication which showed that the WO_3 powders prepared at different temperature had different crystal sizes. The surface area of the commercial and the prepared WO_3 powder were measured on a Quantaorp Sorption System. The results are listed in table 6.1. The data shows that the WO_3 powder prepared at 400°C has the largest surface area which is about 15 times as large as that of the commercial WO_3 powder and the 900 WO_3 powder.

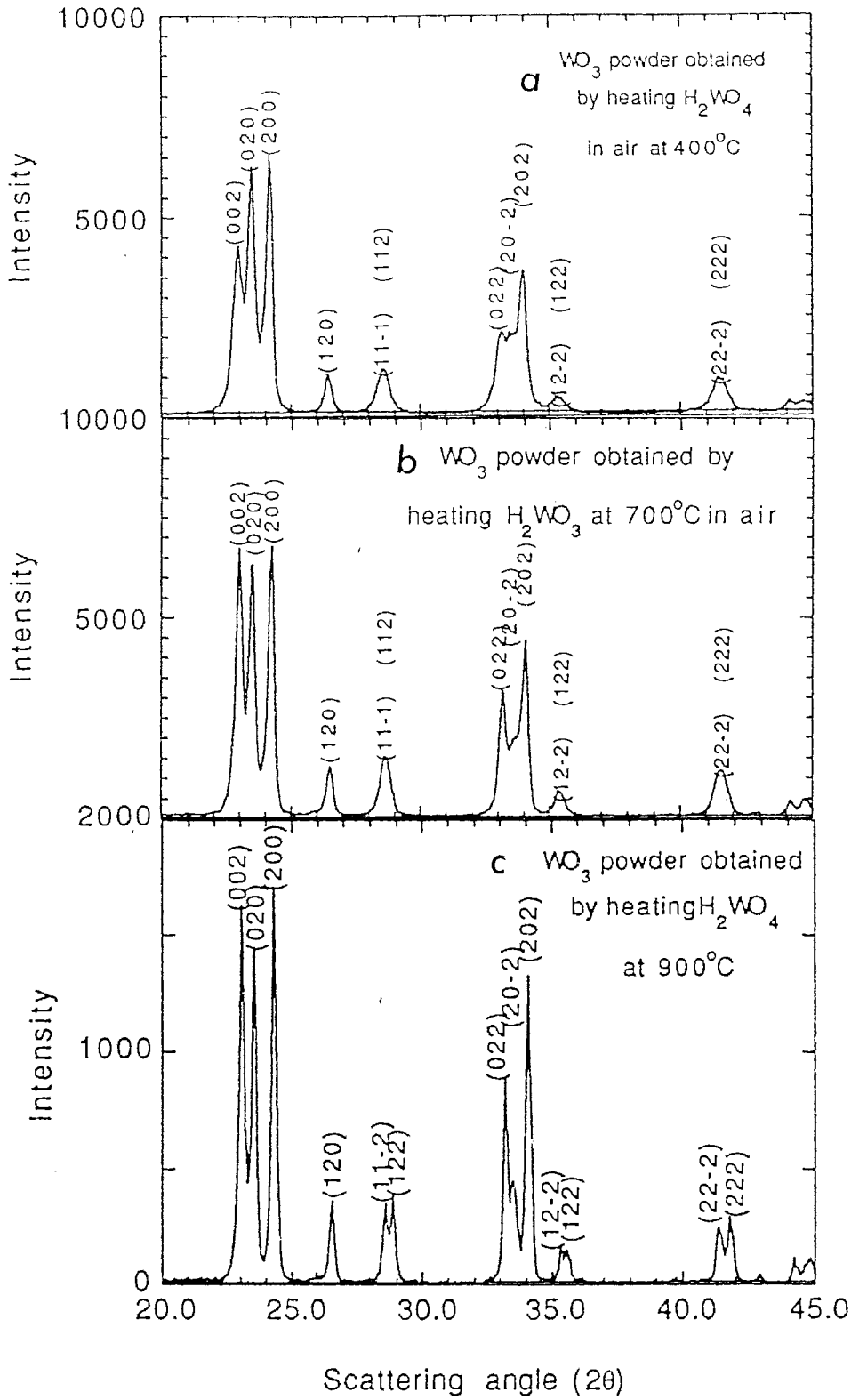

Fig. 6.2 (a) The X-ray diffraction pattern of the 400 WO_3 powder.

(b) The X-ray diffraction pattern of the 700 WO_3 powder.

(c) The X-ray diffraction pattern of the 900 WO_3 powder.

Table 6.1 The surface area of the commercial and the prepared WO_3 powders

WO_3 powders	Surface area (m^2/gm)
*400°C	12.2
*700°C	4.3
*900°C	0.47
commercial	0.85

* This is the temperature under which the H_2WO_3 was heated to prepare the WO_3 powders.

6.3 The lithium intercalation in the WO_3 powders

The powder films were prepared with the method described in Chapter 3 and the battery cells were used to study the lithium intercalation. Figure 6.3 shows the discharge/charge curves of various WO_3 powder cells. The EMF curves are plotted as a function of the time. The currents used for all cells correspond to $\delta x = 1$ in Li_xWO_3 in 50 hours. It is interesting to notice the phenomena that the lithium intercalation behavior is totally different in those WO_3 powders made at different temperature although they seem to be chemically and structurally the same.

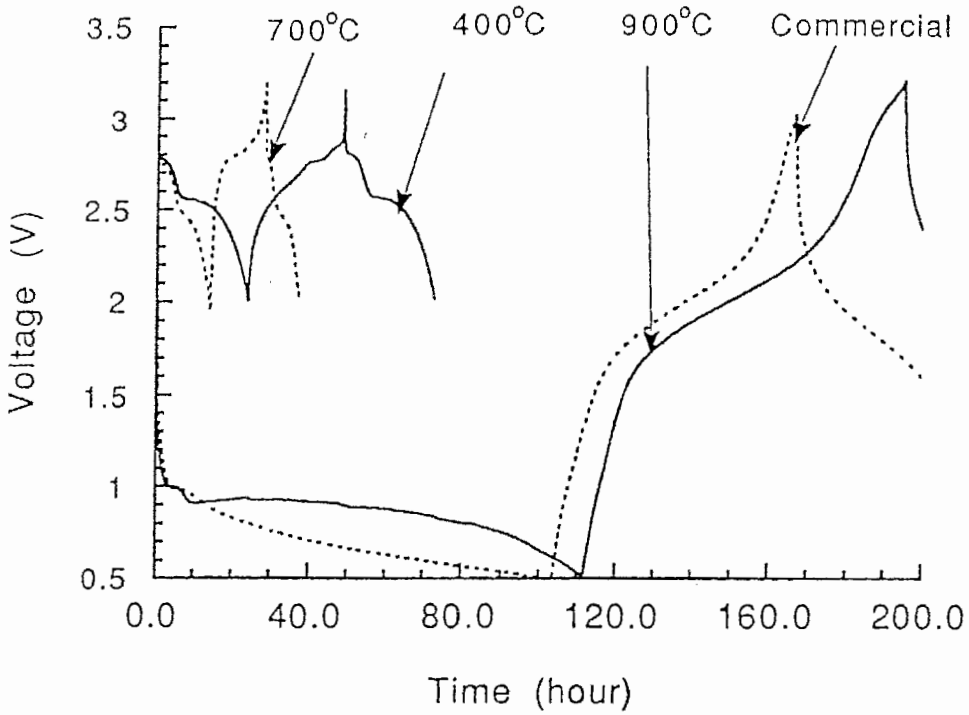

Fig. 6.3 The discharge/charge curves of various WO_3 powder cells

The 400 WO_3 powder shows similar discharge/charge behavior to the WO_3 film as is depicted in figure 6.4 (a). The derivative plots show more clearly similarities between the 400 WO_3 powders and the films (figure 6.4 b and c). Both 400 WO_3 powder and the WO_3 film undergo two phase changes during either discharge or charge process and both materials show almost the same capacities for the lithium intercalation. A structure analysis for the 400 WO_3 powder after Li intercalation will be discussed in next section.

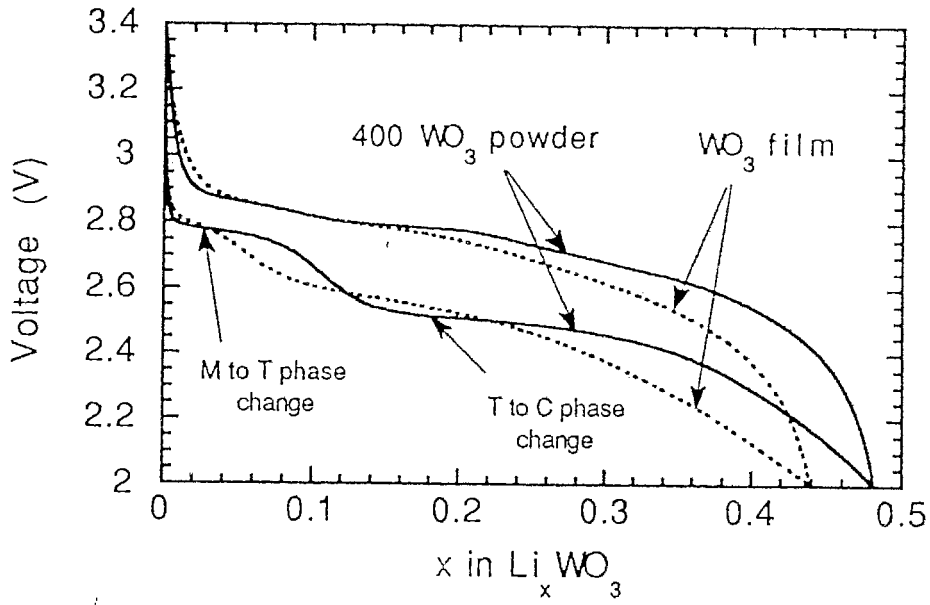

Fig. 6.4 (a) The discharge/charge curves of 400 WO_3 powder and WO_3 film.

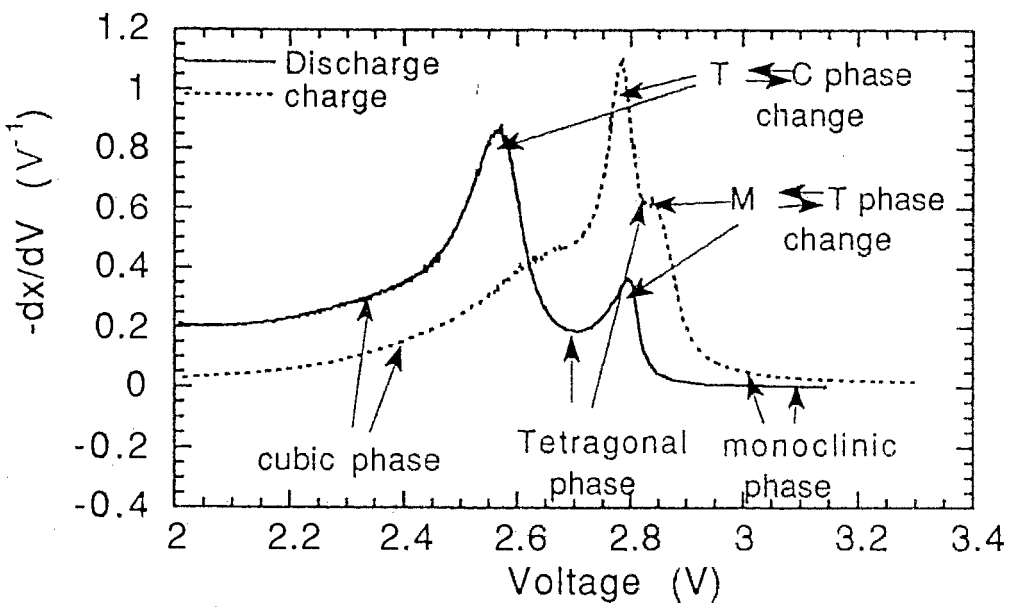

Fig. 6.4 (b) The derivative plots for 400 WO_3 films.

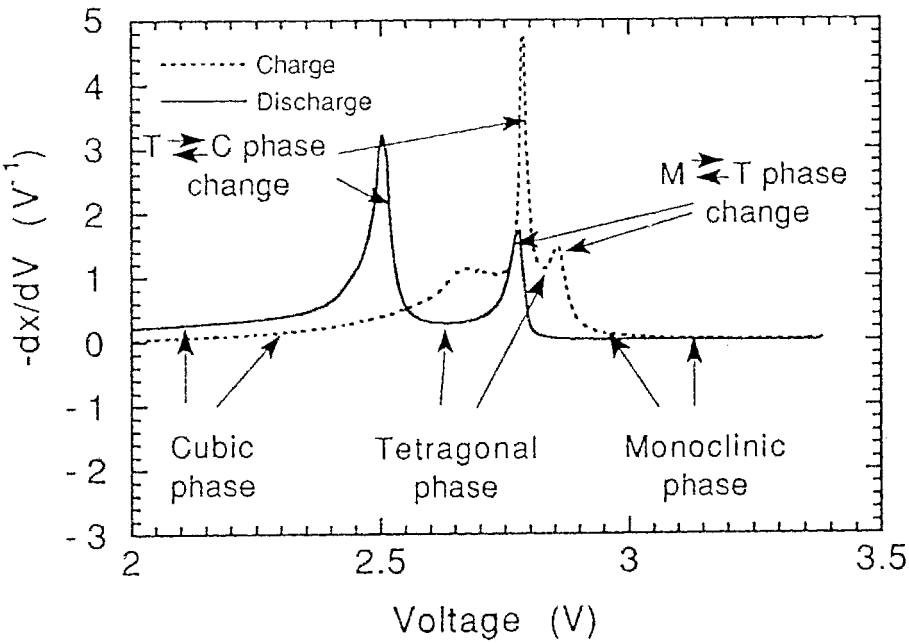

Fig. 6.4 (c) The derivative plots of charge curves for 400 WO_3 powder and WO_3 film.

For the 700 WO_3, the phase changes are found to appear at different voltages from that in the WO_3 film and the 400 WO_3 powder. The capacity of 700 WO_3 powder for the lithium intercalation is different as well. At 2.0V, the quantity of the intercalated lithium in 700 WO_3 powder is only about half that in the 400 WO_3 powder. As to the 900 WO_3 powder and the commercial powder, the discharge/charge curves are totally different from that of 400 WO_3 and 700 WO_3 powders. The lithium can not intercalate into these two powders until the voltage of the cell reaches to 1.0V. The data shown here strongly indicate that some critical change must occur in the WO_3 powders when it was heated at high temperature. The X-ray data show that the commercial WO_3 powder keeps its monoclinic structure until 1.0V

in discharge. The monoclinic phase in WO_3 powder gradually disappears when the voltage of the cell goes down to 0.5V. Figure 6.5(a) and (b) show the X-ray diffraction patterns for the commercial WO_3 powder at 0.8V and 0.5V in a X-ray cell. The monoclinic phase almost totally disappears at 0.5V and the structure turns almost amorphous which is quite similar to the structure of the WO_3 films at 0.5V (Fig. 5.17). From the measured surface area, it seems that the smaller the surface area (or the larger the crystal size), the lower the capacity. To explain the main mechanism of the different behavior of the lithium intercalation in those 400, 700 and 900 WO_3 powders may need further extensive studies on physical and chemical properties of these materials. In this thesis, we were mainly concerned with the properties of lithium intercalation in the 400 WO_3 powder because this powder showed similar properties to the WO_3 films.

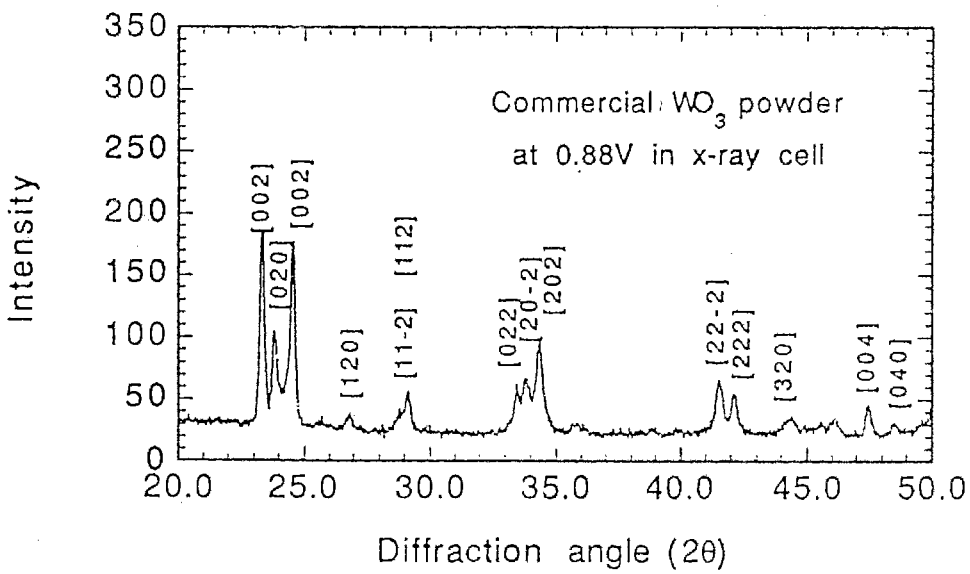

Fig. 6.5 (a) The X-ray diffraction pattern of commercial WO_3 powder at 0.88V.

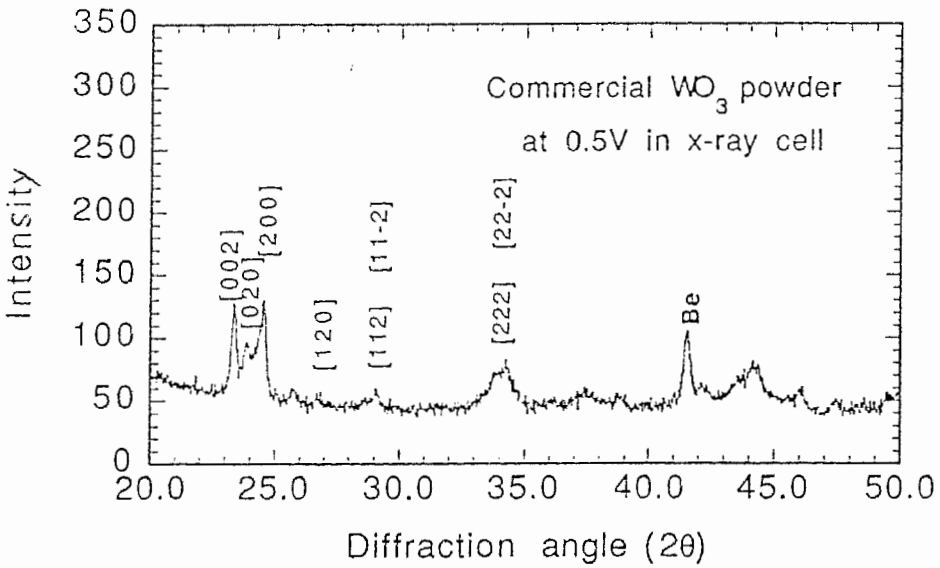

Fig. 6.5 (b) The X-ray diffraction pattern of commercial WO_3 powder at 0.5V.

6.4 Tetragonal and cubic phases in 400 WO_3 powders

As was discussed in chapter 5 and this chapter, there are two phase transitions in the polycrystalline WO_3 films and the 400 WO_3 powder during the lithium intercalation in between the voltage range from 3.2V to 2.0V. In the following subsections, the crystal structures of the tetragonal and the cubic Li_xWO_3 (in 400 WO_3 powder) will be analyzed.

6.4.1 The phase changes in the 400 WO_3 powder

It has been known that the original 400 WO_3 powder is monoclinic. Considering the similarity of discharge/charge between the 400 WO_3 powder and the polycrystalline WO_3 film (figure 6.4 (a) to (c)), the phase changes: monoclinic -> tetragonal -> cubic are expected in the 400 WO_3 powder. From the derivative plots in figure 6.4 (c), the different phase regions may be determined. The results are listed in table 6.2:

Table 6.2 The phase regions in 400 WO_3 powder with respect to the voltage of the cell.

in discharge	monoclinic	(3.20 - 2.83V)
	mono.-> tetr.	(2.83 - 2.75V)
	tetragonal	(2.75 - 2.57V)
	tetr.-> cub.	(2.57 - 2.38V)
	cubic	(2.38 - 2.00V)
in charge	cubic	(2.00 - 2.78V)
	cub.-> tetr	(2.78 - 2.82V)
	tetragonal	(2.82 - 2.84V)
	tetr.-> mono.	(2.84 - 2.88V)
	monoclinic	(2.88 - 3.20V)

It should be noticed that the phase changes occur at different voltages during the discharge and the charge. The peak for monoclinic -> tetragonal. phase change occurs at about 2.77V in discharge but the peak for the tetragonal -> monoclinic phase change occurs at about 2.85V in the charge process. The peak for the tetragonal -> cubic phase change lies at 2.5V in discharge but the peak for the cubic -> tetragonal phase change lies at 2.78V in charge. We call this phenomena hysteresis. When we carefully look at the derivative charge curves in figure 6.4 (c), it is noticed that the -dx/dv shows a peak like shape in the 2.62V to 2.73V

voltage region in the charge process. It will be shown that the WO_3 host in that region still has a cubic phase, but the unit cell dimension of the cubic WO_3 host has to be changed due to more and more lithium atoms extracted from the WO_3 host.

6.4.2 The tetragonal phase in 400 WO_3 powder

The X-ray diffraction data from the WO_3 powder is much more reliable and accurate than that from the WO_3 film because the peaks appearing in the powder pattern are sharper and clearer. With the method described in Chapter 5, the X-ray data obtained from the beryllium X-ray cell was converted to a pattern without the effect of the beryllium absorption and then the Rietveld profile refinement method was used to determine the crystal structure. A tetragonal phase was found when the X-ray cell was at 2.65V with $x = 0.095$ in Li_xWO_3 in discharge process. Table 6.3 lists the refined atomic parameters for the tetragonal Li_xWO_3 unit cell. Figure 6.6 shows the profile fitting results. The refinement R factor is 0.048 (4.8%). In the intensity calculations, the reflections from the beryllium sheet were excluded. From the calculated results, it was found that the tetragonal phase in 400 WO_3 powder is the same as that in the WO_3 film.

Table 6.3 Structural parameters for the tetragonal Li_xWO_3 and the intensity refinements.

Space group: P4/nmm

Cell dimensions: a = 5.203(3)Å, c = 3.844(2)Å

Refined R factor: R = 0.048

Origin at 2/m

	x	y	z	B
W1	0.25,	0.25,	0.432,	1.0
W2	0.75,	0.75,	0.568,	1.0
O1	0.25,	0.25,	0.932,	4.8
O2	0.75,	0.75,	0.068,	4.8
O3	0.00,	0.00,	0.50,	4.8
O4	0.50,	0.50,	0.50,	4.8
O5	0.50,	0.00,	0.50,	4.8
O6	0.00,	0.50,	0.50,	4.8

h k l	$2\theta_o$	$2\theta_c$	I_o	I_c
0 0 1	23.151°	23.075°	42.2	46.3
1 1 0	24.203°	24.199°	100.0	97.8
0 1 1	28.936°	28.890°	17.4	17.7
1 1 1	33.710°	33.736°	45.5	46.6
0 2 0	34.458°	34.447°	28.8	27.2
0 2 1	41.995°	42.000°	17.8	17.9
1 2 1	45.602°	45.590°	9.8	9.8
0 0 2	47.301°	47.321°	4.1	4.3
2 2 0	49.554°	49.570°	16.8	15.4
1 1 2	53.848°	53.841°	8.4	8.2
1 3 0	55.882	55.900°	18.5	16.8
3 1 1	61.301°	61.308°	18.8	16.5
1 2 2	62.655°	62.728°	12.1	11.7

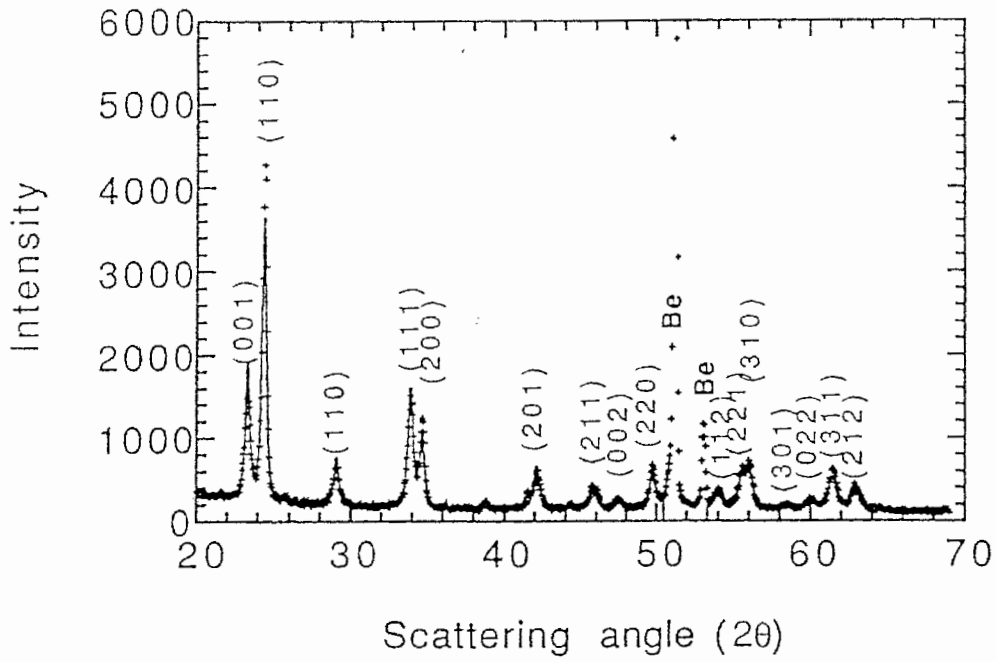

Fig. 6.6 Raw X-ray data (+++) and calculated profile (——). for the tetragonal Li_xWO_3 powder.

6.4.3 The cubic phase in 400 WO_3 powder

The structure parameters of the cubic phase for the 400 WO_3 powder were determined in the same way as was done for the tetragonal phase. The X-ray pattern obtained at 2.0V (x = 0.44 in Li_xWO_3 powder) showed the cubic phase. The cubic phase of Li_xWO_3 powder belongs to the space group Pm3m as is the case for the cubic Li_xWO_3 film. The W atom is at the (0, 0, 0) position and the O atoms at the (0, 0, 0.5), (0, 0.5, 0) and (0.5, 0, 0) positions, respectively. The lattice constant obtained is a = 3.729(1)Å and the refinement R factor is 0.037. Table 6.4 lists the refined results and figure 6.7 shows the raw and calculated X-ray profiles. In figure 6.7, the beryllium contributions were excluded from the calculation.

Table 6.4 The raw and calculated peak positions and intensities of x-ray pattern for the cubic Li_xWO_3 powder, a = 3.729Å.

h k l	$2\theta_o$	$2\theta_c$	I_o	I_c
0 0 1	23.862	23.874	100.0	100.5
0 1 1	34.024	34.017	57.7	55.5
1 1 1	42.892	41.986	14.4	13.3
0 0 2	48.876	48.872	18.9	20.1
0 1 2	55.082	55.096	20.1	21.9
1 1 2	60.860	60.882	25.3	23.7

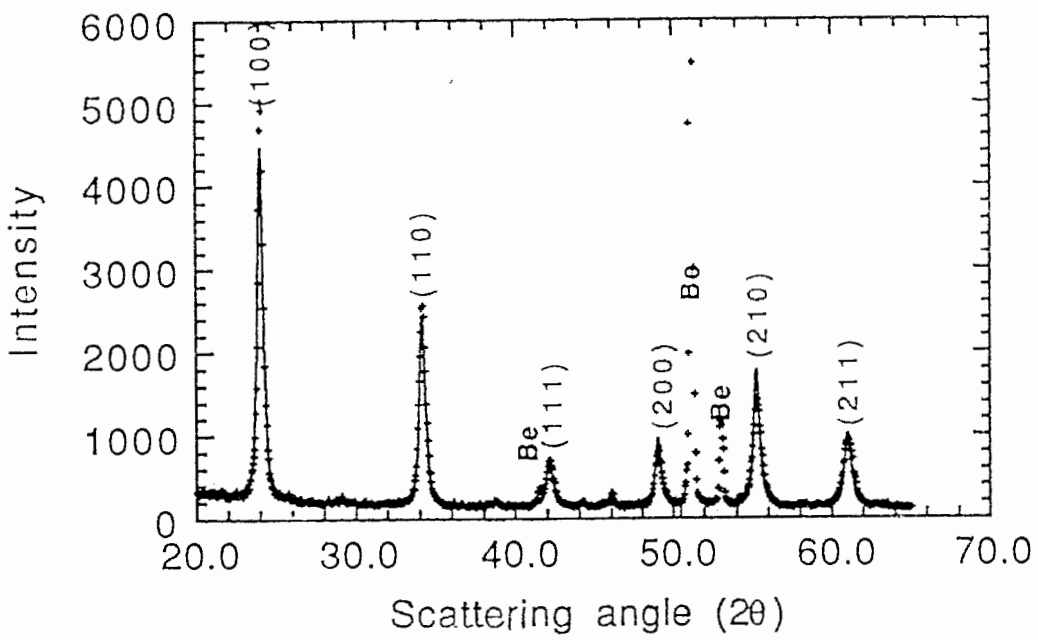

Fig. 6.7 The raw X-ray pattern of the cubic phase (+++) and the calculated cubic profile (——).

6.5 The phase analysis in phase change regions

In this section the structures of 400 WO_3 powder in phase change regions will be studied. To study the phase changes in 400 WO_3 powders, two *in situ* X-ray experiment were carried out. In the *in situ* X-ray experiments, a constant current was applied to the X-ray cell while a sequence of X-ray patterns were collected. In the first *in situ* X-ray experiment, the current used corresponded to make a change of $\delta x = 1$ in Li_xWO_3 in 200 hours. The voltage limits for charge and discharge were selected at 2.75V and 3.2V. 26 X-ray diffraction patterns were collected in about two discharge/charge cycles. The X-ray patterns were collected in the 2θ regions: from 22° to 25° and from 32° to 36°. The changes in δx in one x-ray pattern was less than 0.02. In second *in situ* X-ray experiment, the current selected corresponded to a change of $\delta = 1$ in Li_xWO_3 in 100 hours and the voltage limits were at 3.2V and 2.0V. 54 X-ray patterns were collected in about one and a half discharge/charge cycles. The X-ray patterns were collected from $2\theta = 20°$ to $2\theta = 70°$. The changes in δx in each X-ray pattern was less than 0.03 in this second *in situ* X-ray experiment.

6.5.1 Monoclinic – tetragonal phase changes

To reveal the nature of the 400 WO_3 powder in the monoclinic–tetragonal phase change region, the X-ray patterns obtained from the first *in situ* x-ray experiment were analyzed. Figure 6.8 (a) shows the discharge/charge curves from this *in situ* X-ray experiment. The circles on the curve show the voltage of the cell and the x in the Li_xWO_3 powder at the middle time of each X-ray pattern scanning. In this *in situ* experiment the X-ray cell

only discharge/charged in between 3.2V and 2.75V to analyze the monoclinic-tetragonal phase change.

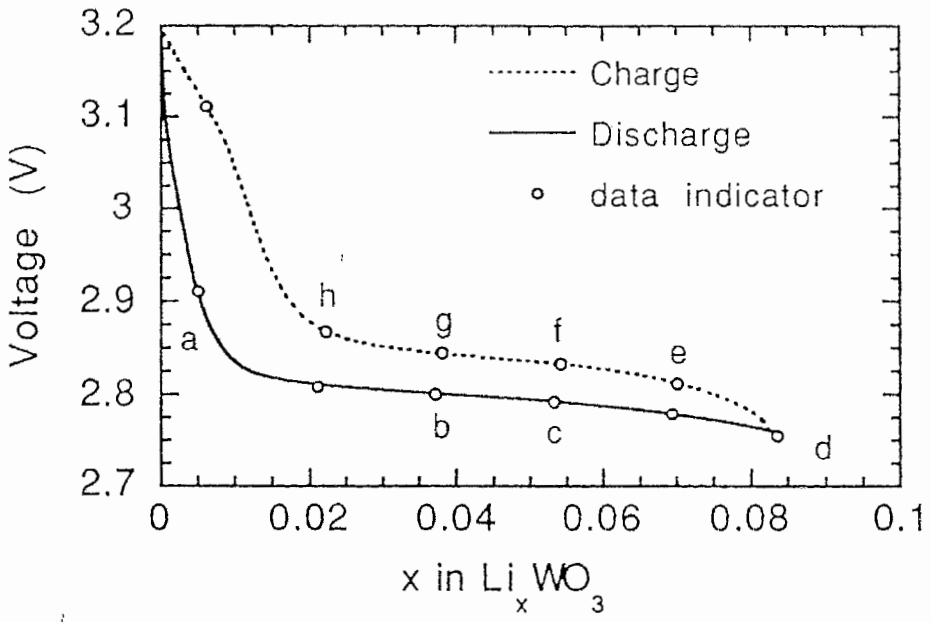

Fig. 6.8 The EMF data of the first *in situ* X-ray cell.

The X-ray data obtained at 3.10V (circle a in figure 6.8 and pattern a in figure 6.9) shows a monoclinic phase. The data obtained at 2.75V (circle d in figure 6.8 and pattern d in figure 6.9) shows a tetragonal phase. It was found that all X-ray patterns obtained between 2.75V and 3.10V can be expressed by certain combinations of pattern (a) and (d). Two sample calculations are shown in figure 6.9.

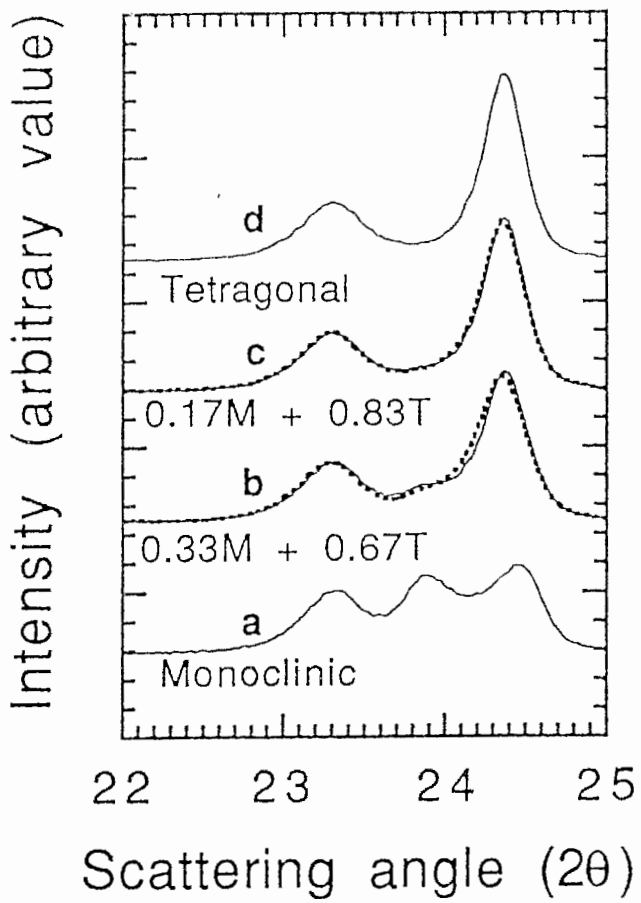

Fig. 6.9 The X-ray patterns: (a) monoclinic, (d) tetragonal; (b) and (c) expressed by the combinations of patterns (a) and (d). In pattern (b) and (c), the solid lines are the raw data, the dashed line is from the combination of (a) and (d).

Figure 6.9 shows that the X-ray pattern (b) obtained at 2.803V in discharge containing 33% monoclinic phase and 67% tetragonal phase;

pattern (c) contains 17% monoclinic phase and 83% tetragonal phase. The other X-ray patterns were also analyzed and the results are listed in table 6.5.

Table 6.5 Phase analysis for the monoclinic-tetragonal phase change

X-ray pattern	Two phase combination	R
discharge 2.821V	(0.80Mono. + 0.20Tetr.)	0.062
2.803V(b)	(0.33Mono. + 0.67Tetr.)	0.045
2.784V(c)	(0.17Mono. + 0.83Tetr.)	0.042
charge 2.811V(e)	(0.23Mono. + 0.77Tetr.)	0.09
2.833V(f)	(0.50Mono. + 0.50Tetr.)	0.085
2.845V(g)	(0.71Mono. + 0.29Tetr.)	0.07
2.867V(h)	(0.93Mono. + 0.07Tetr.)	0.058

Where R is a profile fitting parameter:

$$R = \frac{\Sigma |Y_{o,i} - Y_{c,i}|}{\Sigma Y_{o,i}} \qquad (6.2)$$

where $Y_{o,i}$ is the observed intensity at step i in the X-ray experiment and $Y_{c,i}$ is the calculated intensity at step i by combining the correspondent step i intensities in the monoclinic pattern (a) and the tetragonal pattern (d). In table 6.5 R was calculated through the experimental scattering angles from $2\theta = 22°$ to 25° and 32° to 36°. It can be seen that all R values calculated were smaller than 0.09. According to these data, we believe that the phase change of monoclinic <——> tetragonal in Li_xWO_4 powders is a discontinuous phase change. In discontinuous phase change more than one distinguishable phases may coexist.

6.5.2 Tetragonal – cubic phase changes

The X-ray patterns taken from the second *in situ* X-ray experiment were analyzed. Figure 6.10 shows the EMF curves from the second *in situ* X-ray cell in the charge and discharge processes. The circles on the curves also indicate the X-ray patterns. In this analysis, the same procedures were used as that used in the last section. According to table 6.2, the tetragonal to cubic phase change occurs in the voltage region of 2.57V to 2.38V in the discharge and the Cubic to tetragonal phase change occurs in the voltage region of 2.78V to 2.82V in the charge. All X-ray diffraction patterns including in these two phase change regions were analyzed by the Rietveld profile refinement method. It was found that pattern (a) (*in situ* cell at 2.67V) in figure 6.10 showed a tetragonal phase and pattern (d) (*in situ* cell at 2.0V) in figure 6.10 showed a cubic phase.

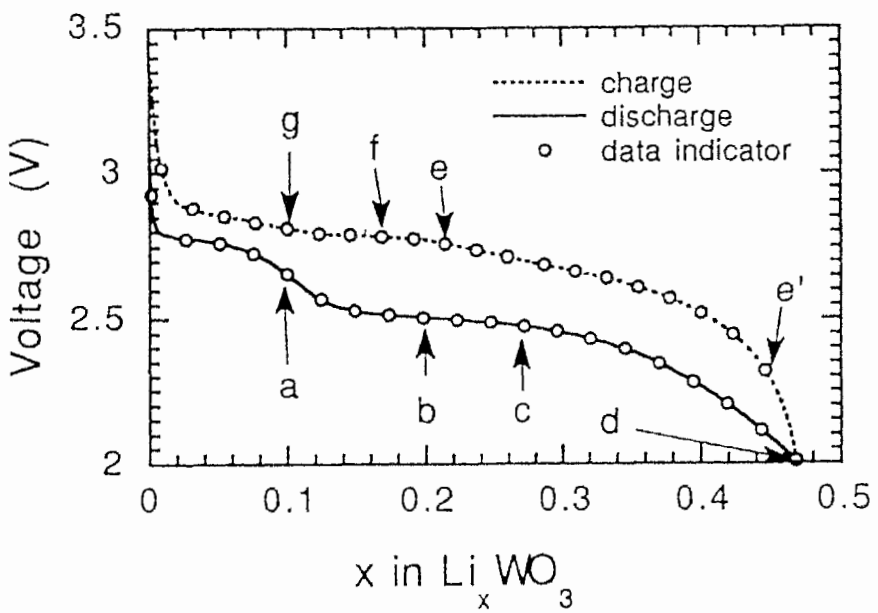

Fig. 6.10 The EMF curves of the second *in situ* X-ray cell.

These two patterns were used to analyze the X-ray patterns obtained between 2.60V and 2.40V in the discharge process. The X-ray patterns obtained at the voltage between 2.60V to 2.40V in discharge were expressed by the combinations of the pattern (a)(tetragonal) and (d)(cubic). Figure 6.11 shows two samples where pattern (b) obtained at 2.51V can be attributed to the combination of 78% tetragonal phase and 22% cubic phase; pattern (c) obtained at 2.473V can be attributed to the combination of 44% tetragonal phase and 56% cubic phase.

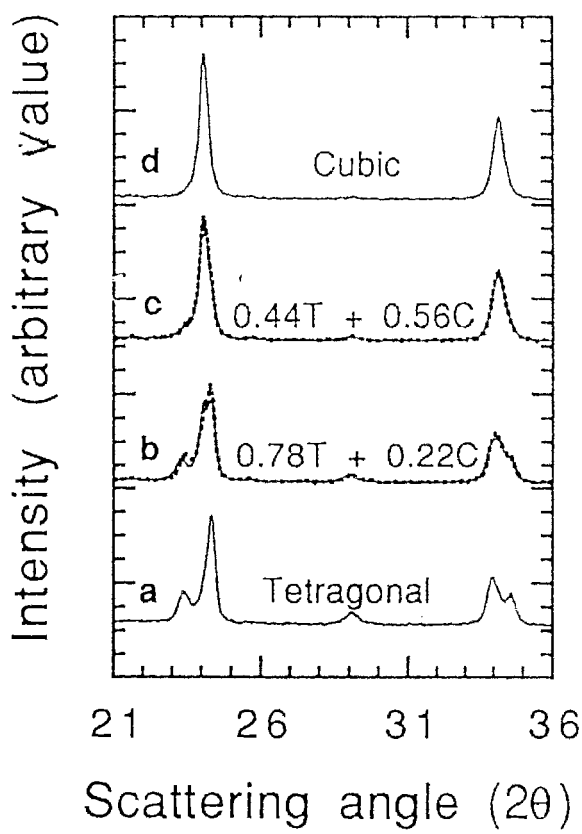

Fig. 6.11 The X-ray patterns: (a) is tetragonal, (d) is cubic, (b) and (c) can be expressed by the combinations of patterns (a)(tetragonal) and (d)(cubic). In pattern (b) and (c), the solid lines are the raw data, the dashed line are from the combination of (a) and (d).

As was discussed in section 6.4.1, the cubic phase of Li_xWO_3 powder may have a cell dimension change in the charge process. To analyze the X-ray patterns from 2.78V to 2.82V in the charge process, the X-ray diffraction pattern at 2.762V (indicated as (e) in figure 6.9) was used as the cubic phase to analyze the cubic–tetragonal phase change in the charge process. The analyzed results are listed in table 6.6.

Table 6.6 The phase analysis for tetragonal–cubic phase changes

	X-ray pattern	Phase combination	R value
discharge process	2.51V (b)	(0.78Tetr.+ 0.22Cub.)	0.084
	2.50V	(0.66Tetr.+ 0.34Cub.)	0.084
	2.487V	(0.54Tetr.+ 0.46Cub.)	0.083
	2.473V(c)	(0.44Tetr.+ 0.56Cub.)	0.078
	2.458V	(0.33Tetr.+ 0.67Cub.)	0.075
	2.432V	(0.26Tetr.+ 0.74Cub.)	0.072
	2.396V	(0.18Tetr.+ 0.82Cub.)	0.066
charge process	2.785V(f)	(0.18Tetr.+ 0.72Cub.)	0.105
	2.790V	(0.34Tetr.+ 0.66Cub.)	0.083
	2.795V	(0.55Tetr.+ 0.45Cub.)	0.072
	2.812V(g)	(0.77Tetr.+ 0.23Cub.)	0.070

Where the R is defined by equation (6.2) and calculated from $2\theta = 20°$ to 70° with each step of 0.05°. It is seen from table 6.6 that the X-ray patterns obtained in the phase-change region can be accurately expressed by the combinations of tetragonal and cubic phases, therefore we believe that the tetragonal–cubic phase change in Li_xWO_3 is a discontinuous phase change.

6.5.3 The cubic phase in the charge process

As was discussed previously, in the voltage region of 2.6 to 2.78V in the charge process, less and less lithium in the Li_xWO_3 may cause some distortions to the cubic phase and thus a change in lattice constant. The profile refinement results showed that all X-ray patterns from (e')

(2.286V) to (e) (2.762V) in figure 6.10 correspond to cubic phase except for some changes in the unit cell dimensions. The analyzed results are listed in table 6.7 and plotted in figure 6.12. The refinement R factor in table 6.7 has been defined by equation (4.7).

Table 6.7 The variation of the lattice constant in the cubic phase, The data in the parentheses are the standard deviation of the last significant digits.

	X-ray pattern	Lattice constant	R
In charge process	2.286V (e')	3.7273(5)Å	0.033
	2.431V	3.7270(6)Å	0.037
	2.510V	3.7271(5)Å	0.037
	2.567V	3.7271(7)Å	0.031
	2.609V	3.7276(5)Å	0.036
	2.638V	3.7287(4)Å	0.034
	2.663V	3.7295(8)Å	0.036
	2.685V	3.7319(7)Å	0.031
	2.715V	3.7345(6)Å	0.036
	2.739V	3.7376(5)Å	0.042
	2.762V (e)	3.7396(6)Å	0.043

From table 6.7 and figure 6.12, it is found that the lattice constant of the cubic phase remained unchanged in the charge from 2.286V (pattern e') to 2.567V. From 2.609V to 2.762V (pattern e), which corresponds to the peak like curve in figure 6.2 (c), the lattice constant changes from 2.7276Å to 2.7396Å. This analysis confirms the statements in section 6.4.1 that the peak-like -dx/dv curve in the discharge process is not a phase change, but a lattice constant variation in the same cubic phase.

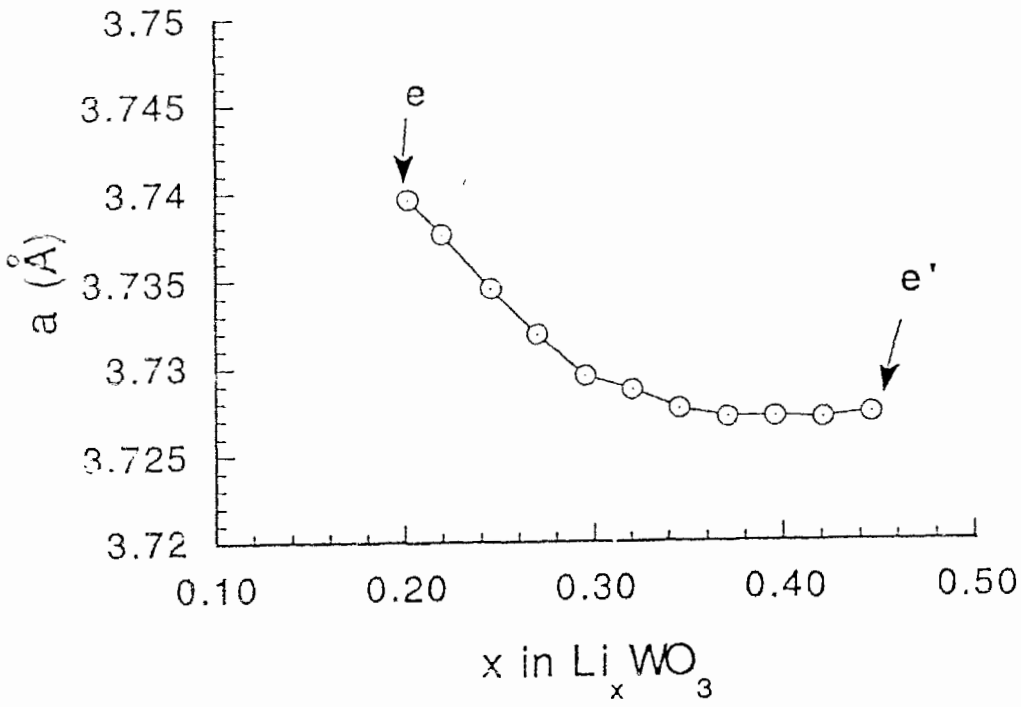

Fig. 6.12 The lattice constant changes with the variation of lithium concentration δx in cubic Li_xWO_3 powder.

6.6 Discussion

6.6.1 The phase diagram of Li_xWO_3 powder

The above study makes it possible to establish a phase diagram for Li_xWO_3. Combining the data in table 6.2, the plots in figure 6.4 (c), and the *in situ* data in figure 6.10, a phase diagram for the 400 Li_xWO_3 powder was obtained. Figure 6.13 shows the diagram. The phase changes in the discharge and charge processes are plotted separately. The single phase and co-existing phase regions for both processes are clearly shown in the

diagram. The hysteresis phenomenon appears in the phase diagram: the phases occur at different x regions in the discharge and charge processes. As is discussed in previous sections, the WO_3 host has a tendency to keep its old phases, therefore the corresponding phase changes occur at different x values in the discharge and charge processes. It may be worthwhile to mention that the phase diagram shown in figure 6.13 only works for 400 WO_3 powder and maybe WO_3 film. Recalling the different voltage curves for 400 WO_3 powder and 700 WO_3 powder, a different phase diagram for 700 WO_3 powder should be expected.

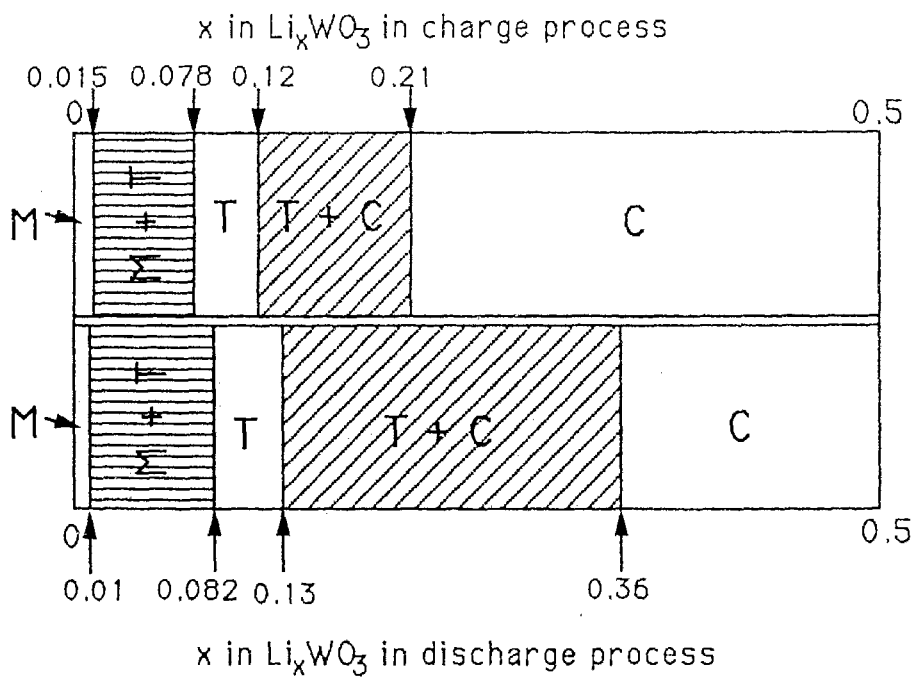

Fig. 6.13 The phase diagram of Li_xWO_3

6.6.2 Comparison between 400 WO_3 powders and WO_3 films

The data analyzed in Chapter 5 and in this chapter show that both WO_3 films and 400 WO_3 powders undergo the same phase changes after lithium intercalation. They have similar EMF curves and derivative curves. The measured tetragonal and cubic phases are also similar in the 400 WO_3 powders and the films. Table 6.8 lists these results.

Table 6.8 Comparisons of the 400 WO_3 powder and the WO_3 film.

	Li_xWO_3 films	Li_xWO_3 powders
Tetragonal phase	a = 5.206Å b = 3.836Å	a = 5.203Å b = 3.844Å
Volume of WO_3 occupancy	V_T = 52.00 Å^3	V_T = 52.03 Å^3
cubic phase	a = 3.726Å	a = 3.729Å
Volume of WO_3 occupancy	V_C = 51.73 Å^3	V_C = 51.85 Å^3

One can see that the phase changes in WO_3 films are the same as in the 400 WO_3 powder. This study reveals that the phase changes in the WO_3 films and the 400 WO_3 powders are discontinuous phase changes. This may be an important result for the further studies of the EC properties in the WO_3 films and the powders.

Chapter 7

Hydrogen and lithium intercalation in cesium tungsten oxides

The alkali tungsten oxides are a potential electrochromic material due to their inert chemical property and favorable crystal structures (Hussain and Kihlborg 1976; Hussain 1978; Slade et al 1989). The response time of an EC cell mainly depends on the diffusion speed of active species inside the EC materials. As was discussed in Chapter 2, the diffusion speed depends on the atomic size of intercalated species and the crystal structures of EC materials. In searching for an EC material in which hydrogen or lithium diffuse readily, two cesium tungsten oxides were studied: hexagonal cesium tungsten bronze and pyrochlore cesium tungsten oxide. This chapter discusses the compound synthesis, structure analysis and the hydrogen and lithium diffusion coefficient measurements for these two compounds.

7.1 Hexagonal cesium tungsten bronze

Original material and film preparations

The hexagonal cesium tungsten bronze was prepared according to the following solid state reaction:

$$(x/2)Cs_2CO_3 + WO_3 \longrightarrow Cs_xWO_{3+x/2} + (x/2)CO_2 \qquad (7.1)$$

The mixtures of $(x/2)Cs_2CO_3$ + WO_3 powders with x = 0.05, 0.1 0.15, 0.2, 0.3 and 0.4 were heated in argon atmosphere at the temperature of 700°C to 900°C for 2 to 3 days. After reactions the Cs_xWO_3 powders were purified by alternating bathing in hot distilled water and ethanol to remove the residues of unreacted Cs_2CO_3. The final products were of the colors from light gray-yellow to light gray-blue depending on the x in the mixtures. The films were prepared by evaporating the produced Cs_xWO_3 powders onto SnO_2 coated glass and Al foil substrate at a temperature of about 250°C to 300°C. The Cs_xWO_3 films used in this work were polycrystalline obtained by annealing the as-prepared Cs_xWO_3 films in air at 350°C – 400°C for 2 – 3 hours. The annealed Cs_xWO_3 films were transparent.

The crystal structures of prepared Cs_xWO_3 powders and films

The cesium compositions in prepared Cs_xWO_3 powders and films were analyzed by energy-dispersive X-ray spectroscopy. It was found that the x number in the produced Cs_xWO_3 powders (x = 0.09, 0.12, 0.16, 0.22 and 0.30) were different from that in the original mixtures (x = 0.1, 0.15, 0.2, 0.3 and 0.4). The cesium content in the produced Cs_xWO_3 powders was always lower than that in the original mixtures. This might be due to the loss of Cs_2CO_3 at the temperature (700°C – 900°C) higher than its melting point (610°C). However, the evaporated films have the same composition as the powders. The hexagonal structure appears in the produced $Cs_{0.22}WO_3$ and $Cs_{0.30}WO_3$ powders as well as in the $Cs_{0.22}WO_3$ and $Cs_{0.30}WO_3$ films. In this chapter, $Cs_{0.30}WO_3$ films are discussed. Using Rietveld profile refinement program, the structure of $Cs_{0.30}WO_3$ was determined. The results calculated

from the powder and the film were identical. Table 7.1 lists the structure refinement results for the $Cs_{0.30}WO_3$ film, where B is the isotropic temperature factor and the N the occupation number of the atom at the site.

Table 7.1 The symmetry and atomic parameters of $Cs_{0.30}WO_3$, cell dimensions: a = 7.364(4)Å, c = 7.713(3)Å. This table lists half atoms in the unit cell.

Space group: P6/mcm
Refined R factor: R = 0.031

Origin at 3m	x	y	z	B	N
W1	.510	.000	.250	4.25	1.0
W2	.000	.510	.250	4.25	1.0
W3	-.510	-.510	.250	4.25	1.0
O1	.500	.000	.000	1.00	1.0
O2	.000	.500	.000	1.00	1.0
O3	.500	.500	.000	1.00	1.0
O4	.414	.220	.250	1.00	1.0
O5	-.414	.220	.250	1.00	1.0
O6	.220	-.420	.250	1.00	1.0
O7	.220	.420	.250	1.00	1.0
O8	-.414	-.220	.250	1.00	1.0
O9	.220	-.220	.250	1.00	1.0
Cs	.000	.000	.000	5.30	0.89

In table 7.2, raw and calculated X-ray diffraction data are listed, the refined R factor is 0.031. The X-ray diffraction pattern shows systematic absence for *l* = odd. From table 7.1, the content of cesium in a half unit cell is 0.91 which corresponds to x = 0.89/3 ~ 0.296 in Cs_xWO_3 film. The calculated cesium content is quite close to the measured value (x = 0.30) by energy-dispersive X-ray spectroscopy.

Table 7.2 The raw and calculated data of X-ray diffraction patterns of hexagonal $Cs_{0.30}WO_3$ film. d is the spacing and I the intensities in relation to hkl reflections.

h k l	d_o	d_c	I_o	I_c
0 1 0	0.01458	0.01457	14.7	13.8
0 0 2	0.03993	0.03997	31.4	31.0
1 1 0	0.04365	0.04370	0.3	0.3
0 1 2	0.05458	0.05455	45.0	43.5
0 2 0	0.05832	0.05830	100	102
1 1 2	0.08371	0.08368	19.0	19.2
0 2 2	0.09821	0.09825	15.6	15.6
1 2 2	0.1422	0.1419	5.4	5.3
0 0 4	0.1598	0.1600	6.3	7.0
0 3 2	0.1718	0.1712	4.9	4.8
2 2 0	0.1749	0.1748	13.4	13.3
0 2 4	0.2177	0.2182	10.1	10.0
1 3 2	0.2292	0.2293	3.6	3.4
0 4 0	0.2025	0.2032	5.5	5.2

Figure 7.1 shows the X-ray profiles of raw (+++) and calculated (——) data. According to table 7.1, the hexagonal $Cs_{0.30}WO_3$ is formed by six-member rings of (WO_6) octahedra sharing their corners in the (001) plane, and by a stacking of such planes along the [001] axis. Figure 7.2 shows this structure. It is expected that the hexagonal tunnels in this structure may offer an easy path for hydrogen or lithium diffusion.

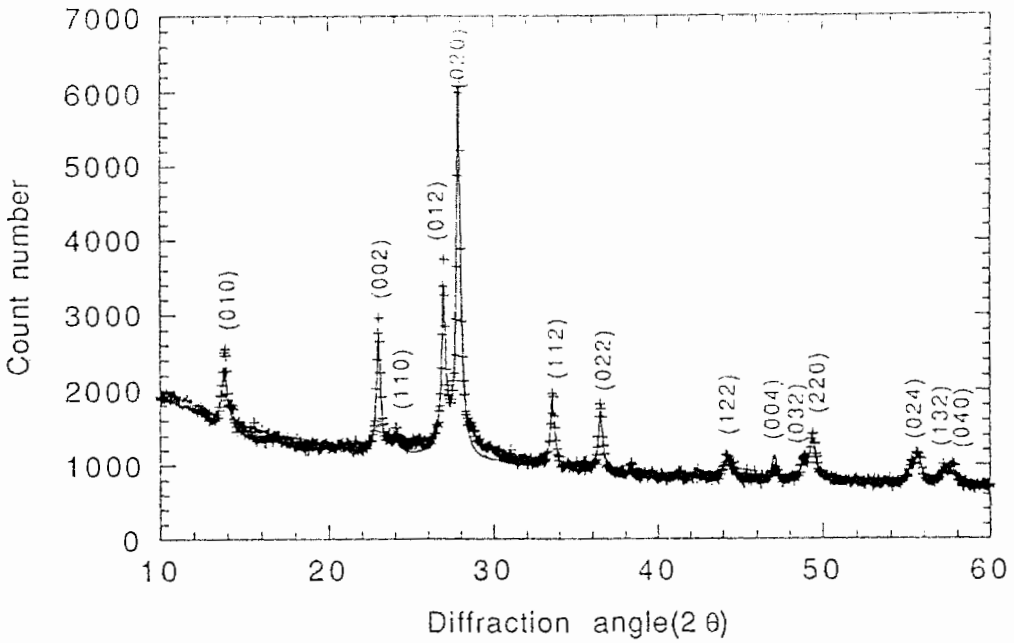

Fig. 7.1 The raw (+++) and calculated (——) X-ray profiles for hexagonal $Cs_{0.30}WO_3$ film.

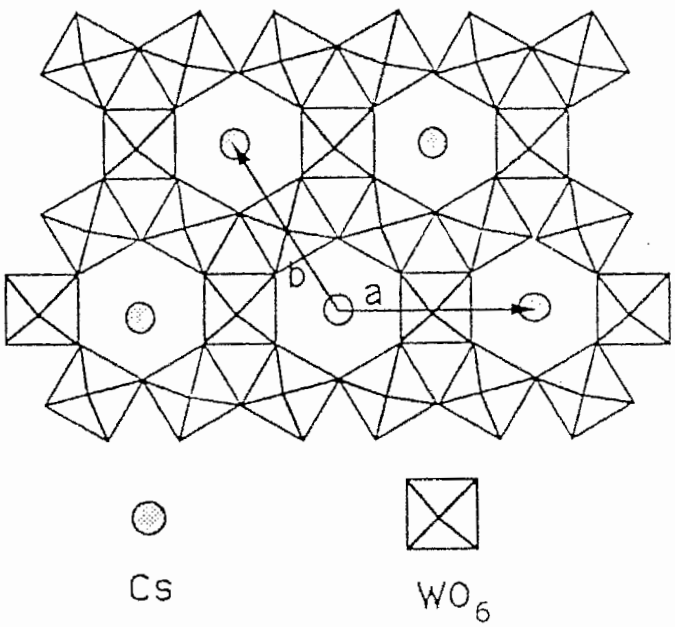

Fig. 7.2 The illustration of crystal structure for hexagonal $Cs_{0.30}WO_3$

The diffusion coefficients of hydrogen and lithium atoms in the hexagonal $Cs_{0.30}WO_3$ films

As WO_3 films, the evaporated $Cs_{0.30}WO_3$ films also turn blue after hydrogen or lithium intercalation. The purpose to develop hexagonal cesium tungsten bronzes is to find a material in which the hydrogen and lithium atoms can diffuse fast. Using the procedures described in section 5.3.3 and equation 5.4 we determined the diffusion coefficients of hydrogen and lithium atoms inside the hexagonal $Cs_{0.30}WO_3$ film. The electrochemical cell used to measure the hydrogen diffusion coefficient has been shown in figure 4.1 and figure 4.2. The results are listed in table 7.3. Both D_H and D_{Li} showed large value at low hydrogen or lithium concentration. With $x < 0.1$ in $H_xCs_{0.30}WO_3$, the values of hydrogen diffusion coefficients ($D_H = 10^{-8} \sim 10^{-9}$ cm^2 s^{-1}) are about one to two order of magnitudes higher than that ($D_H \sim 10^{-10}$ cm^2 s^{-1}) in polycrystalline WO_3 films. However, the D_H in the films drops quickly with increasing hydrogen content in $H_xCs_{0.30}WO_3$. At $x = 0.14$ the hydrogen diffusion coefficient in $H_xCs_{0.30}WO_3$ is close to that in the WO_3 film. The lithium diffusion coefficient D_{Li} has also a high value when $x < 0.05$ in $Li_xCs_{0.30}WO_3$ but drops about two orders of magnitude after the lithium concentration reaches to $x = 0.13$ in $Li_xCs_{0.30}WO_3$ films.

Table 7.3 The diffusion coefficients of hydrogen and lithium atoms inside the hexagonal $Cs_{0.30}WO_3$ film

Hydrogen diffusion coefficient D_H	
x in $H_xCs_{0.30}WO_3$	D_H ($cm^2\ s^{-1}$)
4.3×10^{-5}	3×10^{-8}
3.8×10^{-3}	9×10^{-9}
1.7×10^{-2}	5×10^{-9}
5.4×10^{-2}	2×10^{-9}
0.1	1×10^{-9}
0.14	6×10^{-10}

Lithium diffusion coefficient D_{Li}	
x in $Li_xCs_{0.30}WO_3$	D_{Li} ($cm^2\ s^{-1}$)
2.6×10^{-5}	6×10^{-9}
1.3×10^{-4}	3×10^{-9}
1.0×10^{-3}	2×10^{-9}
2.2×10^{-2}	4×10^{-10}
0.13	6×10^{-11}

The diffusion behavior of hydrogen and lithium atoms in hexagonal $Cs_{0.30}WO_3$ films can be understood. The presence of hexagonal tunnels enhances the diffusion of hydrogen and lithium atoms in $Cs_{0.30}WO_3$ films. However, the diffusion coefficients, D_H and D_{Li}, are expected to decrease after more and more hexagonal tunnels are occupied and blocked by inserted Li and H atoms. As can be seen from figure 7.2, cesium atoms occupy the sites at the center of the six-member rings of (WO_6) octahedra. The

maximum number of cesium at that position in the hexagonal Cs_xWO_3 is x = 0.33. In our case, the cesium concentration is x = 0.30 in Cs_xWO_3, only about 10% of hexagonal site are unoccupied by the cesium. The limited number of unoccupied hexagonal sites may explain the reason why the diffusion coefficients of hydrogen or lithium drops quickly when the composition of hydrogen or lithium reaches to x = 0.05~0.1 in $H_xCs_{0.30}WO_3$ or $Li_xCs_{0.30}WO_3$ films. The D_H and D_{Li} were measured in the single phase regions of $H_xCs_{0.30}WO_3$ ($0 < x < 0.15$) and $Li_xCs_{0.30}WO_3$ ($0 < x < 0.15$). In our experiments, no structural change was observed from the X-ray diffraction data at $x < 0.25$ in $H_xCs_{0.30}WO_3$ and $x < 0.15$ in $Li_xCs_{0.30}WO_3$.

7.2 Pyrochlore cesium tungstate

Preparations of powders and films

The pyrochlore cesium tungstate $(Cs_2O)_xW_2O_6$ (abbreviated as PCT) was prepared by precipitation in acidified ethylene glycol solvent (Coucou and Figlarz 1988). 10g Na_2WO_4 + 2g Cs_2CO_3 were first completely dissolved in heated ethylene glycol solvent, followed by gradually acidifying the solution with acetic acid at a temperature of about 85°C. The reactions took about 5 – 10 hours to complete and lead to a suspension of white PCT. The suspension of white PCT turned to a white precipitate after another 5 – 10 hours. The dried PCT powder was obtained after rinsing and centrifuging the precipitate several times. The final PCT powder was snow white. The produced PCT powder was then used as source material to evaporate PCT thin film. The evaporation was carried out in a vacuum of 2 x 10^{-5} torr and the substrate was heated to about 200°C in order to obtain

a film of good adhesion to the substrate. The freshly-evaporated PCT films were amorphous and become polycrystalline after annealing at 350°C to 400°C for 3 – 4 hours. The annealed polycrystalline films were transparent.

The crystal structures of PCT powders and films

The crystal structures of PCT powders and films evaporated from the PCT powder were found to be the same: cubic with lattice constant a = 10.366Å. The PCT unit cell belongs to the space group Fd3m. The diffraction peaks can be observed only when h, k or l equals to 4n or 4n+2, or h + k + l = 4n or 2n+1. The structure of the unit cell and the symmetry of the lattice were finally determined by the profile refinements. Table 7.4 lists refinement results for the atomic positions of PCT in the unit cell and table 7.5 lists the observed and calculated peak positions and intensities in the X-ray diffraction pattern. The final refined parameter R is 0.072. From table 7.4, it is clear that all atoms are at special positions. For each kind of atom, one atom position is listed. The positions of other atoms can be obtain from the symmetry operation of the space group. It is found during the refinement that not all the sites are fully occupied by the atoms. The occupation numbers of cesium at 8b and oxygen at 16d sites correspond to the x = 0.43 in $(Cs_2O)_xW_2O_6$ which is somewhat higher than that expected from the original solutes in the solution (x = 0.40).

Table 7.4 The atomic parameters of PCT in the unit cell, a = 10.366Å

Space group: Fd3m

Refined R factor: R = 0.072

Origin at 3m	site	x	y	z	B	N
W	16c	0.0	0.0	0.0	3.9	1.0
O	48f	0.301	1/8	1/8	1	1
Cs	8b	3/8	3/8	3/8	1.3	0.85
O	16d	1/2	1/2	1/2	4.7	0.21

With this atom arrangement in the unit cell, the peak intensity and the diffraction profile were calculated. Table 7.5 lists the raw and calculated X-ray diffraction data and figure 7.3 shows the results in the profile refinement.

From these refinement results, the PCT structure is determined. This structure can be similarly described by stacking disordered hexagonal Cs_xWO_3 layers in (111) direction (Figlarz 1989). Figure 7.4 shows the schematic view of the PCT matrix in the (111) direction. As can be seen from these pictures, three dimensional interconnected hexagonal tunnels are formed in the PCT.

Table 7.5 The raw and calculated d spacing and intensities in the x-ray diffraction pattern of PCT films.

h k l	d_o (Å)	d_c (Å)	I_o	I_c
1 1 1	5.989	5.985	34.4	39.2
2 2 0	3.667	3.665	16.4	14.2
3 1 1	3.122	3.126	90.0	100.0
2 2 2	2.997	2.993	44.6	45.7
4 0 0	2.594	2.592	2.9	2.9
3 3 1	2.375	2.378	0.2	0.2
4 2 2	2.113	2.116	1.7	1.8
5 1 1	1.992	1.995	18.7	10.0
3 3 3	1.992	1.995		9.7
4 4 0	1.834	1.833	18.8	19.3
5 3 1	1.757	1.753	0.8	0.8
4 4 2	1.729	1.728	0.0	0.0
6 2 0	1.638	1.639	3.7	4.0
5 3 3	1.581	1.581	6.2	6.3
6 2 2	1.559	1.563	6.7	6.1
4 4 4	1.497	1.497	0.4	0.4
5 5 1	1.451	1.452	0.5	0.4
7 1 1	1.451	1.452		0.1
6 4 2	1.387	1.385	1.9	2.0
5 5 3	1.351	1.350	5.9	1.5
7 3 1	1.351	.350		4.4
8 0 0	1.297	1.296	1.4	1.4

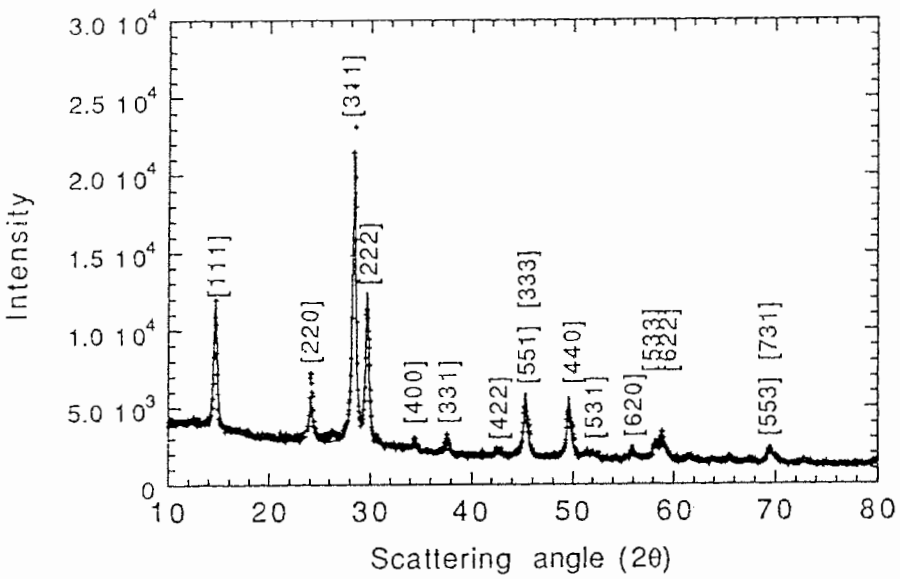

Fig. 7.3 Raw (+++) and calculated (——) X-ray diffraction patterns of PCT.

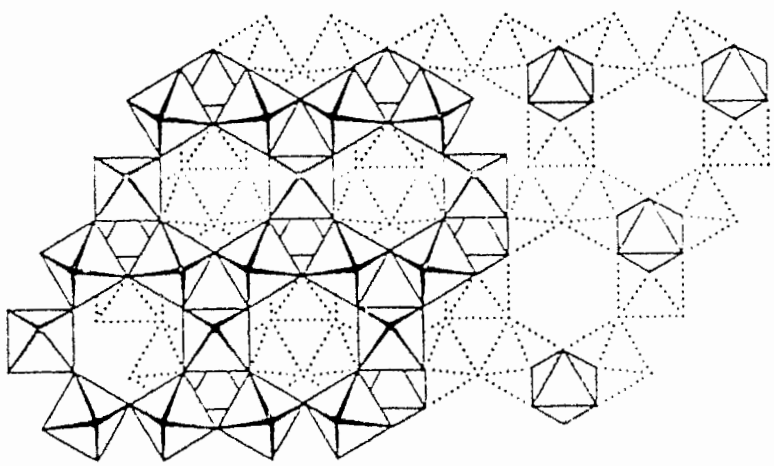

Fig. 7.4 Schematic view of PCT matrix in the (111) direction.

Diffusion coefficients of hydrogen and lithium in PCT

The PCT films could be colored by intercalating hydrogen or lithium. In order to determine the diffusion coefficients of hydrogen and lithium in PCT, the current step method was used again. The EC cell used to determine the D_H in the PCT is shown in figure 4.1 and the cell used to determine the D_{Li} in the PCT film was the battery cell described by figure 4.2. The measured D_H and D_{Li} are listed in table 7.6. No crystal structure change was observed in light blue colored (OD < 0.5) H_xPCT ($0 < x < 0.22$) and Li_xPCT ($0 < x < 0.14$). So most D_H and D_{Li} data in table 7.6 were obtained in a single phase region of H_xPCT or Li_xPCT. The D_H and D_{Li} data obtained from the regions of $x > 0.22$ in H_xPCT and $x > 0.14$ in Li_xPCT may be used as a reference. From the measured data, it was found that the hydrogen or lithium diffusion coefficients, D_H or D_{Li}, are independent of the hydrogen or lithium concentration in the PCT films and about one order of magnitude higher than that in the WO_3 film.

Table 7.6 The diffusion coefficients of hydrogen and lithium in PCT film.

Hydrogen diffusion coefficient D_H	y in H_yPCT	D_H ($cm^2\ s^{-1}$)
	0.047	7.2×10^{-9}
	0.08	7.9×10^{-9}
	0.14	6.3×10^{-9}
	0.29	6.9×10^{-9}
	0.50	4.9×10^{-9}
Lithium diffusion coefficient D_{Li}	y in Li_yPCT	D_{Li} ($cm^2\ s^{-1}$)
	0.057	5.2×10^{-11}
	0.11	3.4×10^{-11}
	0.31	3.0×10^{-11}

7.3 Discussions

As is mentioned at the beginning of this chapter, the purpose of this study was to find a tungsten compound in which hydrogen or lithium will have a faster diffusion than in the monoclinic WO_3 host. To obtain an appropriate optical density change in WO_3 films, certain hydrogen or lithium concentration of $x = 0.1$ to 0.2 in H_xWO_3 or Li_xWO_3 was usually needed. Almost the same quantity of hydrogen or lithium was also required for the optical density changes in hexagonal $Cs_{0.30}WO_3$ and PCT. From the results discussed in this chapter, it was found that the hydrogen and lithium diffusion coefficients in $Cs_{0.30}WO_3$ and PCT are much higher than that in the monoclinic WO_3. At low hydrogen and lithium concentration, the hydrogen and lithium diffusion coefficients in hexagonal $Cs_{0.30}WO_3$ are about two orders of magnitude higher than that in WO_3. When the hydrogen or lithium concentration in the $Cs_{0.30}WO_3$ reached to $x = 0.1 \sim 0.2$, hydrogen or lithium diffusion coefficients drop to smaller values but still higher than that in WO_3. The data listed in table 7.6 shows that the diffusion coefficients of hydrogen and lithium atoms in the pyrochlore $(Cs_2O)_{0.43}W_2O_6$ structure are about one order of magnitude higher than that in WO_3 throughout all hydrogen or lithium concentration regions. The main reason is differences in the host structure. If we compare the crystal structure of monoclinic WO_3, hexagonal $Cs_{0.30}WO_3$ and the PCT, the volumes of the unit cells in each structure can be calculated from the data obtained:

Monoclinic WO_3	$V_M = 424.1$ Å^3
Hexagonal $Cs_{0.30}WO_3$	$V_H = 362.3$ Å^3
Pyrochlore PCT	$V_P = 1113.9$ Å^3

Considering that there are 8 octahedra in the monoclinic WO_3 unit cell, 6 in the hexagonal $Cs_{0.30}WO_3$ unit cell, and 16 in the PCT unit cell, the space occupied by one octahedron in each structure is:

in WO_3	53.01 Å^3
in $Cs_{0.30}WO_3$	60.38 Å^3
in $(Cs_2O)_{0.43}W_2O_6$	69.56 Å^3

If one considers the crystal structure itself, the hexagonal structure should allow faster diffusion than the monoclinic structure and the pyrochlore structure should be even faster than the hexagonal structure for lithium or hydrogen insertion. The cesium atoms in the tungsten oxide host may reduce the free spaces in the hexagonal and pyrochlore structures and thus reduce the lithium and hydrogen diffusion coefficients. Considering high hydrogen and lithium diffusion coefficients in these two materials, hexagonal $Cs_{0.30}WO_3$ and pyrochlore $(Cs_2O)_{0.43}W_2O_6$ should be good candidates to be used as fast EC layer for hydrogen and lithium intercalation.

Chapter 8

Conclusions

The intercalation processes of lithium and hydrogen in WO_3 films, various WO_3 powders and cesium tungsten compounds have been intensively studied. The results achieved in this study have been discussed in details in the previous chapters. In this chapter, we list some main contributions of this work as conclusion.

1. We determined the crystal structures of electrochemically formed Li_xWO_3 films and Li_xWO_3 powders within $0 < x < 0.5$. The phase transitions from monoclinic to tetragonal and then to cubic can be attributed to the changes of W—O bonding length and bonding angle. The lithium intercalation and deintercalation are reversible provided $x < 1$ in Li_xWO_3.
2. We determined the phase diagram for 400 Li_xWO_3 powder. This thesis revealed that the phase transitions in Li_xWO_3 from monoclinic to tetragonal and then from tetragonal to cubic are discontinuous phase transition, i.e. during the phase transition, two phases are co-existing in the Li_xWO_3.
3. We determined the crystal structure of tetragonal H_xWO_3 film and revealed that tetragonal H_xWO_3 and Li_xWO_3 have a very similar crystal structure, space group, atom position and unit cell dimensions. The

structure determination for tetragonal H_xWO_3 film is also a direct evidence to support the tungsten bronze model.

4. We showed that the lithium intercalation in various WO_3 powders could be totally different. A reproducible experiment technique is reported.
5. For lithium and hydrogen intercalation in hexagonal and pyrochlore cesium tungsten oxides, the diffusion coefficients of hydrogen and lithium atoms were found to be dependent on the crystal structures.

To further clarify the physical and chemical properties of WO_3 host after lithium and hydrogen intercalation, some further work may be necessary:

1. Electric conductivity measurements for various tungsten bronzes, such as the studies in insulator–metal transition as function of intercalated species. The studies in the conductivity may reveal more information about the WO_3 band structure.
2. This thesis did not answer the question why the commercial WO_3 powder and 900 WO_3 powder showed totally different properties for lithium intercalation from that of 400 WO_3 powder, 700 WO_3 powder and WO_3 films. There could be many possible reasons for this, such as impurity or defects in the crystallites, water or hydrogen content, and crystal grain size, etc.. Some more analytical means, such as NMR, IR, ESR, could be used to pursue such investigation.

References

Armand, M.B., Thesis, Inst. Nationale Polytechnique de Grenoble, (1981)

Arnoldussen, T.C., J. Electrochem. Soc., 123 (1976) 527

Arnoldussen, T.C., J. Electrochem. Soc., 128 (1981) 117

Barna, G.G., J. Electron. Mat., 8 (1979) 153

Benjamin Reichman and Allen J. Bard, J. Electrochem. Soc., 126 (1979) 583

Berkowitz, J., Chupka, W.A. and Inghram, M.G., J. Chem. Phys., 27 (1957) 85

Brimm, E.O.,Brantley, J.C., Lorenz, J.H. and Jellinek, M.H., J. Am. Chem. Soc., 73 (1951) 5427

Calvert, J.M., Manuccia, T.J. and Nowak, R.J., J. Electrochem. Soc., 133 (1986) 951

Colton, R.J., Guzman, A.M. and Rabalais, J.W., J. Appl. Lett., 49 (1978) 409

Corker, G.A., Grant, G. and Clecak, N.J., J. Electrochem. Soc., 126(8) (1979) 1339

Coucou, A and Figlarz, M., Solid State Ionics 28-30 (1988) 1762

Crandall, R.S. and Faughnan, B.W., Appl. Phys. Lett., 28 (1976) 95

Crandall, R.S. and Faughnan, B.W., Phys. Rev. Lett., 39 (1977) 232

Crowder, B.L. and Sienko, M.J., J. Chem. Phys., 38(7) (1963) 1576

Dautremont-Smith, W.C., Beni, G., Schiavone, L.M. and Shay, J.L.,

Dautremont-Smith, W.C., Display, April (1982) 67

Dautremont-Smith, W.C., Display, April (1982) 3

Deb, S.K. and Chopoorian, J.A., J. Appl. Phys., 37 (1966) 4818

Deb, S.K., Appl. Opt. Suppl., 3 (1969) 193

Deb, S.K., Philos. Mag. 27 (1973) 801

Deb., S.K. and Witzke, H., 19th Electronic Materials Conf., (Cornell, New York, U.S.A. 1977) abstract G7

Deneuville, A. and Gerad, P., J. Electron. Mat., 7 (1978) 559

Deneuville, A., Gerad, P. and Billat, R., Thin Solid Films 70 (1980) 203

Dickens, P.G. and Hurditch, R.J., Nature 215 (1967) 1266

Dickens, P.G., Chippindale, A.M. and Hibble, S.J., Solid State Ionics 34 (1989) 79

Dyer, C.K. and Leach, J.S., J. Electrochem. Soc., 125 (1978) 23

Faughnan, B.W., Crandall, R.S. and Heyman, P.M., RCA Rev. 36 (1975a) 177

Faughnan, B.W., Crandall, R.S. and Lampert, M.A., Appl. Phys. Lett., 27(5) (1975b) 275

Faughnan, B.W. and Crandall, R.S., Chapter 5 in "Topics in applied physics" Vol. 39 edited by J., Pankove (Springer Verlag press, N.Y. 1980)

Figlarz, M., Prog. Solid State Chem., 19 (1989) 1

Flanagan W.C. and Miles C.L., Eastman Kodak, US patent 3 153 113, Electro-light valve (1964)

Freedman, M.L., J. Am. Chem. Soc., 81 (1959) 3834

Freedman, M.L. and Leber, S., J. Less-Common Met., 7 (1964) 427

Gavrilyuk, A.I. and Chudnovskii, F.A., Sov Tech. Phys. Lett., 3 (1977) 69

Gerad, P., Deneuville, A. and Courth, R., Thin Solid Films 71 (1980) 221

Glemser, O., and Chr. Naumann, Z. Anorg. & Allg.Chem. 265 (1951) 2881

Glemser, O., Weidelt, J., and Fruend, F., Z. Anorg. & Allg. Chem., 332 (1964) 299

Goldner, R.B., Mendelsohn, D.H., Alexander, J., Henderson, W.R., Fitzpatrick, D., Hass, T.E. and Sample, H.H., Appl. Phys. Lett., 43 (1983) 1093

Goldner, R.B., Norton, P., Wong, K, Foley, G., Goldner, E.L., Seward, G. and Chapman, R., Appl. Phys. Lett., 47 (1985) 536

Green, M. and Richman, D., Thin solid films 24 (1974) S45

Green, M., Smith, W.C.and Weiner, J.A., Thin solid films 38 (1976) 89

Henry, N.F.M. and Lonsdale, K., "International Tables for X-ray Crystallography", Vol. 4, 2nd edition (Kynoch Press, Birmingham, England. 1965)

Hersh, H.N., Kramer, W.E. and McGee, J.H. Appl. Phys. Lett. 27 (1975) 646

Hiroshi Morita and Hiroshi Washida, Japan. J. of Appl. Phys., 23 (1984) 754

Hiroshi, Y. and Yoshihiro, S., J. Electrochem. Soc., 137 (1990) 3826

Ho, C., Raistrick, I.D. and Huggins, R.A., J. Electrochem. Soc., 127 (1980) 343

Howard, C.J. and Hill, R.J., Australian Atomic Energy Commission Report NO. M112 (1986)

Hurditch, R., Electron. Lett., 11 (1975) 142

Hussain, A. and Kihlborg, L., Acta Cryst. A32 (1976) 551

Hussain, A., Acta Chem. Scand. A32 (1978) 479

Hutchinson, E., "Physical chemistry", (W.B. Saunders Company, Philadelphia & London. 1962) p19

Kaneko, H., Nagao, F., and Miyake, K., J. Appl Phys., 63 (1988) 510

Kaufman, F.B., Schroeder, A.H., Engler, E.M., and Patel, V.V., Appl. Phys. Letter 36(6) 422 (1980)

Kazusuke Yamanaka, Japanese J. of Appl. Phys., 25 (1986) 1073

Kehl, K.L., Hay, R.G. and Wahl, D., J. Appl. Phys., 23 (1952)

Knowles, T.J., Appl. Phys. Lett., 31 (1977) 817

de Koster, H., General Time Corp., US Patent 3 626 410, Moving indicator electrochemical displays

Lagzdons, J.L., Bajars, G.E. and Lusis, A.R., Phys. Stat. Sol., 84(a) (1984) K197

Lampert, Carl M., Solar Energy Materials 11 (1984) 1

Lipson, H. and Steeple, H., "Interpretation of X-ray Powder Diffraction Patterns", (St Martin's Press, New York, 1970)

Loopstra, B.O. and Rietveld, H.M., Acta Cryst., B25 (1969) 1420

Matsuhiro, K. and Masuda, Y., Proc. Soc. Inf. Disp., 21 (1980) 101

Mckinnon, W.R., Ph.D. Thesis: "Physics of Intercalation Batteries" , University of British Columbia (Vancouver, British Columbia, Canada) 1980.

Mendelsohn, D.H and Goldner, R.B., J. Electrochem. Soc., 131 (857) 1984

Miyamura, M., Tomura, S., Imai, A. and Inomata, S., Solid State Ionics 3/4 (1981) 149

Mohapatra, S.K., J. Electrochem. Soc., 125 (1978) 284

Morita, Japan J. Appl. Phys., 21 (1982) 655c

Moskslev, P.N. and Demchishin, A.V., Phys. Met. Mettalogr., 28 (1972) 1019

Nicholson, M.M. and Pizzarello, F,A., J. Electrochem. Soc., 126 (1979) 1490

Nicholson, M.M. and Pizzarello, F,A., J. Electrochem. Soc., 128 (1980) 1228

Ottaviani, M., Penero, S., Morzilli, S., Scrosati, B. and Lazzari, M., Solid State Ionics 20 (1986) 197

Pfifer, J.H. and Sichel, E.K., J. Electron. Mater., 9 (1980) 129

Platt, J.R., J. Chem. Phys., 34 (1961) 864

Pohl,R.W. Naturwissenschaften 20 (1932) 932

Rabalais, J.W., Colton, R.J. and Guzman, A.M., Chem. Phys. Lett., 29 (1974) 131

Randin, J.P., J. Electronic Mater., 7 (1978) 47

Randin, Jean-Paul, J. Electrochem. Soc., 129 (1982) 1215

Rauh, R.D. and Cogan, S.F., Solid State Ionics 28-30 (1988) 1707

Reichman, B. and Bard, A.J., J. Electrochem. Soc., 127 (1980) 241

Rietveld, H.M., Acta Crystallogr. 22 (1967) 151

Rietvled, H.M., J. Appl. Crystallogr. 2 (1969) 65

Salje, E., Acta Cryst., B33 (1977) 574

Schirmer, O.F., Wittwer, V., Baur, G. and Brandt, G., J. Electrochem. Soc., 124 (1977) 749

Schlotter, P. and Pickelmann, I., 21st Electronic Materials Conf. (Boulder, Colorado, USA. 1979) abstrat B5

Schlotter, P. and Pickelmann, I., 22st Electronic Materials Conf. (Boulder, Colorado, USA. 1980) abstrat A4

Schlotter, P., J. Electronic Materials 16 (1987) 39

Schoot,C.J., Ponjee,J.J., Van Dam,H.T., Van Doorn,R.A. and Blowijn,P.T. Appl. Phys. Lett., 23 (1973) 64

Schulman,J. H. and Compton,W.D. "Color centers in solids", International series of monographs on solid state physics, Edited by R. Smoluchowski and N. Kurti (Pergamon Press Inc. New York, 1962)

Sienko, M.J. and Tuong, T.B., J. Am. Chem. Soc., 83 (1961) 3939

Sienko, M.J. and Berak, J. "The Chemistry of Extended Defects in Nonmetallic Solids", Edited by L. Eyring and M. O'keefe, (Elsevier press, Amsterdam, 1970) p541

Slade, C.R., West, B.C. and Hall, G.P., Solid State Ionics 32/33 (1989) 154

Stuart F. Cogan, Nguyet M. Nguyen, Stephen J. Perrotti, and R. David Rauh, J. Appl. Phys., 66 (1989) 1333

Talmey, P., US Patent 2 281 031 (1942), 2 319 756 (1943)

Tanisaki, S., Japan J. of Phys. Soc., 15 (1960) 566

Tanisaki, S., Japan J. of Phys. Soc., 15 (1960) 573

Torossian, G., Am. J. Sci., 38 (1914) 537

Tsutomu Kawata, Motokazu Yamamoto, et al. Jepan, J. Appl. Phys., 14 (1975) 725

Van Dam, H.T. and Ponjee, J.J. J. Electrochem. Soc., 121 (1974) 1555

Weibel, G.E., in "Non-emissive electro-optic displays", Edited by A.R. Kmetz, and F.K. von Willisen (Plenum press, New York 1976)

Weppner, W. and Huggins, R.A., Ann. Rev. Mat. Sci., 8 (1978) 269

Witzke, H., Deb, S.K., 19th electronic materials conf. (Cornell, New York, USA, 1977) abstract G8

Wiles, D.B. and Young, R.A., J. Appl. Crystallogr. 14 (1981) 149

Yamada, S., Nakamura, T., Hiruta, Y., Urabe, K. and Kitao, M., Japan J. Appl. Phys., 22 (1983) 789

Zaromb, S., J. Electrochem. Soc., 109 (1962) 903

Zaromb, S., J. Electrochem. Soc., 109 (1962) 912

Zaromb, S., Philco Corp., US Patent 3 245 313, Light modulating means employing a self-erasing plating solution (1966)